Università di Pisa

FACOLTÀ DI SCIENZE MATEMATICHE, FISICHE E NATURALI
Corso di Laurea Magistrale in Fisica

Tesi di Laurea Magistrale

Evaluation of physical image quality of the preclinical scanner IRIS CT using conventional and nanoparticle-based contrast agents

Candidato:
Antonella STASI

Relatore:
Prof. Daniele PANETTA

Anno Accademico 2015-2016

A me stessa

Acknowledgements

"Non è il suo moto per altro distinto
ma li altri son mensurati da questo."
(La Divina Commedia - Paradiso: C. XXVII, v.115-116)

Con questi versi vorrei cominciare dal principio, dal mio primo mobile, perché la sua tenacia e passione per il suo lavoro hanno impresso il moto a tutti gli altri "cieli", portandomi fin qui. Grazie per i tuoi quotidiani sacrifici e per la fiducia che mi hai sempre dimostrato. Grazie alla donna più importante, l'Atlante della famiglia, che da lontano mi è sempre stata vicino, incoraggiandomi nei giorni di malumore e rallegrandosi con me in quelli più gioiosi. Grazie al Sale&Pepe delle mie giornate e luce di tutte le mie sere, diario segreto al quale ho sempre confidato le mie paure, le mie gioie, e le mie speranze. Grazie per la tua immensa pazienza e per il tuo amore che mi ha quotidianamente accompagnato in questa esperienza. Grazie ad un amico (gian)prezioso, sempre contento di assistere ai miei, a volte insensati, sfoghi. Grazie per la tua accoglienza, hai fatto di una caserma il posto in cui ho sempre trovato serenità, il ritrovo domenicale di un gruppo pazzo e assurdo senza il quale Pisa non sarebbe stata la stessa. Grazie anche al capriccio di ogni riccio che si è sempre preoccupato per i miei stati d'animo ballerini.
Vorrei inoltre ringraziare il Dott. Piero Salvadori per avermi dato l'opportunità di realizzare questo lavoro presso l'Istituto di Fisiologica Clinica del CNR. I mesi ivi trascorsi rappresentano per me un'esperienza molto importante e costruttiva. Un ringraziamento speciale va al Professor Daniele Panetta per avermi dato la possibilità di conoscere questo affascinante campo della scienza. Grazie per avermi constantemente seguita durante l'intero periodo di tesi, e per aver sempre chiarito tutti i miei dubbi con grande professionalità.
Ringrazio il Dott. Valerio Voliani del NEST della Scuola Normale Superiore e Rosa D'Apice per la loro disponibilità a fornirmi tutti gli strumenti necessari per poter svolgere gli esperimenti con le nanoparticelle.
Grazie infine a tutti coloro che hanno condiviso con me anche un solo minuto di questa esperienza, ciascuno di voi, a proprio modo, ha contributo alla, si spera buona, riuscita di questo lavoro.

Antonella

Contents

List of abbreviations

1D	One-dimensional
2D	Two-dimensional
3D	Three-Dimensional
4D	Time-resolved three-dimensional (or four-dimensional)
ADD	Axis to Detector Distance
AOR	Axis of Rotation
BH	Beam Hardening
CA	Contrast Agent
CCD	Charge Coupled Device
CMOS	Complementary Metal Oxide Semiconductor
CNR	Contrast to Noise Ratio
CsI	Cesium Iodide
CT	Computed Tomography
CTDI	Computed Tomography Dose Index
DAQ	Data Acquisition
DCE	Dynamic Contrast-Enhanced
DFT2D	Two-Dimensional Discrete Fourier Transform
EAE	Energy Absorption Efficiency
FBP	Filtered Back Projection

FDK	Feldkamp-Davis-Kress
FOV	Field of View
FPG	Fast Prospective Gating
FS	Full Scan
FWHM	Full Width at Half Maximum
GNPs	Gold Nanoparticles
GUI	Graphical User Interface
H-LSF	Horizontal Line Spread Function
HU	Hounsfield Unit
LSF	Line Spread Function
LSI	Linear Shift Invariant
LOR	Line of Response
MRI	Magnetic Resonance Imaging
MTF	Modulation Transfer Function
NNPS	Normalized Noise Power Spectrum
NPs	Nanoparticles
NPS	Noise Power Spectrum
PEG	Polyethylene Glycol
PET	Positron Emission Tomography
PG	Prospective Gating
PMT	PhotoMulTiplier
PSF	Point Spread Function
PVE	Partial Volume Effect
QA	Quality Assurance
QE	Quantum Efficiency

RES	Reticuloendothelial System
RG	Retrospective Gating
ROI	Region of Interest
SAD	Source to Axis Distance
SCD	Symmetric Charge Division
SDD	Source to Detector Distance
SNR	Signal to Noise Ratio
SPECT	Single Photon Emission Tomography
SS	Short Scan
TAC	Time Attenuation Curve
TFT	Thin Film Transistor
V-LSF	Vertical Line Spread Function
VOI	Volume of Interest

Introduction

This thesis is focused on preclinical micro-Computed Tomography (CT) imaging, a particular imaging method that is largely used to study small animal models of human diseases. Essentially it is based on the same physical principles of a clinical CT scanner, but it is designed for higher-resolution imaging. The strengths of micro-CT lie in fact in its high spatial resolution, relatively low cost, and scanning efficiency making this imaging technique one of the most interesting, attractive and complementary to other ones such as Positron Emission Tomography (PET) or Single Photon Emission Tomography (SPECT). Moreover the growing interest in the development and validation of new Contrast Agents (CAs) allows to go far beyond the simple imaging of soft tissues enabling various applications such as molecularly targeted imaging and functional imaging.
The main goals of this thesis are:

- evaluate the performances of the IRIS CT scanner focusing on the physical image quality of fast dynamic imaging protocol;
- provide a first correction of Beam Hardening (BH) by means of the water precorrection method;
- examine the x-ray properties of a novel CA which is under developement at the Center for Nanotechnology Innovation@Nest, Istituto Italiano di Tecnologia.

The work presented here is structured as follows.
In **Chapter 1** the physical principles of micro-CT will be explained, from the x-rays production, passing through x-rays attenuation, up to x-rays detection. Then attention will be paid on the fundamentals of image reconstruction, describing all the steps concerning with the Filtered Back Projection (FBP), starting from the definition of *line integral* to explain the meaning of a projection view, and to finally state the *Fourier slice theorem*, from which the FBP algorithm can be derived. At the end of the chapter the main applications of micro-CT will be presented focusing especially on the importance that 4D micro-CT imaging covers nowadays.

In **Chapter 2** the IRIS PET/CT scanner, operating at the Institute of Clinical Physiology of the National Research Council in Pisa, will be described in all of its parts. The PET component will be briefly described, then specific attention will be paid on the CT section.
Chapter 3 is a digression on CAs available on the market for micro-CT imaging. More specifically it will stress the difference between *water-soluble* and *blood-pool* agents. According to this first kind of classification, they will be further grouped depending on the main material of which they consist. Thus it will be focused on iodinated, nanoparticulated and liposomal CAs, on their main applications in in-vivo imaging and on the huge development that nanotechnology has poured also in this field.
In **Chapter 4** perfomances characterization of the IRIS CT scanner is presented. Performances of the flat panel detector will be evaluated in the frequency domain in terms of the Noise Power Spectrum (NPS). The spatial resolution of the IRIS CT scanner will be analyzed in terms of Modulation Transfer Function (MTF). Noise of reconstructed images will be evaulated in the frequency domain by means of NPS, and in the spatial domain in terms of the standard deviation σ as a function of the dose and the voxel size. Since the IRIS scanner can operate in dynamic mode for applications such as perfusion studies, images acquired with the scanning protocol that was designed for this task, will be object of study. The characterization will be focused especially on noise level and Contrast to Noise Ratio (CNR) in terms of density of the irradiated material. CNR will be also evaluated in terms of the object dimension as to evaluate the impact of Partial Volume Effect (PVE) on this fast imaging protocol. Finally, results of the Hounsfield Unit (HU) calibration will be presented, as well as those obtained from the BH correction that was performed by the water precorrection for the first time on the IRIS CT scanner.
In **Chapter 5** the first results that have been obtained in phantom studies with a new kind of nanoparticle based CA will be illustrated. In these studies, analytical simulations of the imaging process preceded experiments, since it was the first time that a CA different from iodine was used in IRIS CT studies. Thus, phantom simulation will be described along with the home made phantom that was specially constructed for these measurements, and the metal Nanoparticles (NPs) employed for these experiments. The main goal for these first measurements was in fact to assess the sensitivity of the system (expressed in HU/mg/mL) to nanoparticle based CA for all tube voltages, reserving for the future the investigation of possible applications of this novel CA in micro-CT.

Chapter 1

Microcomputed tomography for preclinical imaging

Introduction

High-resolution Computed Tomography or micro-CT is the preclinical equivalent of CT and is used to study small-animal models of human diseases.
The first x-ray microtomography system was conceived and built by Jim Elliott in the early 1980s. Actually, only in 1994, with the presentation of the first commercially available bone micro-CT scanner, this technique started to become more relevant and today it covers a central role in disease detection and monitoring, in morphological and functional phenotyping, and in testing potential therapies and the safety of new drugs.

A micro-CT scanner is based on the same underlying physical principles of a clinical CT scanner, but it is designed for higher-resolution imaging. It typically produces Three-Dimensional (3D) tomographic data related to the spatio-temporal distribution of the mean linear attenuation coefficient with spatial resolutions in the order of 10-100 μm. This task is accomplished by taking a few hundreds of Two-dimensional (2D) cone beam projections from multiple angles around the object. The multiple projections are then combined using a reconstruction method.
The main design target of most recent micro-CT for in vivo imaging of small animals is the reduction of the scanning time and radiation dose while preserving the spatial resolution. Keeping the animal dose at low levels is indeed very important to enable longitudinal studies avoiding radiation-related injuries, in agreement with the 3 R's law (Reduction, Refinement, Replacement) and with the most recent recommendation and directives on the use of animals in experimental research.

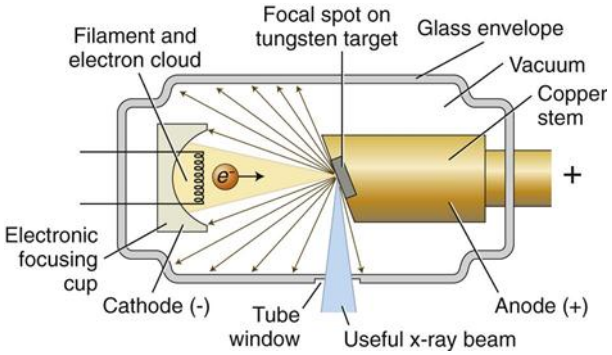

Figure 1.1: Schematic overview of an x-ray microfocus tube and its components.

The last few years have also seen a growing interest in the development and validation of new Contrast Agents (CAs) for preclinical CT and, at the same time, in the implementation of dynamic micro-CT instrumentation and scanning protocols enabling functional imaging via kinetic analysis of CA's Time Attenuation Curve (TAC).

1.1 Physical fundamentals of micro-CT

In this chapter, the principles of micro-CT are explained in general.
A typical micro-CT scanner uses an x-ray tube and a digital x-ray detector, with two possible design geometries: rotating gantry (x-ray source and detector) or rotating specimen. The majority of current commercial systems for in vivo scanning use the rotating gantry geometry.

1.1.1 X-rays production

X-ray microfocus tubes are the most used systems for x-rays production in micro-CT and have a decisive influence on the image quality, as will be further explained. As reported in Figure 1.1, a x-ray tube consist of an oil-filled housing containing an evacuated envelope of heat-resistant borosilicate glass within which a filament and an anode are mounted. When the cathode filament is heated, it produces a narrow beam of electrons that are accelerated by a potential difference (in the range of 30-100 kV for most micro-CT scanners). The anode is generally constructed with tungsten although molybdenum is used for special applications where a low-energy beam is required. In x-ray microfocus tubes the anode is fixed, unlike clinical x-ray tubes where the anode is rotating in order to better dissipate the heat. The electrons interact with the material of the anode, where they slow down by multiple coulomb-type collisions with atomic electrons and nuclei, and even-

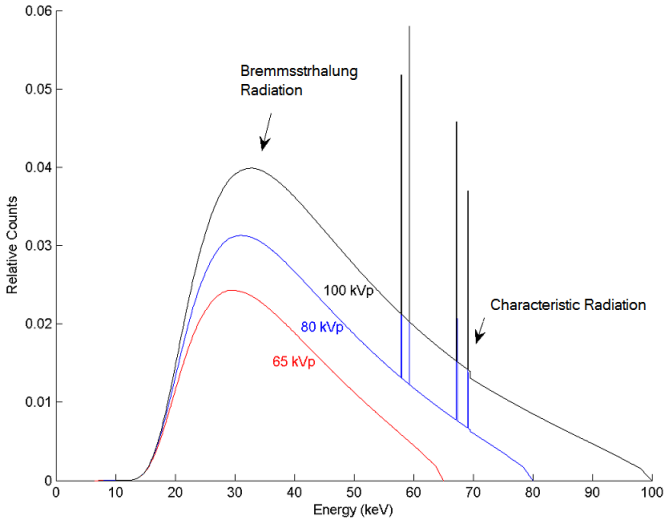

Figure 1.2: X-ray spectra of a x-ray tube with tungsten anode, for different tube voltages.

tually they loose all their initial kinetic energy in a very thin layer underneath the anode surface. Most of the energy absorbed from the electrons appears in the form of heat, only a small amount (less than 1 %) appears in the form of x-rays.
If the electron interacts with an inner-shell electron of the target, characteristic X-radiation with a discrete energy spectrum is produced. These kind of x-rays result when the interaction is sufficiently strong to ionize the target atom by total removal of the inner-shell electron. The appearing vacancy will be therefore filled with an outer-shell electron resulting in a emission of a fluorescence x-ray photon with energy equal to the difference in the binding energies of the orbital electrons involved. In addition to being dependent on the anode material, this kind of radiation also depends on the electron kinetic energy that must be greater than the ionization energy of K and L electrons. This process takes place also when the ionization is related to the outer-shell orbitals, but the energy of the characteristic emitted photons is too low to significantly pass through the filters and the exit window of the tube. While the characteristic radiation results in a discrete x-ray spectrum of characteristic peaks, the braking radiation (or bremsstrahlung) caused by the sudden deceleration of the incident electrons on the anode, shows a continuous spectrum. Due to the attenuation of the soft part of the spectrum by the exit window of the tube and the other added filters, this radiation shows a maximum relative intensity at approximately one-third of the maximum photon energy, as it can be seen from Figure 1.2. The maximum photon energy, instead, is given by the initial peak kinetic energy of the accelerated electrons. The complete tube assembly is finally mounted on a support and provided with collimation so that

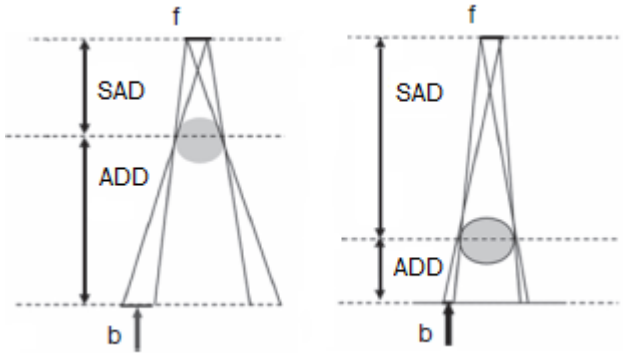

Figure 1.3: The effect of penumbra blurring (b) for the same focal spot size (f) of the x-ray tube. The penumbra is larger when the object is closer to the source (left hand side) than when the object is closer to the detector (right hand side).

the beam direction and the size of the radiation field may be varied as necessary. An unavoidable physical limitation of using an x-ray tube is the beam hardening effect due to the polychromatic beams and it will be further investigated in Chapter 4. The focal spot size also plays a fundamental role as it limits the image resolution. Even if an ideal detector with "perfect" spatial resolution is used, the image of any object will appear with blurred edges because of the finite dimension of the source. This effect is known as *penumbra blurring* (b) and is related to the focal spot diameter (f), the Axis to Detector Distance (ADD), and the Source to Axis Distance (SAD) by equation (1.1):

$$b = \frac{ADD}{SAD} f = (M - 1)f \tag{1.1}$$

where M is the magnification of the object, defined as $M = 1 + \frac{ADD}{SAD}$. Figure 1.3 shows what happens when the scanning is performed with the object closer to the source or to the detector. Most system work therefore with low or medium magnification, in the range $1.1<M<2$ in order to reduce this effect. High magnification is instead used in ex-vivo micro-CT or nano-CT scanners, where microfocus tubes with very small focal spots ($\leq 5\,\mu m$) are employed. Such sources are not suitable for in-vivo experiments because of their very low power, leading to scan times up to several hours that are unacceptably long when living subjects are studied.

1.1.2 X-rays interaction with matter

Attenuation is the reduction of the intensity of an x-rays beam as it traverses matter [1]. The reduction may be caused by either photoelectric absorption (energy is transferred from photons to atoms of the irradiated material) or by deflection (i.e.,

scattering) of photons from the primary beam, depending on the photon energy and on the sample composition. For monoenergetic x-rays, the attenuation in matter is quantitatively described by the Lambert-Beer's law:

$$I = I_0 \, e^{-\mu s} \tag{1.2}$$

where I_0 is the intensity of the unattenuated radiation, μ is the linear attenuation coefficient and I is the intensity of the transmitted beam after it has passed a layer of an homogeneous material of thickness s.
The linear attenuation coefficient is a measure for the attenuation per unit distance. It is specific for the used x-ray energy and for the type of target material. Consequently, equation (1.2) has to be adapted for inhomogeneous materials and polychromatic x-rays:

$$I = \int I_0'(E) \, e^{-\int \mu(E,s) \, ds} \, dE \tag{1.3}$$

where $I_0'(E)$ is the beam intensity per unit energy interval, thus I_0 is given by the integral of $I_0'(E)$ over the entire range of available energy in the spectrum:

$$I_0 = \int_0^{E_{max}} I_0'(E) \, dE. \tag{1.4}$$

The main types of interaction of X or gamma photons with matter are: Rayleigh, photoelectric, Compton, and pair production interactions.
Rayleigh scattering and pair production do not contribute to the CT signal. Rayleigh scattering, often referred to as coherent scattering, is a process in which an incident low energy photon interacts with the target atom as a whole [2]. Since there is any transfer energy to the target, it can be considered as a process of elastic scattering. Moreover, the deviation of the scattered photon from its original direction, is negligible for the x-ray energies here considered. Regarding pair production, it can only take place if the energy of the incident photon is greater than 1.02 MeV, that is an energy threshold higher than x-ray energies involved in micro-CT.
In the photoelectric effect, a photon of energy $h\nu$ interacts with a tightly bound atomic electron (i.e., an orbital electron of the inner atomic shells, generally K, L, and M, with binding energy E_b), transferring its energy to the electron, which receives a kinetic energy $E_k = h\nu - E_b$ and is ejected from the atom, as it is shown on the left side of Figure 1.4. The x-ray photon is thus completely absorbed. Therefore this process can take place with the given bound electron only if $h\nu > E_b$. The ejection of the electron from an atomic shell leaves a corresponding vacancy in that shell that is promptly filled by a higher shell electron, resulting in the emission of a fluorescence x-ray. The energy of this emitted photon is given by the difference between the binding energies of the two potential energy levels between which the electronic transition occurs. If the binding energy of the

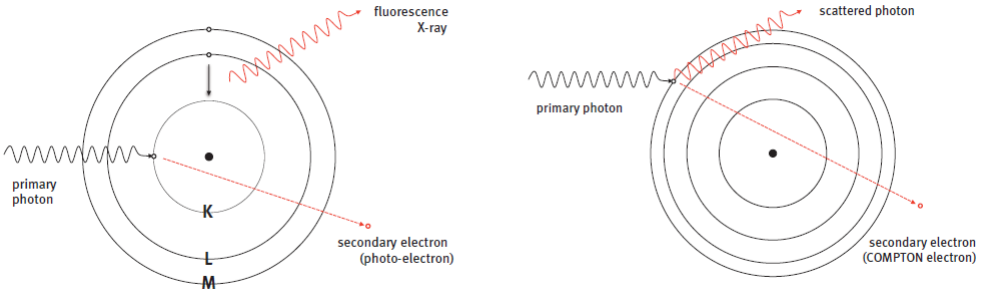

Figure 1.4: Schematic view of the photoelettric (on the left) and Compton (on the right) effect. Images are adapted from [2].

electron involved in the collision is negligible with respect to the energy of the incident photon, there is a low probability that photoelectric absorption occurs and the interaction can be modeled as a relativistic collision between a photon and an unbound, stationary electron. This usually happens for interactions with electrons of external orbitals, and the process is called incoherent or Compton scattering which is graphically shown on the right side of Figure 1.4. The term "scattering" suggests that the incident photon is not absorbed, but instead it is scattered in a different direction. It is also called "incoherent" because each scatter event involves a single electron instead of the atom as a whole, and hence the photons coming from each event have no coherence [2]. Photon is scattered at an angle ϕ with respect to the direction of incidence, emerging with an energy $h\nu'$ and giving the fraction $(h\nu - h\nu')/h\nu$ (not all) of its energy to the electron which is scattered at an angle θ with respect to the incident photon direction, with a kinetic energy $E_k = (h\nu - h\nu')$ as given by energy conservation. Taking into account also the conservation law for the total momentum, the kinematic relationships between ϕ, θ, $h\nu$, and $h\nu'$ of the Compton effect are obtained:

$$h\nu' = \frac{h\nu}{1 + \frac{h\nu}{m_e c^2}(1 - \cos\phi)} \tag{1.5}$$

$$\cot\theta = \left(1 + \frac{h\nu}{m_e c^2}\right)\tan\left(\frac{\phi}{2}\right). \tag{1.6}$$

From a macroscopic point of view, it is often necessary to quantify the attenuation of a photon beam through a known thickness of material. The atomic cross section, σ, represents the probability for a photon to undergo that interaction on a single atom [2]. The overall probability of interactions of a photon with a single atom or its nucleus is the sum of the cross sections for all the possible interactions:

$$\sigma_{\text{tot}} = \sum_i \sigma_i \quad . \tag{1.7}$$

The atomic cross section for the photoelectric effect, σ_{PE}, depends on the photon energy $h\nu$ and on the atomic number Z. In the energy range involved in micro-CT imaging, it can be approximated by the following expression [3]:

$$\sigma_{PE} \propto \frac{Z^4}{h\nu^3} \tag{1.8}$$

while the atomic cross section for the Compton scattering, $(\sigma_C)_{atom}$, depends on the atomic number Z and the Klein-Nishina total cross section $(\sigma_C)_{elec}$ in the following way:

$$(\sigma_C)_{atom} = Z(\sigma_C)_{elec}. \tag{1.9}$$

By multiplying the total cross section σ_{tot} with the number of atoms in the unit volume, one gets the total linear attenuation coefficient μ:

$$\mu_{tot} = \frac{N_A \rho}{A}\sigma_{tot} \tag{1.10}$$

where N_A is Avogadro's number, A is the mass number, and ρ the density of the chemical species. Just like atomic cross sections, the parameter μ depends on the incident photon energy and on Z and ρ of the target material.
As mentioned above, only the photoelectric and Compton scattering effects are important in the energy ranges commonly used in micro-CT imaging. Thus, the linear attenuation coefficient can be written as:

$$\mu_{tot} = \frac{N_A \rho}{A}\Big(\sigma_{PE} + (\sigma_C)_{atom}\Big). \tag{1.11}$$

1.1.3 X-rays detection

A radiation detector is used to measure the intensity of the x-rays transmitted through the object. The purpose of the detector is to convert the distribution of incident x-ray flux (dependent on the position and time of observation) into an electrical signal, which can be handled by conventional electronic techniques and then digitized for further processing and analysis on a computer.
The majority of micro-CT systems to date employ digital flat surface 2D detectors leading to a cone beam scanning geometry.
Combined detection systems made up of scintillator screens coupled to Charge Coupled Device (CCD)s via fiber-optic bundles, with various demagnifying ratios, is the standard for micro-CT imaging. Nevertheless, the advance in Complementary Metal Oxide Semiconductor (CMOS) technology lead to the production of large area detectors with high frame rates, making them the most widely used detectors for in vivo small animal imaging systems. Also reported in the literature

are studies on the use of direct conversion detectors coupled to Thin Film Transistor (TFT) arrays and of single pixel or small area detectors operating in photon counting mode.
Thallium-doped Cesium Iodide (CsI:Tl) and Gadolinium Oxysulfide are the most used scintillator screens. CsI:Tl screens with thickness of about 150-200 µm are shown to be a good compromise between efficiency and spatial resolution, also thanks to a columnar-grown structure that reduces the spread of the visible light generated at the site of interaction of the x-ray photon. On the other hand, the high atomic number of gadolinium allows drastic reduction in the thickness of the scintillator layer (by a factor of 3 or more) and thus the light spreading while keeping comparable detection efficiency with respect to Cesium Iodide (CsI). The Energy Absorption Efficiency (EAE) is an important parameter to take into account since it plays a fundamental role in photon detection. It is defined as

$$\mathrm{EAE} = \frac{\int_{E=0}^{E_{\max}} \mathrm{I}_0'(E) E \left(\frac{\mu_{\mathrm{en}}(E)}{\mu(E)}\right) (1 - \mathrm{e}^{-\mu(E)x})\, \mathrm{d}E}{\int_{E=0}^{E_{\max}} \mathrm{I}_0'(E) E\, \mathrm{d}E} \tag{1.12}$$

where x is the thickness of the detector, $\mu(E)$ is its linear attenuation coefficient, $\mu_{\mathrm{en}}(E)$ is its absorption coefficient and $\mathrm{I}_0'(E)$ is the x-ray spectrum [5]. This quantity is related to the Quantum Efficiency (QE) of the detector, providing useful information on the fraction of photons that actually contribute to the signal formation, resulting in a loss of information.
When high spatial resolution is requested, detector pixels have sizes in the range of 50-100 µm so that the CCD or CMOS array is generally a few square centimetres large. This limits the maximum size of the object (i.e., the Field of View (FOV)) that can be scanned.
The photons produced by scintillator are then transferred to a light sensitive sensor either by direct close contact or by an imaging optical element. Digital detectors are based upon a sensor that consists of a matrix of cells, or pixels, on a semiconductor substrate.
In case of a CCD sensor, the charges, in columns of pixels, are sequentially moved column by column to an output registry column. During each period of column transfer, the content of the whole output registry column is sequenced into an output cell, from which it is further preamplified and fed out. In CMOS sensors, each pixel in the matrix could be accessed and read in a random fashion. In practice, they are also read sequentially, pixel by pixel and in most cases with an interlaced readout. Each pixel is associated with an individual preamplifier to preserve the charge-to-voltage conversion from being affected by the capacity of the output line and hence by the position of the pixel in the matrix [4].
The differences between the two types of readout architectures are diverse. Very briefly, we can state that such differences regard mainly the following parameters:

- frame rate, since a CMOS pixel generates directly an analogical signal in spite of a CCD pixel that produces charges;
- image uniformity, because CCD pixels have the same amplifier which is reflected in a less gain pixel differences than in CMOS pixels;
- fill factor, as CMOS pixels have a less area for photoreception since they contain many features to processing and control signal.

1.2 Image reconstruction

The aim of tomographic reconstruction is to recover the distribution of the linear attenuation coefficients μ on a section of the object being scanned. μ, as already explained above, is a function of Z of the traversed material, ρ, the material density, and E, the photon incident energy. If ρ and Z are both functions of the position $r = (x, y, z)$ in the material, (let us neglect the dependence on time for the following discussion) it is possible to state that

$$\mu = \mu(r, E). \tag{1.13}$$

The result after the acquisition of the raw scan data in CT is not $\mu(r, E)$, but rather a set of its *line integrals* over all possible lines intersecting the object and passing through the focal spot size and each of the detector pixels, for all the gantry angles. A line integral, as the name implies, represents the integral of some parameter of the object along a line. In this case, a line integral represents the total attenuation suffered by a beam of x-rays as it travels in a straight line through the object [6]. Because the vast majority of x-ray detectors used today in CT work as energy-integrating devices, the information on the photon energy E is lost and hence we will just deal with line integrals of a energy-averaged (or energy-weighted) version of $\mu = \mu(r)$. The complete set of line integrals on the plane of the x-ray source trajectory (assumed to be circular in this context) is called the (2D) Radon transform of the object function $\mu(r)$. In the terminology of tomography, the graphical representation of Radon transform of a function is called sinogram. This term comes just from the fact that each point in the object space is mapped on a sinusoid in the projection space (or Radon space). In other words, the final goal of tomographic reconstruction is to invert the Radon transform of $\mu(r)$. The simplest projection is a collection of parallel ray integrals: it could be measured, for example, by moving an x-ray source and detector along parallel lines on opposite sides of an object[1]. Another type of projection is possible if a single source is placed in

[1]This scanner geometry was implemented in the EMI Mark I Hounsfield's scanner in the 70s.

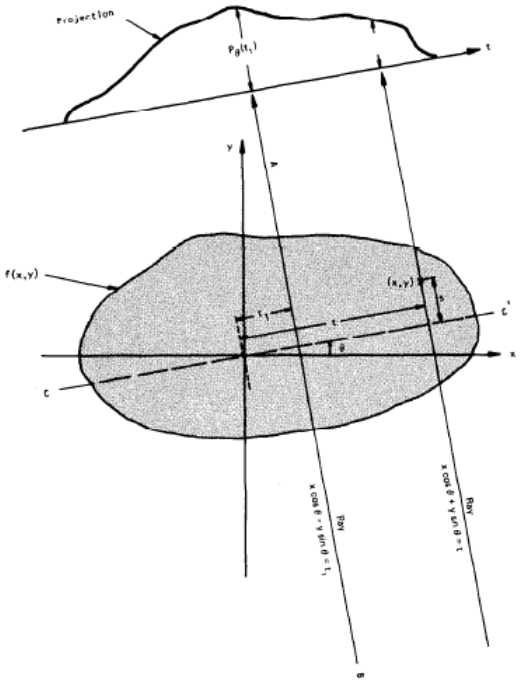

Figure 1.5: An object, $f(x, y)$, and his projection $P_\theta(t_1)$, are shown for an angle of θ. The figure is adapted from [6].

a fixed position relative to a line of detectors and it is known as a fan beam projection because the line integrals are measured along fans[2]. This section will discuss the well known reconstruction algorithm based on the Fourier slice theorem and the FBP for parallel beam. First, an overview is given about the theory of line integrals and projections.

1.2.1 Line integrals and projections

The coordinate system defined in Figure 1.5 will be used to describe line integrals and projections. In this example the object is represented by a 2D function $f(x, y)$ and each line integral by the (θ, t) parameters. The equation of a ray that travels through the object with an angle of incidence θ and a distance t with respect to the origin is given by:

$$x \cos\theta + y \sin\theta = t \tag{1.14}$$

[2]As done in single-slice third generation scanners, now obsolete after the introduction of multi-slice detectors.

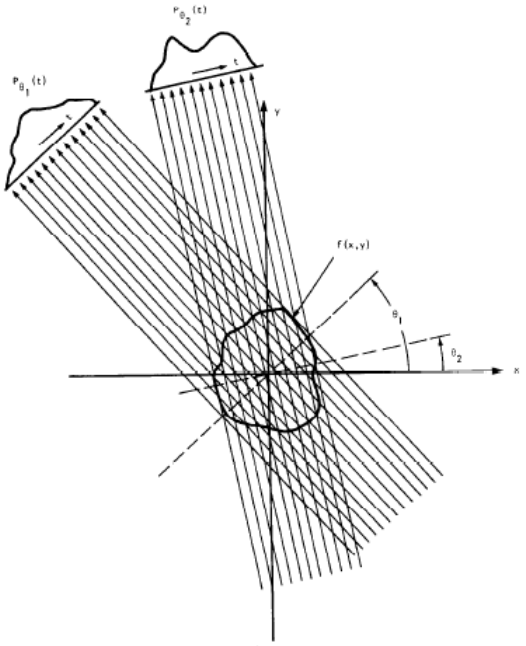

Figure 1.6: Parallel projections are taken by measuring a set of parallel rays for a number of different angles. The figure is adapted from [6].

this relationship is used to define line integral $\mathrm{P}_\theta(t)$ as

$$\mathrm{P}_\theta(t) = \int_{-\infty}^{+\infty} f(t, s)\,\mathrm{d}s \tag{1.15}$$

where s is the coordinate orthogonal to t and corresponds to the thickness traversed by the ray beam. Using a delta function, equation (1.15) can be written as

$$\mathrm{P}_\theta(t) = \int_{-\infty}^{+\infty}\int_{-\infty}^{+\infty} f(x, y)\delta(x\cos\theta + y\sin\theta - t)\,\mathrm{d}x\,\mathrm{d}y \tag{1.16}$$

This function is known as the Radon transform of the function $f(x, y)$ for a parallel projection geometry that is shown in Figure 1.6. Radon stated that, if a suffcient number of projections from different angles is available, one can reconstruct the image of the attenuation map from these functions [7].

1.2.2 The Fourier slice theorem

The Fourier slice theorem relates Radon data to a radial profile in Fourier space. It states that the One-dimensional (1D) Fourier transform of a parallel projection is equal to a slice of the 2D Fourier transform of the original object. It follows

that, given the projection data, it should then be possible to estimate the object by simply performing a 2D inverse Fourier transform. Therefore let us start by defining the 2D Fourier transform of the function $f(x, y)$ as

$$F(u, v) = \int_{-\infty}^{+\infty} \int_{-\infty}^{+\infty} f(x, y)\, \mathrm{e}^{-\mathrm{i}2\pi(ux+vy)}\, \mathrm{d}x\, \mathrm{d}y \tag{1.17}$$

and the Fourier transform of the projection $\mathrm{P}_\theta(t)$

$$\mathrm{S}_\theta(w) = \int_{-\infty}^{+\infty} \mathrm{P}_\theta(t)\, \mathrm{e}^{-\mathrm{i}2\pi wt}\, \mathrm{d}t \tag{1.18}$$

If we consider the Fourier transform of the object along the line in the frequency domain given by $v = 0$, the equation (1.17) simplifies into

$$F(u, 0) = \int_{-\infty}^{+\infty} \int_{-\infty}^{+\infty} f(x, y)\, \mathrm{e}^{-\mathrm{i}2\pi ux}\, \mathrm{d}x\, \mathrm{d}y \tag{1.19}$$

but because the phase factor is no longer dependent on y, the integral can be split into two parts,

$$F(u, 0) = \int_{-\infty}^{+\infty} \left[\int_{-\infty}^{+\infty} f(x, y) dy \right] \mathrm{e}^{-\mathrm{i}2\pi ux}\, \mathrm{d}x. \tag{1.20}$$

It can be noticed that the term in the brackets is recognized as the equation for a projection along lines of constant x or

$$\mathrm{P}_{\theta=0}(x) = \int_{-\infty}^{+\infty} f(x, y)\, \mathrm{d}y \tag{1.21}$$

Substituting this in equation (1.19), it results that:

$$F(u, 0) = \int_{-\infty}^{+\infty} P_{\theta=0}(x)\, \mathrm{e}^{-i2\pi ux}\, \mathrm{d}x. \tag{1.22}$$

The right-hand side of this equation represents the 1D Fourier transform of the projection $\mathrm{P}_{\theta=0}$, therefore

$$F(u, 0) = \mathrm{S}_{\theta=0}(u). \tag{1.23}$$

This equation represents the simplest form of the Fourier slice theorem. Clearly this result is independent of the orientation between the object and the coordinate system. If an image $f(x, y)$ is rotated by an angle θ with respect to the x-axis, the Fourier transform $F(u, v)$ will be correspondingly rotated by the same angle with respect to the u-axis, which can be seen in Figure 1.7. The derivation of the Fourier Slice Theorem can be placed on a more solid foundation by considering

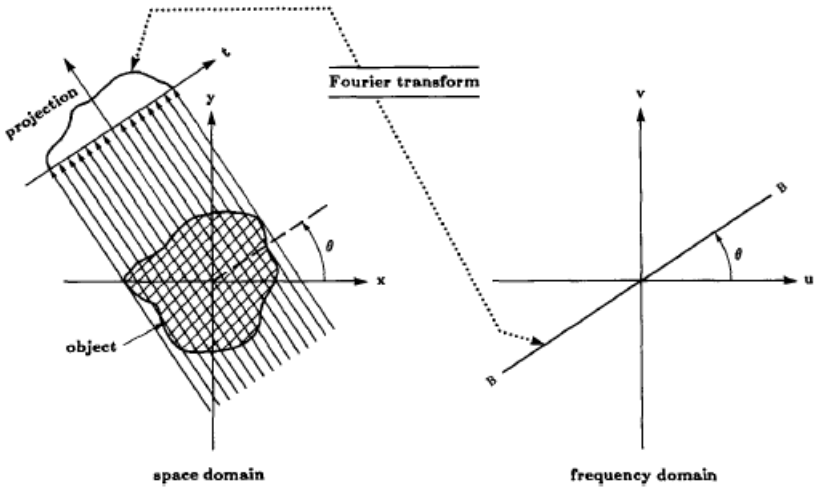

Figure 1.7: The Fourier slice theorem relates the Fourier transform of a projection to the Fourier transform of an object along a radial line. The figure is adapted from [6].

the (t, s) coordinate system to be a rotated version of the original (x, y) system as expressed by

$$\begin{bmatrix} t \\ s \end{bmatrix} = \begin{bmatrix} cos\theta & sin\theta \\ -sin\theta & cos\theta \end{bmatrix} \begin{bmatrix} x \\ y \end{bmatrix}. \tag{1.24}$$

In the (t, s) coordinate system a projection along lines of constant t is written

$$\mathrm{P}_\theta(t) = \int_{-\infty}^{+\infty} f(t, s)\,\mathrm{d}s \tag{1.25}$$

and the Fourier transform is given by

$$\mathrm{S}_\theta(w) = \int_{-\infty}^{+\infty} \left[\int_{-\infty}^{+\infty} f(t, s)\,\mathrm{d}s \right] \mathrm{e}^{-2\mathrm{i}\pi w t}\,\mathrm{d}t. \tag{1.26}$$

This result can be transformed into the (x, y) coordinate system by using the relationship (1.24):

$$\mathrm{S}_\theta(w) = \int_{-\infty}^{+\infty} \int_{-\infty}^{+\infty} f(x, y)\,\mathrm{e}^{-\mathrm{i}2\pi w(x\cos\theta + y\sin\theta)}\,\mathrm{d}x\,\mathrm{d}y. \tag{1.27}$$

The right-hand side of this equation now represents the 2D Fourier transform at a spatial frequency of $(u = w\cos\theta, v = w\sin\theta)$, that is

$$\mathrm{S}_\theta(w) = F(u, v) = F(w\cos\theta, w\sin\theta). \tag{1.28}$$

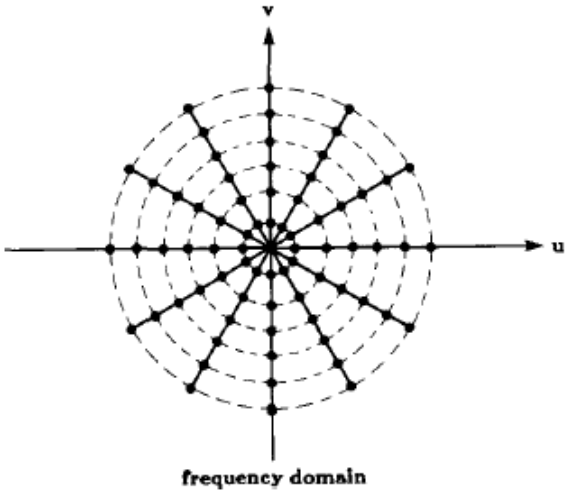

Figure 1.8: As a consequence of the Fourier Slice Theorem, collecting projections of the object at a number of angles provides estimates of the Fourier transform of the object along radial lines. The figure is adapted from [6].

This equation is the cornerstone of projection tomography and proves the Fourier slice theorem. This basis result indicates that by taking the projections of an object function at angles $\theta_1, \theta_2, ..., \theta_k$ and Fourier transforming each of these, the values of $F(u, v)$ can be determined on radial lines, as shown in Figure 1.7. If an infinite number of projections are taken, then $F(u, v)$ would be known at all points of the uv-plane. In practice only a finite number of projections can be taken. In that case it is clear that the function $F(u, v)$ is only known along a finite number of radial lines such as in Figure 1.8.

1.2.3 The Filtered Back Projection

The algorithm that is currently being used in almost all applications of straight ray tomography is the filtered back projection algorithm. It has been shown to be extremely accurate and will be derived by using the Fourier slice theorem. Recalling the formula for the inverse Fourier transform, the object function, $f(x, y)$, can be expressed as

$$f(x, y) = \int_{-\infty}^{+\infty} \int_{-\infty}^{+\infty} F(u, v)\, \mathrm{e}^{\mathrm{i}2\pi(ux+vy)}\, \mathrm{d}u\, \mathrm{d}v. \tag{1.29}$$

Exchanging the rectangular coordinate system in the frequency domain, (u, v), for a polar coordinate system, (w, θ), by making the substitutions

$$u = w \cos\theta \tag{1.30}$$

$$v = w \sin\theta \tag{1.31}$$

and then changing the differentials by using

$$\mathrm{d}u\,\mathrm{d}v = w\,\mathrm{d}w\,\mathrm{d}\theta \tag{1.32}$$

equation (1.29) can be rewritten as

$$f(x,y) = \int_0^{2\pi}\int_0^{\infty} F(w,\theta)\,\mathrm{e}^{\mathrm{i}2\pi w(x\cos\theta + y\sin\theta)}\,w\,\mathrm{d}w\,\mathrm{d}\theta. \tag{1.33}$$

This integral can be split into two by considering θ from 0 to π and from π to 2π. Then using the property of Fourier transformations

$$F(w,\theta+\pi) = F(-w,\theta) \tag{1.34}$$

equation (1.33) may be written as

$$f(x,y) = \int_0^{\pi}\left[\int_{-\infty}^{+\infty} F(w,\theta)|w|\,\mathrm{e}^{i2\pi wt}\,\mathrm{d}w\right]\mathrm{d}\theta \tag{1.35}$$

and appliying the Fourier slice theorem

$$f(x,y) = \int_0^{\pi}\left[\int_{-\infty}^{+\infty} \mathrm{S}_\theta(w)|w|\,\mathrm{e}^{\mathrm{i}2\pi wt}\,\mathrm{d}w\right]\mathrm{d}\theta. \tag{1.36}$$

This integral may be expressed as

$$f(x,y) = \int_0^{\pi} \mathrm{Q}_\theta(x\cos\theta + y\sin\theta)\,\mathrm{d}\theta \tag{1.37}$$

where

$$\mathrm{Q}_\theta(t) = \int_{-\infty}^{+\infty} \mathrm{S}_\theta(w)|w|\,\mathrm{e}^{\mathrm{i}2\pi wt}\,\mathrm{d}w. \tag{1.38}$$

Equation (1.38) represents a filtering operation, where the frequency response of the filter is given by $|w|$. From equation (1.18) it is known that $\mathrm{S}_\theta(w)$ is the 1D Fourier transformation of $P_\theta(t)$ and thus

$$\mathrm{Q}_\theta(t) = \mathrm{P}_\theta(t) \otimes \mathrm{h}(t) \tag{1.39}$$

with $\mathrm{h}(t)$ a filter function defined as $\mathrm{h}(t) = \mathcal{F}(|w|)$. The filter function $|w|$ is not transformable according Fourier less than insert some cut-off frequencies. Therefore $\mathrm{Q}_\theta(t)$ is called a *filtered projection*. The resulting projections for different angles θ are then added to form the estimate of $f(x,y)$. Equation (1.37) expresses that each filtered projection Q_θ is *back projected*. This can be explained as follows. To every point (x,y) in the image plane there corresponds a value of $t = x\cos\theta + y\sin\theta$ for a given value of θ. The filtered projection, Q_θ contributes

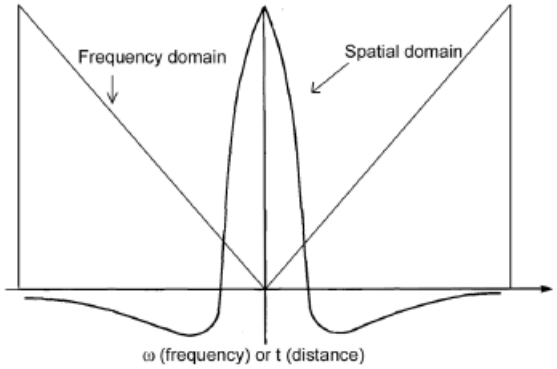

Figure 1.9: Schematic view of the ramp filter h(t) in the spatial domain and $|w|$ in the frequency space.

to the reconstruction of t ($= x\cos\theta + y\sin\theta$). Furthermore, the filtered projection, Q_θ, will make the same contribution to the reconstruction at all of the points along a line. Therefore, one could say that in the reconstruction process each filtered projection, Q_θ, is smeared back, or back projected, over the image plane. The filter h(t), also known as ramp filter because of its shape in the frequency domain, represents an ideal inversion filter in frequency space, and is shown in Figure 1.9. Every image point of a projection line is represented in Fourier space as a point on the corresponding line. From Figure 1.8 it is clear that, using several projections, the information at low frequencies (near the origin) is overemphasized, as compared to the information at high frequencies. This effect is compensated by the $|w|$ filter, which is a ramp filter that puts a linear weight in Fourier space to reduce the low spatial frequencies and enhance the high ones. The ramp filter is generally composed (i.e., multiplied in the frequency domain) of additional "windows", whose shape depends on whether it is desired to emphasize edges (at cost of worsening the image noise) or attenuate the image noise (in which case there will be a loss of image sharpness). Basically, such apodization windows act as tools for fine-tuning the high frequency content of the reconstructed image, which is the part of the frequency spectrum containing information on sharp edges. Different windows are available with different frequency response characteristics. Choosing an optimal window for a specific application requires knowledge of the signals involved, consideration of the frequency resolution, and the dynamic range requirements. The most used windows in this field of the digital signal processing, besides the simplest window that is the boxcar (or rectangular) window, are the Hanning, the Hamming, the Blackman windows. As an example of the structure

of a window function, the Hanning window fuction is reported in equation (1.40):

$$\mathrm{w}(n) = \frac{1}{2}\left(1 - cos\left(\frac{2\pi n}{\mathrm{N}-1}\right)\right), \quad 0 \leq n \leq \mathrm{N}-1 \tag{1.40}$$

where N represents the number of samples, that is the width of the window. In fan-beam geometry, the above formula for reconstruction of parallel-ray data is simply modified by suitable coordinate trasformation in order to take into account the geometrical magnification, and the different length of the lines of projections for different pixel positions on the detector array. This leads to a reconstruction formula similar to equation (1.38), where weighting factors are included before ramp-filtering.

1.2.4 The Feldkamp-Davis-Kress Algorithm

Reconstruction of raw data set is generally perfomed via the Feldkamp-Davis-Kress (FDK) back-projection algorithm, which is an approximated algorithm for reconstruction of cone-beam data from circular scan orbits [8]. The basic idea of the FDK method is to:

1. weight projection data by taking into account the increased length of the lines of projections away from the transaxial midplane;

2. filter the measured data along each row of the detector as if it were part of a 2D fan-beam acquisition;

3. perform 3D back projection.

However, exact 3D reconstruction for a circular trajectory is impossible because the set of cone-beam projection data from circular scans do not satisfy Tuy-Smith's condition. Briefly, the Tuy-Smith sufficiency condition is satisfied when all the planes intersecting the object also intersect the trajectory of the source, at least in one point [9]. Despite its approximated nature, the image quality of the reconstructed images is acceptable for small cone angles. When the axial aperture of the cone-beam is increased, an underestimation of the reconstructed μ's is observed in peripheral slices. Indeed, the FDK algorithm is an exact reconstruction algorithm only for objects that are shift invariant along the z-axis (e.g., cylinders or prisms).

1.2.5 The Hounsfield Unit

The physical quantity that is finally reconstructed is somewhat conceptually different from the linear attenuation coefficient μ because of the polychromatic x-ray

beam. In fact if we try to compute the line integral p of the linear attenuation coefficients calculating the logarithm of the intensity ratio, as derived for monoenergetic radiation (see from equation (1.2)), we will get

$$\mathrm{p} = -\ln \frac{\int \mathrm{I}_0'(E)\, \mathrm{e}^{-\int \mu(E,s)\,\mathrm{d}s}\,\mathrm{d}E}{\int_0^{E_{max}} \mathrm{I}_0'(E)\,\mathrm{d}E} \neq \int_{\mathrm{L}} \mu\,\mathrm{dL}. \tag{1.41}$$

Even though p as calculated by equation (1.41) is not equal to the line integral of μ at any precise energy, unless monochromatic radiation is employed, we still use that log-transformed ratio of measured intensities in polychromatic CT to estimate the value of the line integral of μ at some "effective" energy. This is due to the absence of spectral information in most x-ray radiation detectors used to date. Thus in the case of polychromatic CT, it is more correct to speak about effective linear attenuation coefficient, μ_{eff}, just because it is obtained by integrating the real μ over a finite interval of x-ray energies (see equation (1.3)). For this reason, image reconstructed data are expressed in CT numbers that can be defined as the relative variation of a voxel value with respect to water:

$$\mathrm{CT} = 1000 \times \frac{\mu_{\mathrm{eff,voxel}} - \mu_{\mathrm{eff,water}}}{\mu_{\mathrm{eff,water}}}, \tag{1.42}$$

where the effective linear attenuation coefficient of water ($\mu_{\mathrm{eff,water}}$) has to be measured in the same experimental conditions of the whole image. The unit of measurement for CT numbers is the Hounsfield Unit (HU). Directly from the equation above, it follows that the CT number for water corresponds to 0 HU, whereas denser and softer materials have positive and negative CT numbers, respectively. For instance, the CT number of air is approximately -1000 HU.

1.3 General applications of micro-CT

Research on small-animal models of human diseases is critical to our understanding of the origin, progression, and treatment of diseases. The mouse is a commonly studied animal for such research because of the large, established information on its genome, its rapid rate of reproduction, and relatively low husbandry costs. However, its small size presents severe challenges for morphological and functional analysis. Thanks to the high spatial resolution scan and the 3D visualization capability of the system that can be used for non-invasive imaging of different organs, micro-CT can provide a reliable platform for small animal imaging. It arises as a tool for the morphological imaging; the first reported studies concerned in fact with bone architecture and density. They drove the early developments of micro-CT systems, also thanks to the large difference in x-ray attenuation

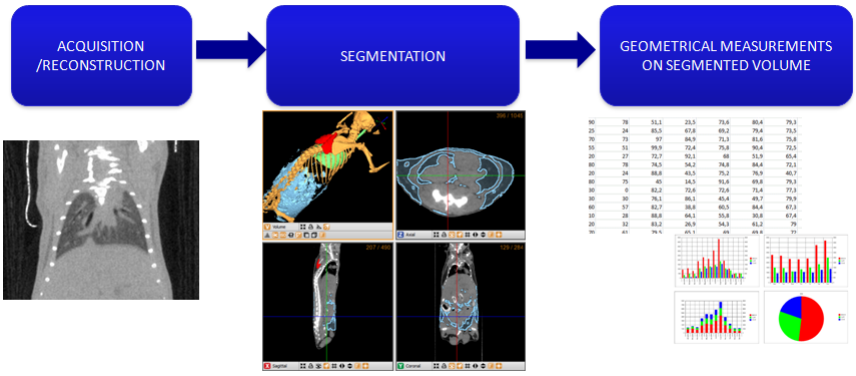

Figure 1.10: Schematic of the segmentation process leading to the quantification of the morphometric parameters.

(or "contrast") between the bone and soft tissue. Micro-CT data are in most cases more informative and quantitative compared with 2D histological examination (which is, unlike micro-CT, a destructive tecnique), allowing the quantification of 3D morphometric parameters such as volumetric bone mineral density, bone volume ratio, bone surface ratio, and trabecular thickness [10]. Morphometry is performed on a binary image obtained by segmenting the original micro-CT volume. In most cases, due to the high contrast between bone, marrow and muscle, simple threshold-based segmentation is sufficient for both cancellous and cortical bone segmentation on micro-CT images of adequate spatial resolution. The majority of the segmentation methods are based on the analysis of a histogram of image intensities. In Figure 1.10 the procedure leading to the quantification is illustrated. Micro-CT plays also a fundamental role in osteoporosis research and in the field of regenerative medicine, as it enables to accurately determinate three-dimensional structure of engineered bone scaffolds, with particular emphasis on porosity and connectivity [11]. Enabled by the inherent contrast between air and tissue, micro-CT is a powerful modality for lung imaging too despite the small size of the organs and the rapid respiratory motion. It can be used successfully to study various lung disease models, such as emphysema and fibrosis. For vascular and cardiac imaging, the use of CAs is required in order to discriminate vessels from soft tissues and myocardium from the blood, respectively. In Figures 1.11(a) and 1.11(b) two examples of how the injection of a CA make possible to visualize the vascular network of a small animal are reported. Global cardiac functional metrics such as cardiac output, stroke volume, ejection fraction, and regional myocardial thickness can be computed recurring to the Time-resolved three-dimensional (or four-dimensional) (4D) micro-CT imaging which will be described in the next section.

Micro-CT has proven to be also useful in tumor detection, progression, and imag-

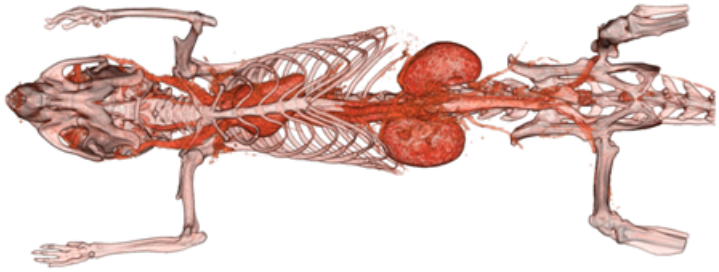

(a)

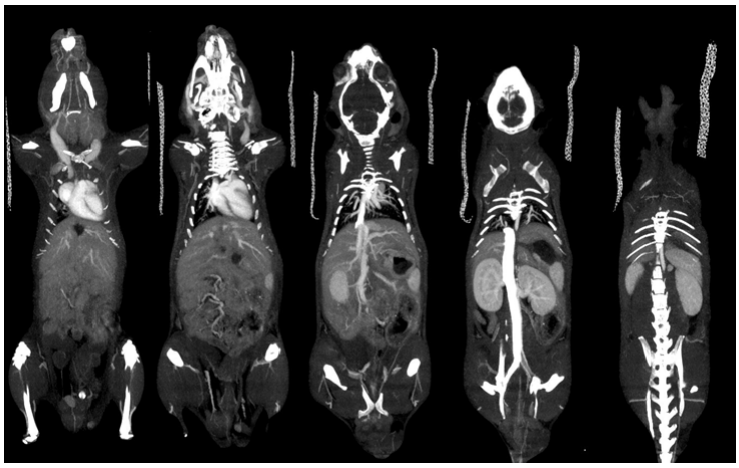

(b)

Figure 1.11: 1.11(a): Image of mouse injected with iodinated contrast agent. 1.11(b): Maximum intensity projection (MIP) of a whole body multi-bed scan of a mouse. They are reported just to emphasize the visualization of the vascular network over time thanks to the injection of CA. All images were provided by the Institute of Clinical Physiology of the National Research Council, in Pisa.

ing tumor angiogenesis [12, 13]. Cancer imaging is related to the use of CAs, even though the imaging of lung tumors is generally performed without the administration of a CA. However, in some lung disease models, the use of nanoparticle based CA may be beneficial, since it may allow the assessment of the vascular density of the lung or even vascular permeability of tumors via enhanced permeability and retention [14].
Another way in which micro-CT can be used is by combining it with other imaging modalities, such as PET or SPECT. In fact, although very sensitive, the nuclear imaging methods are limited by poor spatial resolution which becomes an issue when imaging small animal. Micro-CT is therefore useful in providing anatomical reference and also enables corrections of γ-ray attenuations through tissue. An extensive review of the applications of micro-CT in the biomedical context can be found in [15].

1.4 4D micro-CT imaging

In the previous paragraph, the main applications taking advantages of the extensive morphological information that micro-CT can provide have been briefly reviewed. There is however a significant interest also in functional micro-CT imaging which has the additional requirement of generating 3D images with an adequate temporal resolution. Time-resolved, or dynamic, 3D imaging, is nowadays referred to as 4D imaging, which is at the basis of all the image processing strategies giving rise to quantitative functional information. However, there are considerable challenges in scaling all imaging modalities to the temporal and spatial resolution required for mice and rats since a mouse heart is only about 5 mm in diameter and can beat up to 600 times/minute. In addition the limitations due to radiation dose must be considered in order to avoid radiation-related injuries while keeping high the spatial resolution. Let us just think that, for an ideal quantum-noise limited CT scanner, the image noise is proportional to the inverse of $\Delta x^2 \sqrt{D}$ [16], where Δx is the dimension of the isotropic voxel, and D is the radiation dose delivered to the small animal. This means that keeping the spatial resolution high, will result in a significantly Signal to Noise Ratio (SNR) decrease, if the x-rays exposure to the animal is held constant relative to that in the clinical setting. Relationships between all these variables so determinants will be analyzed in the course of this thesis with the aim to understand how dynamic imaging is an arduous challenge.

1.4.1 4D phase-correlated micro-CT

The term "4D micro-CT imaging" also refers to "phase-correlated" imaging in which cardiorespiratory-gating strategies are employed during in vivo scanning in order to capture the physiological motion. Unless not acquired with very high dose the reconstructed phase-correlated images show severe streak artifacts, image noise is very high and anatomical details vanish in the noise.
4D phase-correlated micro-CT used in cardiopulmonary studies typically employs either Prospective Gating (PG) or Retrospective Gating (RG). In PG, acquisition is triggered by the coincidence of a selected respiratory phase and a selected cardiac phase. This produces a set of projections with a constant angular step, resulting in reconstructed images that are free of streaking artifacts. However, because of the time spent waiting for the coincidence of cardiac and respiratory events, the scan time can take as long as one hour to cover 10 different phases of the cardiac cycle [17]. In RG, the projection images are acquired at a rapid and constant rate without waiting for cardiac and respiratory coincidence. Respiratory and electrocardiogram (ECG) signals are monitored and saved in synchrony with the acquisition of the projections. Postsampling using these signals, the projections are retrospectively sorted into different subsets corresponding to different cardiac and respiratory phases. With this protocol, the scan time can be shortened, but the irregular angular distribution causes streaking artifacts in the FBP-based reconstructed images, as reported in [17]. Some investigator has recently tried to overcome the limitations of PG and RG, by mean of a hybrid gating strategy called Fast Prospective Gating (FPG) [18]. In FPG, multiple projections are acquired at the same angle, corresponding to all cardiac or respiratory phases to be reconstructed, before the cradle is rotated to the next angle[3]. FPG requires on-the-fly computation of the triggering events, which are delayed from the peaks of the respiratory or cardiac signals.

1.4.2 Time-resolved 3D imaging

The novel interest in dynamic CT imaging reflects on the possibility of CA kinetic modeling for estimation of functional parameters. Moreover the value of perfusion CT is recognized in neurology, cardiology, and oncology. All such applications are based on the analysis of the temporal evolution of tissue contrast enhancement after the injection of the CA and on the differences on time dependence of the enhancement between normal and impaired tissues. Thus, time-resolved micro-CT imaging can be used for longitudinal imaging. Dynamic micro-CT has also been applied to the direct measure of perfusion in tumors following the injection of conventional CA [20, 21]. CT perfusion measurements enable in fact the

[3]Reseachers of the mentioned article ([18]) use a rotating specimen geometry on vertical axis.

quantitative evaluation of functional parameters such as blood flow and blood volume. However, to accurately calculate functional parameters with standard methods a high temporal resolution of the first pass kinetics of the contrast material bolus is required, but it remains a challenge in small animal Dynamic Contrast-Enhanced (DCE) micro-CT [22]. In dynamic micro-CT applications the functional parameters can be for example obtained using a two-compartment model and describing the one-way transfer of the CA from the intravascular space to the extravascular space as done by Eisa et al. This method is not based on the first pass kinetics of the contrast agent, but on the delayed phase. Because the contrast dynamics in the delayed phase are slower, reduced temporal sampling is acceptable [22]. In Figure 1.12 an example of TACs are reported.

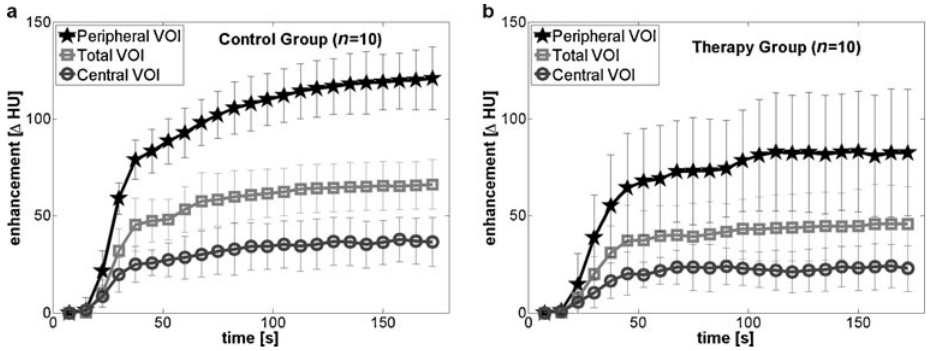

Figure 1.12: Example of Time Attenuation Curve (TAC)s with standard deviations for the peripheral, total and central tumour Volume of Interest (VOI) for the control group (a) and the therapy group (b). The image is adapted from [22].

Chapter 2

The IRIS PET/CT scanner

Introduction

The scanner PET/CT IRIS (Inviscan Sas, Strasbourg, France) is a multimodal preclinical tomograph for high resolution PET/CT imaging of small animals. One of these scanners is operating at the Institute of Clinical Physiology of the National Research Council, in Pisa (Figure 2.1). The hardware and software characteristics of the IRIS scanner will be presented, focusing mainly on the CT component.

2.1 The IRIS PET component

The PET component of the scanner consists of 16 modular detectors arranged in two octagonal rings. Each detector module can acquire coincidences with the six opposing modules of which three belong to the same ring and three belong to the other one. The IRIS/PET FOV results in a lenght of 95 mm in the axial direction, with a diameter of 80 mm. Each detector module consists of a matrix of 702 lutetium-yttrium orthosilicate crystals doped with cerium (LYSO:Ce) of 1.6 mm $\times$1.6 mm $\times$12 mm with a pitch of about 1.7 mm. The detector is directly coupled to a 64 anodes PhotoMulTiplier (PMT) (H8500C, Hamamatsu Photonics K.K., Hamamatsu, Japan) and each of them is completely independent from the others, with no light guide between scintillator and PMT. The same modularity is implemented at the level of the acquisition electronics. The output signals from each PMT pass through a conditioning stack made of a coding board, a pulse shape preamplifier and a timing board. The coding board consists of a Symmetric Charge Division (SCD) resistive network, which is implemented for its simplicity and good performance. The SCD reduces the 8$\times$8 signals of each PMT into 8x + 8y signals which in turn are further reduced to four, (XA, XB ,YA, YB), by a passive resistive chain. The position signals are then sent to 16

Figure 2.1: The scanner PET/CT IRIS. The image is adapted from http://www.inviscan.fr/gallery.htm .

Data Acquisition (DAQ) boards based on 12-bit A/D converters. Events from two detectors are accepted when their arrival time is within a maximum difference of 2.6 ns, corresponding to an actual coincidence window of 5.2 ns. Random events are acquired using a symmetrical delayed window technique and implementing a random single event acquisition. The coincidence processor rejects multiple coincidences. Events are sent to the local DAQ PC in the form of data packets with rate-dependent size and are stored in a list-mode format. The list-mode format contains the four position signals, the detector module identifier, and other event tags such as gating signals or random coincidence flag. Each data packet includes the information on the coarse time stamp, together with the single, the coincidence and the random count rates. Images can be reconstructed with both sinogram based 2D-FBP and with a multi-core Line of Response (LOR) based 3D Maximum Likelihood Expectation Maximization or Ordered Subset Estimation Maximization (OS-EM). Events can be corrected for dead-time and decay-time and attenuation correction is implemented with a CT-based-attenuation map.

2.2 The IRIS CT component

The PET/CT IRIS can be fully controlled by the user with a web-based Graphical User Interface (GUI). It allows the user to create animal studies and multimodality acquisition workflows, including the possibility of customizing both

the post-processing and the image reconstruction protocols parameters. The same GUI is used for hardware control and monitoring. The CT section is equipped with a microfocus x-ray source and with a flat-panel x-ray detector that will be further descripted in the following sections. CT images are reconstructed using a Feldkamp-type FBP algorithm on a dedicated workstation equipped with two Intel Xeon CPU, working under a Linux x64 operating system, where data are automatically transferred and processed at the end of the study. All reconstructed images are calibrated in HU, converted in a DICOM3 compliant image format and exported to a local DICOM server [23].

The choice of the scanning protocol depends substantially on the kind of specimen to be examined and consequently on the dose level that it can be delivered, trying in the same time to get the better spatial resolution that is possible. Three types of protocol are available for the IRIS scanner according to their function:

- CT or PET acquisition protocols. For a CT acquisition, the parameters to set are those that substantially determine the dose level to the patient, as the tube voltage, the cathode current, the exposure time per frame, and the number of projection views.

- Preprocessing protocols allow the preparation of raw data before reconstruction. They request to take a decision about the cropping (dimensions of the FOV), as to discard unuseful data when objects smaller than FOV are scanned, and voxel size.

- Reconstruction protocol by which preprocessed data are finally reconstructed. Here the apodization window can be selected and pre-corrections for ring artifacts and beam-hardening can be applied.

CT data are typically acquired in Full Scan (FS) or in Short Scan (SS) mode, corresponding to a full (360°) or partial (180° + fan-angle of the projection) rotation of the gantry around the specimen, respectively. The SS acquisition modality enables to greatly reduce the acquisition time, with a consequent reduction of the dose absorbed and an increase in the temporal resolution.
The available tube voltage settings in the “standard” (i.e., of pre-load) set of protocols are 35, 50, 65 and 80 kV, with a number of projections for the FS mode ranging from 400 to 2000 depending on the reconstruction voxel size. Five nominal voxel sizes are available: 60, 80, 120, 160 and 240 μm. The rotation range is [-180°; +180°] for a FS protocol, and [-110°; +110°] for a SS protocol. The total scan time varies from 16 s to 560 s for the FS protocols, and 7.3 s for the SS ones. Typical reconstruction times ranges from 20 sfor low resolution scan to 2-10 minutes for the medium and high resolution protocols.

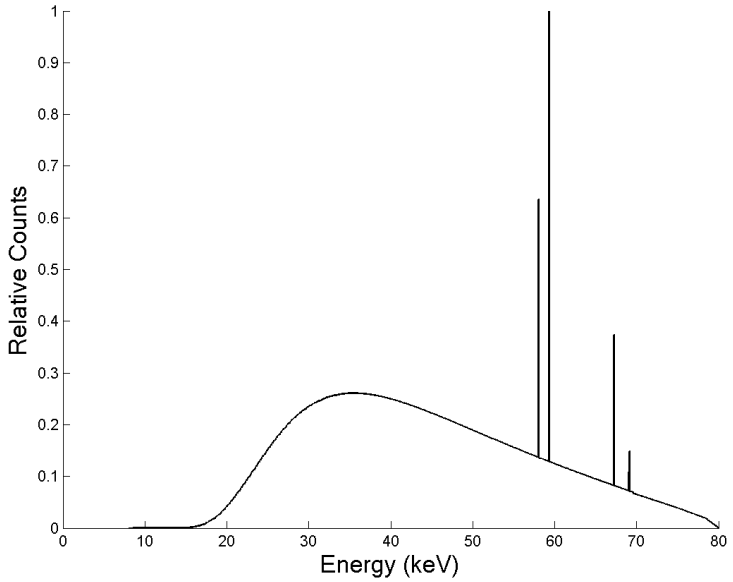

Figure 2.2: Spectral distribution simulated by *SpekCalc Windows release 1.1* of the IRIS scanner source at 80 kVp.

2.2.1 X-ray source

The x-ray source is a microfocus x-ray monoblock made up of a x-ray tube, an electronic control and analog interface circuitry, and an optional digital interface. This tube, with fixed tungsten anode and a nominal maximum focal spot size of 50 μm, can operate at 35-80 kVp and the cathode current ranges from 10 to 1000 mA. It is enclosed in a glass envelope, and a exit window made of polyetherimide, also known with the commercial name of Ultem of 2.5 mm in thickness, covers the aperture [24]. Moreover 2 mm of alluminium have been added in order to remove low energy photons that contributes only on the dose rate. These parameters are very important to know for the purpose of modeling the x-ray spectrum, as needed in numerical simulations (see Chapter 5). The lower energy photons are absorbed by the filter more efficiently than the higher-energy ones and, as a consequence, the mean energy of the beam is increased. Figure 2.2 shows a 80 kV-spectrum "similar" to that produced by this source. This spectrum has been simulated by the software *SpekCalc Windows release 1.1* taking into account the attenuation that the beam suffers because of the materials that it traverses [25].

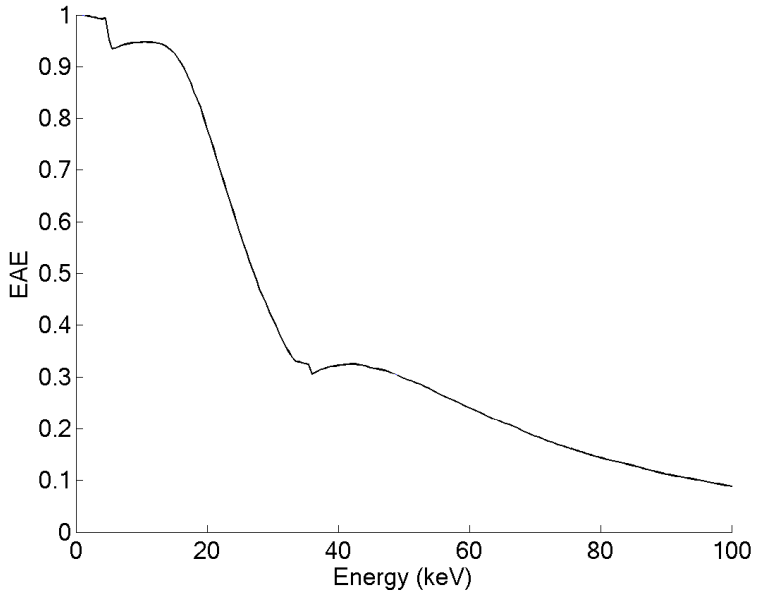

Figure 2.3: The Energy Absorption Efficiency is illustrated as a function of the energy for a 150 μm thick CsI scintillator. The linear attenuation coefficient and the absorption coefficient of the scintillator were provided by the software *XMuDat*.

2.2.2 X-ray detector

The x-ray detector consists in a flat-panel CMOS detector coupled to a 150 μm thick (CsI:Tl) scintillator. It is subdivided in 1536×1944 square pixels (transaxial×longitudinal) with side length ot 75 μm, resulting in a total active area of 115×145 mm^2. The minimum exposure time per frame in sequence mode is 39 ms, which can be shortened to 15 ms and 12 ms using 2×2 and 4×4 hardware rebinning, respectively. In Figure 2.3 is reported the EAE as a function of energy for the CsI scintillator of the IRIS scanner. The linear attenuation and the absorption coefficient of the scintillator were provided by the software *XMuDat* [26].

2.2.3 IRIS CT scanner geometry

Both the PET ring and the CT components (x-ray source and detector) are placed on the same rotating gantry having a total rotation range in the interval of [-190°; +190°]. The longitudinal offset between the centers of the PET and CT FOV is 120 mm. The nominal value of the Source to Axis Distance (SAD) and the Source to Detector Distance (SDD) are 206 mm and 262 mm, respectively, resulting in a transaxial FOV diameter of 90 mm. Due to the cone beam geometry, the longitu-

dinal FOV length for single rotation scans depends on the distance $r = \sqrt{x^2 + y^2}$ from the Axis of Rotation (AOR) (= z axis) and ranges from 90 mm at $r = 45$ mm (only available without cropping) to 110 mm along the AOR. The maximum scan lenght, allowing to multi-bed acquisition is 250 mm. With a detector pitch Δu of 75 µm and a magnification (M = SDD/SAD) of 1.27, the nominal voxel size Δx is $\Delta x = \Delta$u/M = 60 µm. Larger voxels can be obtained by rebinning the projection data.

Chapter 3

Contrast agents for vascular imaging

Introduction

X-ray based micro-CT is an important modality for non invasive small animal imaging. One of the major challenges using in vivo micro-CT for molecular imaging is to overcome its poor contrast sensitivity: exogenous, radio-opaque CAs are therefore required in order to increase image contrast.
Lots of studies in the literature are focused on their applications for in vivo imaging, evaluating especially their toxicity, their contrast enhancement properties, tissue permeability and their vascular residence time. Moreover, advances in nanotechnology have enabled the development of multifunctional nanoprobes that can simultaneously perform various functions, including molecularly targeted imaging and therapy. These progresses reflect the efforts to develop more specific, individualized therapies for various diseases, and to combine diagnostic and therapeutic capabilities into a single agent, bringing the imaging domain research and that of the therapeutic one closer. In this chapter an exhaustive description of the CAs for micro-CT imaging already available on the market will be presented, in addition to a brief overview of the potential applications of these emerging multifunctional nanoparticles in clinics.

3.1 Water-soluble agents and blood-pool agents

Depending on their formulation, contrast media can be distinguished between *water-soluble* agents, tipically used in clinics, and *blood-pool* agents for preclinical imaging.
The small molecular weights of the first ones, consisting of iodinated compounds,

results in passive diffusion through the endothelium of capillaries. They do not permeate cells, but distribute themselves in the extra-cellular fluid space, both intra and extra-vascular. They are excreted exclusively by rapid renal filtration in the glomerular capillaries, leading to rapid clearance rates but also to renal toxicity. Short imaging times are therefore necessary in order to keep up with the fast kinetics of these CAs. However most commercial micro-CT systems require several minutes to acquire projection data, so they are not able to acquire a sufficient number of projection images during the first pass of the CA. To overcome these limitations, CAs have been developed with the aim of keeping long vascular residence times and stable concentrations in blood after a single bolus injection. Such contrast media are usually referred to as blood-pool CAs. Due to their large molecular sizes, these agents cannot be filtered through the renal system as water-based solutions. Instead, they are slowly excreted via the hepatobiliary system. This class of CAs include nanoparticulated CAs that employ metal NPs, and liposomal CAs in which the contrast medium is embedded in a lipidic formulation.

3.1.1 Iodinated contrast agents

Clinical CAs are mostly based on iodinated molecules since, among nonmetal atoms, iodine, with an atomic number (Z) of 53, has a high x-ray attenuation coefficient. Figure 3.1 shows the total linear mass attenuation coefficients of iodine and water as a function of the energy. How it can be noticed, iodine linear attenuation coefficient is greater than that one of the water over the entire energy spectrum allowing to differentiate iodine from body tissues, which would not be differentiated from each other because of their similar linear attenuation coefficient[1]. Iodinated CAs have been used in clinical radiology for decades.
They are based on the tri-iodinated benzene ring, either in an ionic or non-ionic form. Compounds consist of either one tri-iodinated benzene ring (i.e., monomers) or two tri-iodinated benzene rings linked by an organic functional group (i.e., dimers). In addition, ionic tendency is governed by the presence or absence of a carboxylate (-COO-) functional group contained on an organic side chain. Hence iodinated CAs can be classified in ionic monomer, ionic dimer, non-ionic monomer and non-ionic dimer. Logically, these four groups have different properties, clinical uses, and toxicity profiles, and to some degrees these differences influence which types of agents are used [27].
An ionic dimer form was introduced in 1954 and is known under the commercial name of Hypaque (GE Healthcare, Princeton, USA). However, the high extracel-

[1]Total linear attenuation of soft tissues shows a similar trend to that of water, that is why in Figure 3.1 water is used for comparison.

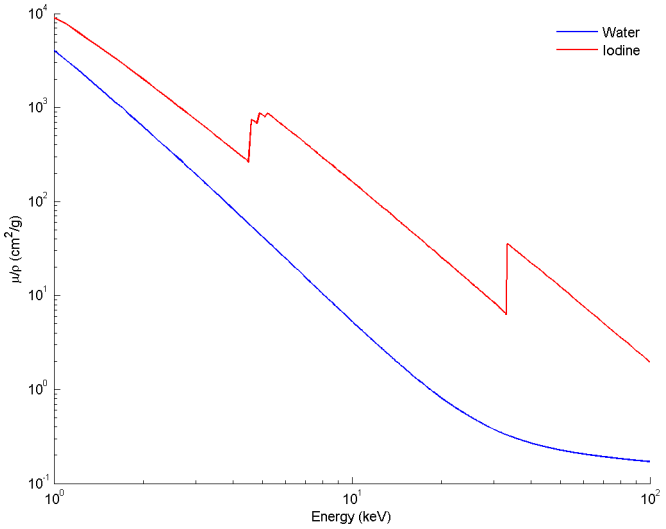

Figure 3.1: Total linear mass attenuation coefficients in cm^2/g of water, in blue, and of iodine, in red, as a function of photon energies in keV. In the energy range reported, it can be noticed the K edge at 33 keV and the series of L edges at 4.56, 4.85, and 5.19 keV of iodine. Attenuation coefficients were provided by the software *XMuDat* [26].

lular distribution volumes of this ionic compound were later found to be responsable for adverse reactions and chemotoxicity. Since the 1970s, several attempts have been made to reduce the toxicity of radio-opaque materials. For this purpose, a number of non-ionic forms was developed, such as iohexol (Omnipaque, GE Healthcare, Princeton, USA), iodixanol (Visipaque, Accupaque, GE Healthcare, Princeton, USA), iopamidol (Isovue, Bracco, Milan, Italy), iomeprol (Iomeron, Bracco, Milan, Italy). They are nowadays widely used in clinical angiographic examinations.

3.1.2 Nanoparticulated contrast agents

Nanoparticle-based CAs have paved the way for molecular CT imaging, as already explained. Metal-based agents are really interesting since they intrinsically provide higher attenuation than iodine, and can therefore be injected in smaller amounts. Moreover, as blood-pool agents, allow contrast enhancement studies over time after a single injection resulting in a less amount of toxic effects on the patients. Their physical and chemical properties strongly depend on their size and shape [28]. The average diameter of most of the metal inorganic nanoparticles proposed for in vivo imaging is over 20 nm. Generally the excretion of objects above 10 nm occurs through liver and spleen but when it has to do with intact metal

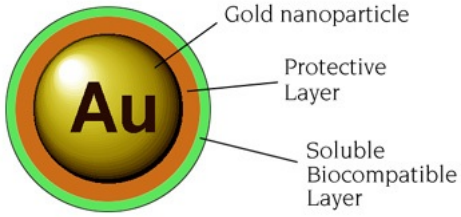

Figure 3.2: Shematic view of the core-shell nanostructure composition. More specifically it is a representation of a gold nanoparticle available on the market under the name of Auro Vist^{TM}, as will be further explained in the text. The image is adapted from http://www.nanoprobes.com/newsletters/ImgGold.html.

nanoparticles, the excretion is an extremely slow and inefficient process, leading to unwanted accumulation which in turn causes increased toxicity. On the other hand, nanoparticles with a diameter of a few nanometers would show ideally-fast clearance kinetics through renal excretion, as iodinated based CAs [29]. Consequently to what explained so far, the degradation kinetics of these nanostructures in physiological media, is an aspect that must be taken into account. Metal based CAs are usually in the form of core-shell nanostructures, since metal nanoparticles (representing the core of the final structure) are embedded in composite nanomaterials that act as an outer shell in order both to prevent the direct contact of metal with blood and to make the whole nanostructure biocompatible. Shell materials can be classified into two main classes: organics and inorganics. The organic materials are related to carbon based materials (mostly polymers), whereas the inorganic class includes metal, metalloid and metal salt nanoparticles. Silica materials, for example, falls into this group. In fact, it is generally regarded as a safe material, and has been previously used as surgical implant. It is well documented and accurate size and morphology control are achievable in the synthesis of silica nanoparticles. They are widely used to encapsulate interesting nanoprobes, also of different kinds and functionalities, simultaneously [28]. In Figure 3.2 is reported a schematic representation of these core-shell nanostructure. A contrast agent based on Gold Nanoparticles (GNPs), has shown great potential in imaging the vascular compartment. In fact, gold (Z=79) provides a strong x-ray attenuation, as was first demonstrated, inadvertently, by Wilhelm Roentgen, in the first x-ray human image. Synthesis of GNPs has been well established, and are available in the forms of spheres, cubes, rods, cages and wires by now. Morphology control is important as it greatly influences the physical properties of the products and in turn affects their role as imaging probes. A GNp-based CA is already commercially available under the name of Auro Vist^{TM} (15 nm and 1.9 nm) (Nanoprobes, Yaphank, USA) and it has been demonstrated that are particularly useful for in vivo vascular casting, studies of tumors, stroke, atherosclerosis and other vascular conditions.

However it has not already approved for human use. Uptake and biocompatibility of several GNPs are in fact controversial. Some studies claim their non-toxicity, but some other see their toxic potential to depend on their size, surface chemistry, and shape [30, 31]. Anyway, their longer blood residence time than iodine agents, approximately 15 hours blood half-life, make them really interesting for dynamic micro-CT studies.
Another innovative agent is a barium-based agent, commercially available as ExiTron^{TM} nano, and specifically formulated for preclinical CT imaging [32]. Two different formulations are on the market, depending on the concentrated formulation: ExiTron nano 6000, optimized for liver/spleen imaging, and ExiTron nano 12000, optimized for angiography.
Bismuth-based NPs in the form of Bi_2S_3 nanostructures hold great promise for CT contrast agents because bismuth possesses a high x-ray attenuation coefficient and it is less expensive than other elements. Moreover, Bi_2S_3 has low toxicity and leaves no residue in the organism [33]. It has been demonstrated that these nanoparticles can be used for in vivo imaging of the vasculatures and Reticuloendothelial System (RES)-rich organs after intravenous injection. When they were administered subcutaneously, regional lymph nodes were clearly revealed by CT. Recently, large-scale synthesis of Bi_2S_3 nanodots of 2 to 3 nm in diameter was reported. The high biocompatibility of the nanodots was confirmed by histological observation. In Figure 3.3 are reported the total linear mass attenuation coefficients of the previously mentioned metals. It must nevertheless be underlined the fact that the total attenuation of the CA also depends on its concentration in solution. Typical concentrations in water (or physiologically-compatible media) of CAs are in the order of less than 1 mg/mL to few hundreds of mg/mL.

3.1.3 Liposomal contrast agents

Liposomes are self-closed spherical or elliptical lipid vescicles composed of one or more lipid bilayers, which entrap an aqueous phase (an its representation is reported in Figure 3.4). Generally they can be loaded with various polar or non-polar substances which can be entrapped in the aqueous liposome interior, dissolved in the hydrophobic bilayer, or adsorbed on the liposome surface. Liposomes are very flexible carriers because various compositions of phospholipids can be used for their preparation, and their surface can be readily modified with various molecules such as Polyethylene Glycol (PEG), radioisotopes, antibodies, and metal chelates.
Although clinical contrast agents are used to prepare liposomal CT contrast agents, the pharmacokinetics and toxicity of the iodine compounds incorporated in the liposomes are different from those of free iodinated CAs. In fact the encapsulation alters the usual renal clearance mechanism of the iodinated agent, resulting in a ex-

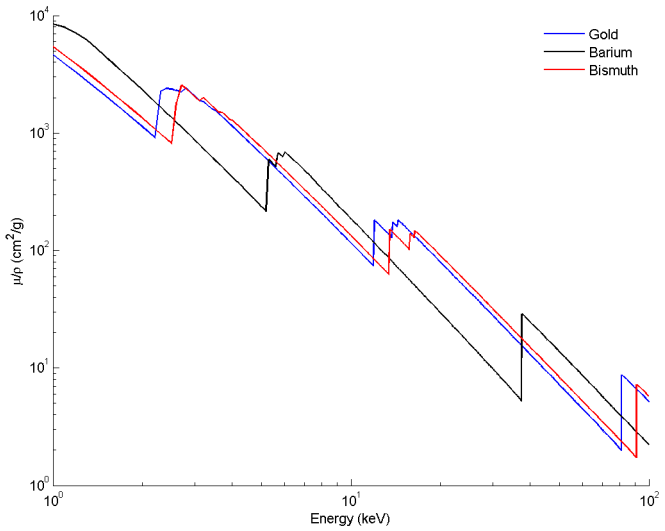

Figure 3.3: Total linear mass attenuation coefficients in cm^2/g of gold in blue, barium in black, and bismuth in red as a function of energy in keV. K edges at 80, 37 and 90 keV, respectively, can be noticed besides the series of the corresponding L edges. Attenuation coefficients were provided by the software *XMuDat* [26].

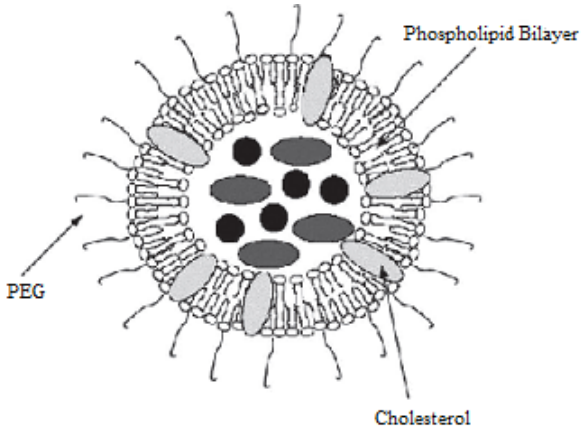

Figure 3.4: Schematic diagram of a liposome. Image is adapted from [34].

cretion via the RES that is slower. The first liposomal contrast agent for micro-CT imaging was introduced in 1998 and it consisted of an iodinated contrast medium embedded in a lipidic formulation. It was used mainly to detect solid tumors of the liver or spleen. Fenestra VC (ART Advanced Research Technologies Inc., Montreal, Canada), for example, is a commercial blood-pool agent consisting of iodinated triglycerides formulated in a stable, submicron oil-in-water lipid emulsion. It has been shown to reside in the vascular compartment for more than three hours, although it does not provide strong contrast due to its low iodine content (50 mg/mL).
Another commercially available blood-pool agent, is eXIA 160 (Binitio Biomedical Inc. Canada), an aqueous colloidal poly-disperse contrast agent containing a large concentration of iodine (160 mg/mL), which allows sufficient enhancement with very low injection volumes [35]. It does not only enhance the liver and spleen, as expected with clearance via RES, but it also enhances the myocardium and the brown adipose tissue.

3.2 Applications of contrast agents in micro-CT molecular imaging

Blood pool imaging is extremely important for the evaluation of the current state of blood flow and for the discovery of the blood flow irregularities caused by atherosclerotic lesions, thrombi or tumors. With the help of selective blood pool agents, blood perfusion and various cardiac parameters as well as a status of blood flow and vascular system in several organs, can be evaluated. Blood pool specific imaging agents can also provide minimally invasive angiography, oncologic imaging of angiogenesis and identifying hemorrhage. Most of the 4D micro-CT studies use in fact blood pool contrast agents allowing to measure cardiac function, but localization of metastases in different organs are also possible according to the specific organ perfusion properties of the medium employed. The liposomal CA eXIA 160 has been proposed for cardiac micro-CT, since it creates strong contrast between the blood and the tissue with a low injection volume of only 0.125 mL per 25 g mouse. Notably, this contrast agent was also taken up by the myocardium, allowing imaging myocardial infarction in mice and provided continued enhancement when it was eliminated from the blood [35]. Assessment of liver function and detection of metastases was also demonstrated using delayed contrast enhancement such as ExiTron nano. It was demomstrated that after a single injection with a volume of 100 µL per 25 g mouse of this nanoparticulated CA, contrast of liver and spleen peaked up after 4-8 hours, lasted up to several months and was tolerated well by mice, allowing longitudinal monitoring of pathological

processes of these organs in small animales [32].

The possibilities that are nowadays available thanks to the huge progresses of nanotechnology, can be gathered under the name of "*theranostics*" [28]. This term was introduced to indicate therapeutics guided by diagnostics: therapeutic functions can be in fact implemented on many nanomaterials which are already imaging agents, upgrading them to *theranostic agents*. These aims can be reached by targeting strategies which are really variable depending on the desired targets. In the case of cancer, for example, it is a common approach to identify a biomarker that is aberrantly expressed on the surface of cancer cells, and then to load its cognate binding vector onto probes-carriers to achieve recognition and tumor homing. For nanoplatforms, the unique size scale of the particles enables achievement of an Enhanced Permeability and Retention (EPR) effect in tumor targeting. However, care has to be taken with the particles surfaces to avoid innate immunosystem recognition and to secure sufficiently long circulation half lives for the agents to reach their targets. The first targeted gold nanoparticles that enable molecular CT imaging of cancer, date back to 2008 when R. Popovtzer et al. described a new class of immuno-targeted gold nanoprobes that selectively and sensitively target tumor specific antigens. They were able to demonstrate that these gold nanoprobes formed a concentrated assembly on the cancer cells, yielding a distinguishable x-ray attenuation, which was not typical for nondecorated cells or tissue. This transformed the targeted cancer into highly distinct and easy to diagnose features [36]. Nanoparticle-based theranostics are still in their early stages of development, but different studies are already available in literature. Micelles, for example, may be used as targeted drug carriers. Three principal targeting mechanisms can be seen for micelles, as well as for any other pharmaceutical long-circulating drug carrier. The first one is based on micelle spontaneous penetration into the interstitium through the leaky vasculature (EPR effect) and is considered as a "passive targeting". The transport efficacy and accumulation of microparticulates in the tumor interstitium is to a great extent determined by their ability to penetrate the leaky tumor vascular endothelium. Moreover, it has been demonstrated that diffusion and accumulation parameters are strongly dependent on the cutoff size of tumor blood vessel wall, and the cutoff size varies for different tumors. The second targeting mechanism is based on the fact that many pathological processes in various tissues and organs are accompanied with local temperature increase and/or acidosis, and micelles made of thermo or pH sensitive components. At last, specific ligands, such as antibodies, can be attached to the water-exposed termini of hydrophilic blocks [37].

Finally, the introduction of multiple probes that incorporate different high-Z materials allow co-localization studies and many other applications. Dual energy micro-CT, for example, falls in this field, offering a solution to the problem of separeting different materials. It essentially utilizes the x-ray attenuation informa-

tion from two different beam energy levels to characterize chemical composition.

Chapter 4

Performances of the IRIS CT scanner

Introduction

In this chapter the performances of the IRIS CT scanner are evaluated. In the first part of the chapter, we mainly focus on the theory concerning with the physical parameters by which the performances of the imaging system are evaluated. In the second part, results are presented. More specifically the noise structure of the CMOS flat panel perfomances have been evaluated in terms of NPS. The spatial resolution of the IRIS CT scanner has been analyzed in terms of MTF. Noise of reconstructed images has been evaulated in the frequency domain by means of NPS, and in the spatial domain in terms of the standard deviation as a function of the dose and the voxel size. Then we focus on phantom studies employing conventional CAs based on iodine. They have allowed the first investigations of the IRIS CT scanner high temporal resolution protocol, specifically designed for dynamic (functional) imaging. Finally results of CT numbers calibration are reported. As a new achievement of this work, the BH artifact is analyzed and a first correction of it is provided.

4.1 Materials and methods

Image data analysis was performed by using first the software *ImageJ* to display and process reconstructed images and *MATLAB R2014a* in order to get a final statistic analysis of image data.

4.1.1 Evaluation of the detector performances

Since performance of the imaging detector is largely responsible for the quality of reconstructed images, proper selection and optimal design-configuration of the detector system are essential for successful microtomography [38]. Fourier-based analyses of those quantities generally assumes that the system must has a Linear Shift Invariant (LSI) response to an input signal, and noise must results from wide-sense-stationary random processes. Due to the non-uniformity of gain among the various pixels of the device, x-ray detector results a LSI system only after the gain correction.
Detector noise can be random and systematic depending on its technology. A common systematic source of noise is the structure (or fixed pattern) noise. This type of noise is correlated because its pattern remains the same in repeated images taken with the same detector. Structure noise needs to be removed in order to improve the SNR of the x-ray detector. This process, known as flat-field correction, is applied either by normalizing with the flat-field image or by subtraction of the flat-field image [39, 40].
Noise is usually described mathematically in the spatial domain by the standard deviation, σ (or the variance, σ^2), in measurements of the image signal over a specified Region of Interest (ROI) of a homogeneous (flat) area. However the variance cannot describe adequately the noise of a x-ray detector and, in general, of an x-ray imaging system because it does not show the spatial correlation of noise. Therefore, the noise transfer properties of the detector are better evaluated in terms of the Noise Power Spectrum (NPS). It is essentially the spectral decomposition of the variance (σ^2) and it provides an estimate of the spatial frequency dependence of the point-to-point fluctuation in the image. The measurement of the NPS is conceptually straightforward but difficult to carry out experimentally, and there has not been universal agreement on the best methods for its measurement. The NPS is most commonly computed directly from the squared Fourier amplitude of 2D image data

$$\mathrm{NPS}(u_n, v_k) = \lim_{N_x, N_y, M \to \infty} \frac{\Delta x \Delta y}{M N_x N_y} \sum_{m=1}^{M} \left| \sum_{i=1}^{N_x} \sum_{j=1}^{N_y} [I(x_i, y_j) - \bar{I}]\, \mathrm{e}^{-2\pi \mathrm{i}(u_n x_i + v_k y_j)} \right|^2 \tag{4.1}$$

where $I(x_i, y_j)$ is the image intensity at the pixel location (x_i, y_j), $\bar{I}$ is the global mean intensity, and u and v are the spatial frequencies conjugated to x and y, N_x and N_y are the number of pixel in the x and y directions of the digital image, Δx and Δy are the pixel spacing in the x and y directions and M is the number of region used for the analysis in the ensemble average [41]. For a correlation with the dose, the Normalized Noise Power Spectrum (NNPS) would be more advisable to calculate. It can be extracted from the measure of NPS as follows

[42]:

$$\mathrm{NNPS} = \frac{\mathrm{NPS}}{(\mathrm{G}\cdot X)^2} \tag{4.2}$$

where X is the air kerma in μGy unit, and G is the gain factor in digital units per μGy. The gray (symbol: Gy) is a derived unit of ionizing radiation dose in the International System of Units (SI). One gray is the absorption of one joule of energy, in the form of ionizing radiation, per kilogram of matter [43]:

$$1Gy = 1\frac{J}{kg} = 1\frac{m^2}{s^2} \quad . \tag{4.3}$$

4.1.2 Evaluation of tomographic imaging performances

Tomographic imaging perfomances are usually evaluated in terms of spatial resolution, noise, contrast and dose efficiency. These parameters are related factors and affect each other in complex ways. The purpose of this section is just giving a thorough description of these fundamental aspects of any imaging system, by which IRIS performances will be analyzed.

Spatial resolution

The MTF expresses the ability of an imaging system to reproduce the contrast in the image at various spatial frequencies f and is generally used to evaluate the spatial resolution. It essentially indicates how the spatial frequencies that compose the object are transferred to the output image. If the detector had a perfect resolution, MTF would have the costant value of 1.0 in the entire range of the frequencies. However, higher spatial frequencies are affected by blurring and unsharpness, so that a decreasing trend of MTF as f increases is generally noticed. For this reason, the frequency that corresponds to MTF value of 10 % is commonly used to express the limiting resolution of the system. At first order, the MTF of the tomographic system of a given geometry can be evaluated using its dependence on three factors, namely, the penumbra effect (explained in section 2.2.1), the spatial resolution of the detector array, and the reconstruction algorithm:

$$\mathrm{MTF}_{\mathrm{tot}}(f) = \mathrm{MTF}_{\mathrm{foc}}(f)\cdot \mathrm{MTF}_{\mathrm{det}}(f)\cdot \mathrm{MTF}_{\mathrm{alg}}(f). \tag{4.4}$$

Besides, for a LSI, the spatial resolution is completely defined in terms of the Point Spread Function (PSF), passing from the frequency domain to the spatial one. PSF essentially represents the response of the imaging system to an impulse that, can be mathematically represented by a Dirac delta function. Due to both the physical performance of all real imaging systems, the focal spot size, and the finite sampling pitch in the case of digital ones, PSF is always a larger distribution

than a sharp point-like impulse. As a consequence, larger shape of PSF, will result in worse spatial resolution. For this reason, the parameter that quantitatively describes the spatial resolution of an imaging system in the spatial domain, is the Full Width at Half Maximum (FWHM) of the PSF itself.
Returning to the three blurring components of equation 4.4, they can be modeled with good approximation with gaussian functions with widths equal to σ_{foc}, σ_{det}, and σ_{alg}, respectively. In the spatial domain, equation 4.4 take therefore the form of the following:

$$\sigma_{\text{PSF}} = \sqrt{\left[\left(1 - \frac{1}{\text{M}}\right)\sigma_{\text{foc}}\right]^2 + \left(\frac{1}{\text{M}}\sigma_{\text{det}}\right)^2 + \left(\frac{1}{\text{M}}\sigma_{\text{alg}}\right)^2} \tag{4.5}$$

where the dependence on the magnification M has included. Here σ_{PSF} represents the width of the in plane PSF of the imaging system, σ_{foc} the focal spot size, σ_{det} the detector Line Spread Function (LSF) on the detection plane, while σ_{alg} can be estimated considering that the backprojection involves linear interpolation of filtered data, which is equivalent to a convolution with a triangle function with FWHM equal to the detector sampling pitch Δu. If the standard ramp filter is used, the linear interpolation is the only source of blurring attributable to the reconstruction algorithm.
From equation 4.5 it follows that the intrinsic spatial resolution of the detector is progressively less important for increasing values of the magnification. In fact, for $\text{M} \gg 1$, the object is more and more close to the x-ray focal spot, the size of which will dominate the overall image unsharpness. On the other hand, for $\text{M} \simeq 1$, the object is nearly in contact with the detector so that the penumbra effect almost vanishes. In this case, only the combined contribution of the detector resolution and of the reconstruction algorithm influences the overall spatial resolution.

Noise of CT images

Image noise is the uncertainty introduced by an imaging system due to stochastic or systematic fluctuations of the image values at each point. It may arise either from the inherent statistical nature of photon detection (quantum noise) or from electronic noise due to thermal processes. The variance in the linear reconstructed attenuation coefficient can be modeled as follows [16]:

$$\sigma_{\mu}^2 = \frac{\pi^2}{12\Delta x^2 n_{\text{ang}} N} + \sigma_{\text{sym}}^2 \tag{4.6}$$

where N is the number of photons per projected ray sum, n_{ang} is the number of projection views used to form an image, Δx is the isotropic voxel spacing in

the image, and σ^2_{sym} represents the variance introduced by all sources of photon-independent noise. Although equation (4.6) is developed under the assumption of parallel ray acquisition, the resulting variance estimate has been shown to be a reliable estimate of performance with fan and cone beam acquisition geometries. It is really clear now the relationship between noise, x-ray dose and isotropic resolution. Generally noise is analyzed in terms of the coefficient of variation (C_v) which is a measure of the relative standard deviation and is defined as the ratio of the standard deviation σ to the mean μ:

$$C_v = \frac{\sigma}{\mu}. \tag{4.7}$$

It gives informations about the contrast resolution of the image, or in other words, it is a measure of the ability to distinguish substances with similar attenuation coefficients. For an ideal, quantum-noise limited CT scanner, the coefficient of variation calculation resulting from equation (4.6) can be approximated by

$$\frac{\sigma}{\mu} \propto \frac{1}{\Delta x^2 \sqrt{D}} \tag{4.8}$$

which exhibits an inverse relationship between the coefficient of variation and the square of the isotropic voxel size, and the square root of the x-ray entrance dose, D. For a constant C_v, a tenfold increase in dose will allow a reduction in the isotropic voxel size by a factor of only $10^{1/4}$. Alternatively, an improvement in resolution, achieved by decreasing voxel size by a factor of 10, will result in an equivalent image quality if the x-ray dose to the animal is increased by a factor of 10^4. It is really clearly now how micro-CT in vivo imaging brings forth an important challenge since it would obtain high quality images with an x-ray dose small enough for the animal to recover. The limit to the amount of radiation that can be used for live animal imaging is given as the lethal dose, or LD50/30. It is the whole-body radiation dose that would kill 50 % of an exposed population within 30 days of exposure. For a mouse, the lethal dose ranges from 5.0 to 7.6 Gy, depending on the strain of mouse, age at exposure and many other factors. One of the aims of this thesis is in fact to examine the fundamental limits of the voxel-to-voxel variation as a function of isotropic resolution and dose to the animal [16].

Contrast to Noise Ratio

The coefficient of variation is a measure of the absolute noise in the image, for this reason most used parameter is the CNR. To achieve images of a similar quality to those produced by a clinical scanner, the image contrast must be improved to compensate for higher absolute noise in the micro-CT images. Micro-CT offers an inherently higher contrast than clinical scanners because lower energy x-ray

spectra are used. A lower spectral energy will in fact provide a higher contrast image, but there will be fewer photons reaching the detector to form the image, mainly due to the very low power of x-ray sources employed in micro-CT with as compared to their clinical counterparts. Moreover, the sensitive area of each detector pixel in micro-CT systems can be up to hundreds times smaller than those of clinical CT detectors. Therefore the micro-CT system will produce images with more quantum noise than a clinical CT scanner. Also the electronic noise is higher in flat-panel x-ray detector with respect to standard clinical-level CT detectors. A second method of increasing contrast is through the use of exogenous contrast agents.

Albert Rose was the first person who tried to theoretically relate levels of contrast, resolution, and noise based on a probabilistic model. It can be used in x-ray imaging detectors to show the relationship between the number of input x-ray quanta and the perception of detail. In this case, the signal to noise ratio of this model (SNR_{Rose}) describes the detectability of a uniform object of area A in a uniform background having a mean N_b number of quanta per unit area [44]. The SNR_{Rose} is given by:

$$SNR_{Rose} = k = \frac{A(N_b - N_0)}{\sqrt{AN_b}} = C\sqrt{AN_b} \tag{4.9}$$

where N_0 is the average number of x-ray quanta per unit area in a uniform object of area A. The noise is the standard deviation $\sigma_b = \sqrt{N_b}$, where N_b is the number of x-ray quanta in an equal area (compared to the object) of a uniform background. It may be observed that the Rose model calculates the noise of the background instead of that of the object because it assumes that the signal difference between the object and the background is very small compared with the signal of the background. This is true only in the case of low-contrast signals. Furthermore, the Rose model is valid only for uncorrelated Poisson distributed noise (because it assumes that the standard deviation equals the square root of the signal). However, in most x-ray imaging systems the noise is neither perfectly uncorrelated nor Poisson distributed. Rose showed that the SNR_{Rose} needs to be approximately five or more in order for the human observers to detect reliably an object under specific conditions. This limit depends on the detection threshold by the observers during the period of the experiment and it can be used to estimate the contrast threshold C_T:

$$C_T = \frac{k}{\sqrt{AN_b}}. \tag{4.10}$$

CNR shows therefore the relationship between contrast and noise in an image for large-scale objects [4]. It is usually calculated as:

$$CNR = \frac{|I_o - I_b|}{\frac{1}{2}(\sigma_o + \sigma_b)} \tag{4.11}$$

where the numerator expresses the absolute contrast in terms of intensity difference between an object of interest and its background, and the denominator is the image noise expressed in terms of the standard deviation of the combined object-background[1]. For a linear (or linearizable) and quantum-limited x-ray detector, it has been demonstrated that CNR equals $\mathrm{SNR}_{\mathrm{Rose}}$ [45]:

$$\mathrm{SNR}_{\mathrm{Rose}} = \mathrm{C}\sqrt{\mathrm{AN_b}} = \mathrm{C}\frac{\mathrm{AN_b}}{\sqrt{\mathrm{AN_b}}} = \mathrm{C}\frac{I_\mathrm{b}}{\sigma_\mathrm{b}} = \frac{|I_\mathrm{o} - I_\mathrm{b}|}{I_\mathrm{b}} \cdot \frac{I_\mathrm{b}}{\sigma_\mathrm{b}} = \mathrm{CNR}. \tag{4.12}$$

4.1.3 Dosimetry

Dosimetric measurements are essential in order to monitor the radiation dose that is delivered on the small animal, since some limitation applies, as explained before. The Computed Tomography Dose Index (CTDI) was introduced to quantify the radiation output from x-ray CT examination of multiple contiguous CT scans. It sought to create an "index" to reflect the average dose to a cylindrical phantom in the central region of a series of scans. The word "index" was in fact specifically included in CTDI name to distinguish the quantity from the radiation dose absorbed by a patient. The CTDI technique uses a long ionization chamber to integrate the primary and scattered radiation delivered with a one gantry rotation and normalizes it to the nominal beam width. The CTDI is a standardized measure of the radiation output of a CT system, measured in a cylindrical acrylic phantom, that enables users to estimate the amount of emitted radiation and compare the radiation output between different scan protocols or scanners. Further calculations are required to map scanner output to patient dose, taking into account the patient size, irradiated organs, body composition, and scan range. It provides a very useful way to compare the doses delivered by various scan protocols or to achieve a specific level of image quality for a specific size patient. Anyway it is important to underline that CTDI cannot be used as a surrogate for patient dose [46]. Generally it is measured over a length of 100 mm, thus it is defined as:

$$\mathrm{CTDI}_{100} = \frac{1}{\mathrm{NT}} \int_{-50\,\mathrm{mm}}^{50\,\mathrm{mm}} \mathrm{D}(z)\,\mathrm{d}z \tag{4.13}$$

where NT is the nominal beam aperture along the z axis and $\mathrm{D}(z)$ is the measured dose profile. The $\mathrm{CTDI}_{100,\mathrm{air}}$ is a good approximation of the dose D(0) free in air at the isocenter [23]. In this work we employed the $\mathrm{CTDI}_{100,\mathrm{air}}$ values that were measured in a previous work [23]. They are reported in Table 4.1 for all tube voltages. From these measurements it is possible to calculate the mean dose

[1]The noise in the CNR definition can be expressed either as the background noise or as the combined object-background noise. Both definitions are very close in the case of low-contrast objects.

Tube voltage (kV)	$CTDI_{100,air}$ (mGy/mAs)	$\sigma CTDI_{100,air}$ (mGy/mAs)
35	0.17	0.03
50	0.60	0.05
65	1.14	0.08
80	1.78	0.12

Table 4.1: $CTDI_{100,air}$ values and relatives standard deviation $\sigma CTDI_{100,air}$ for all tube voltages. $CTDI_{100,air}$ values were measured in a previous work [23].

Tube voltage (kV)	Dose to mice (mGy)	Dose to rats (mGy)
35	17.8	12.8
50	51.6	42.0
65	7.2	31.8
80	33.6	29.5

Table 4.2: Mean dose in mGy delivered to mice and rats (diameters of 20 and 40 mm respectively) for the P160-AllkV-FS scanning protocol. Mean dose values are calculated by means of $CTDI_{100,air}$ values reported in section 4.1.3, and Monte Carlo conversion factors adapted from [47].

to animals of standard diameters (20 mm for mice, 40 mm for rats) for all kind of protocol, by using Monte Carlo conversion factors from dose in air to mean animal dose [47].

4.1.4 Scanning Protocols

Different kind of scanning protocols were used during this thesis, but one of them was implemented several times, since it provides a good trade-off between dose and scan time [23]. It is the P160-AllkV-FS which consists in four CT acquisitions in FS mode at the standard tube voltages with a total exposure, which is optimized for each energy and corresponding to 147, 98, 35.1 and 19.6 mAs, respectively. The number of projection views is set to 576 for all acquisitions, each of which is followed by the same preprocessing and reconstruction protocols. The reconstructed voxel size is 160 µm and the Ram-Lak filter is implemented. Once the scanning protocol is set, the mean dose values in mGy unit to mice and rats can be calculated as explained in section 4.1.3. The mean dose values corresponding to the P160-AllkV-FS protocol, are reported in Table 4.2 for all tube voltages.

4.2 Results

4.2.1 NPS of CMOS flat panel detector

The measure of the 2D NPS of the detector was perfomed by analyzing separately sixteen central non-overlapping regions of dimensions 64×64 of a flat field image, giving sixteen bidimensional realizations according to equation (4.1). The hardware rebinning was kept fixed to two for all measurements.
Applying the following formula a corrected flat field image $I_{corr}(x, y)$ was obtained:

$$\mathrm{I_{corr}}(x,y) = \frac{\mathrm{I}(x,y) - \overline{\mathrm{I_{dark}}}(x,y)}{\overline{\mathrm{I_{FF}}}(x,y) - \overline{\mathrm{I_{dark}}}(x,y)} \cdot \left(\overline{\overline{\mathrm{I_{FF}}}(x,y) - \overline{\mathrm{I_{dark}}}(x,y)}\right) \tag{4.14}$$

where $\overline{\mathrm{I_{FF}}}(x, y)$ is the average of ten flat field images at the same irradiation conditions and integration time, $\overline{\mathrm{I_{dark}}}(x, y)$ is the average of the ten dark images at the same integration time of flat field images. A zero padding with 320 samples was perfomed on the selected ROIs before Fourier transforming, in order to increase the sampling rate in the frequency domain and speed up processing time. For each ROI the Two-Dimensional Discrete Fourier Transform (DFT2D) of the signal fluctuation was therefore implemented; these realizations were then averaged and normalized according to pixel and ROI dimensions, obtaining a measure of the 2D-NPS in mm^2. For an easier analysis of noise as a function of the dose, a 1D representation of the 2D-NNPS was calculated as equation (4.2) states. The gain factor G was determined as the slope of the characteristic curve, relating the mean pixel value to the air kerma at the isocenter. Using the flat-field images at three exposure levels the gain factor was determined by linear regression to be $G = 154$ digital units per μGy. For the air kerma values, $\mathrm{CTDI_{100,air}}$ values in mGy/mAs units, reported in Table 4.1, were multiplied for mAs values obtaining the air kerma at the isocenter. For a 1D-NNPS representation, data from five rows and columns on both sides of the corresponding axis (for a total of ten), omitting the axis itself, were averaged, resulting in the Horizontal and Vertical 1D-NNPS (H-NNPS, V-NNPS) respectively. Axis were omitted because they are susceptible to any remnant column or row wise fixed pattern noise on the flat field image. In other words, in the presence of horizontal or vertical structure noise, the NPS has an unusually large value along the frequency axes which is not representative of stochastic noise [48]. Each data point was associated with a spatial frequency by means of the formula $f = \sqrt{u^2 + v^2}$, where u and v correspond to the spatial frequencies of the 2D-NPS. Smoothing was then obtained by averaging the data points within the rows and columns that fall in a frequency interval that ranges from the minimum to the Nyquist spatial frequency, with an interval equal to the sampling frequency after zeropadding.

Figure 4.1(a) illustrates H-NNPS and V-NNPS profiles, extracted from the 2D-NNPS measured from a corrected flat field image acquired at the tube settings of 80 kV, 1 mA and a time of exposure of 34 ms. As expected, noise has a structured appearance and it can been noticed that the two profiles present similar trends, so they can be averaged to calculate the mean 1D-NNPS. The Nyquist frequency is the maximum spatial frequency that has been plotted and it is equal to 3.33 mm^{-1} for a pixel rebinning of 2×2[2]. In Figure 4.1(b) are reported the 1D-NNPS calculated at the tube settings of 1 mA for the tube voltages of 35, 50, 65, and 80 kV to which correspond a time of exposure per frame of 255, 170, 61, and 34 ms, respectively. Thus the relatives air kerma values at the isocenter are: 42.46 μGy, 102.61 μGy, 69.86 μGy and 60.65 μGy, respectively. The dependence on the air kerma is really clearly even if noise values at 35 kV are lower than those at 80 and 65 kV. This fact can be ascribed to the poor photon statistics. NPS was therefore also evaluated as a function of the air kerma keeping fixed the tube voltage and changing mAs values in terms of tube current. More specifically, flat field images were acquired at 80 kV, with an exposure time of 34 ms and the tube current was set to 0.2 mA, 0.6 mA and 1 mA. Thus the corresponding air kerma values are 12.13, 36.39, and 60.65 μGy. Figure 4.1(c) illustrates the 1D-NNPS at these settings confirming what was before supposed.

4.2.2 Tomographic imaging performances

Spatial Resolution

The method used for evaluating the MTF of the imaging system consists substantially in a measure of a oversampled LSF which is obtained with a slightly angulated tungsten wire respect to the z axis (AOR) [49]. A 13 μm tungsten wire phantom was used for this measurement. It was positioned as much as possible at the center of the FOV, resulting in a radial distance of 1.5 mm from the AOR, and at a slight angle both to the x and y axis (3.8° and 7.3°, respectively). In Figure 4.2 a zoom of the transaxial slice of the wire phantom is reported. 2000 projections were acquired at 80 kV and reconstructed with the standard apodization window with the nominal voxel size. Because of the slight angulation of the wire, twenty slices were taken into account corresponding to twenty different alignments of the wire relative to the sampling coordinate. Thus twenty partial LSFs have been obtained in the range between the two different half-pixel-shifted alignments. More specifically an Horizontal Line Spread Function (H-LSF) and Vertical Line Spread Function (V-LSF) were obtained from each slice integrating a ROI of size 14×14 pixels in the region of the wire, in the columns direction

[2]The Nyquist frequency is defined as half the sampling frequency which in turn depends on the sampling pitch.

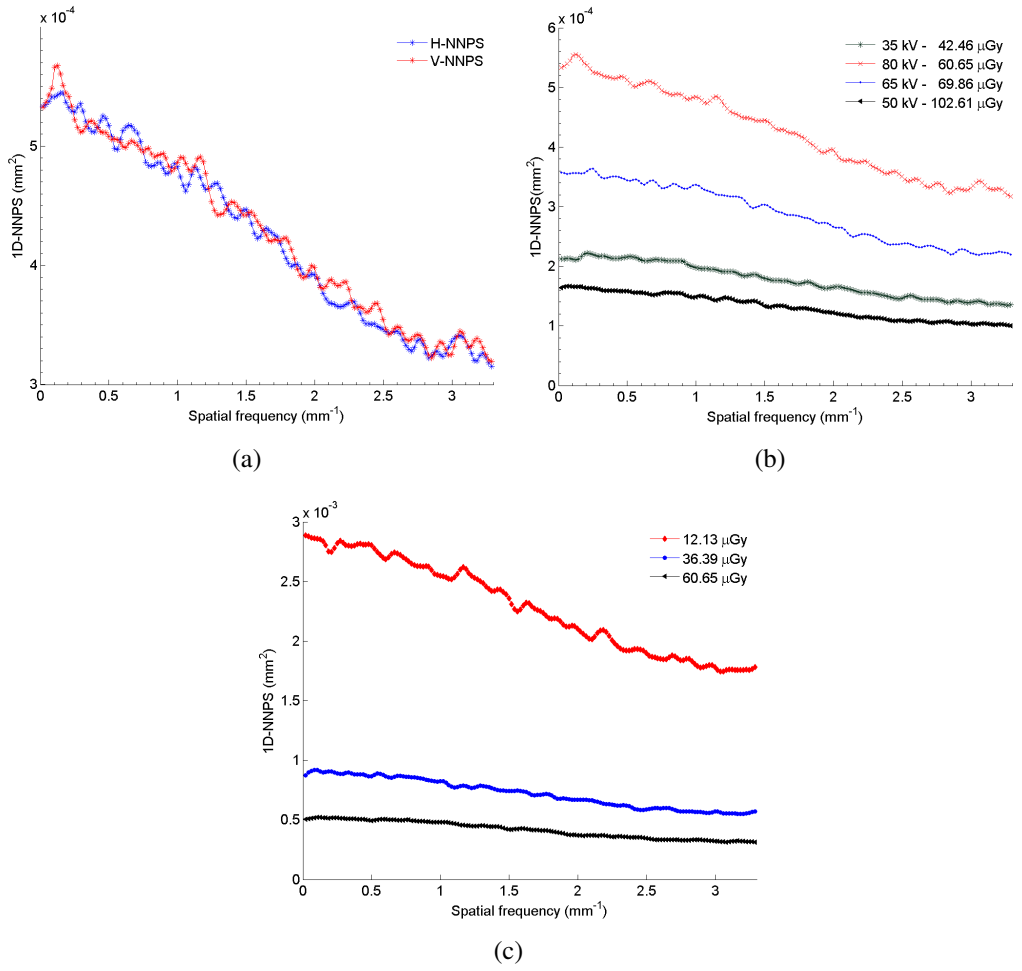

Figure 4.1: 4.1(a): Horizontal and vertical NNPS profiles (H-NNPS and V-NNPS respectively) of the CMOS flat panel, extracted from the 2D-NNPS of a flat field image acquired at 80 kV, 1 mA and an exposure time of 34 ms. 4.1(b): Average 1D-NNPS of the CMOS flat panel at the different tube voltages. The corresponding air kerma values at the isocenter have also been reported. 4.1(c): Average 1D-NNPS of the CMOS flat panel measured with flat field images acquired at 80 kV, with an exposure time of 34 ms and a tube current of 0.2 mA, 0.6 mA and 1 mA. The corresponding air kerma values at the isocenter are 12.13, 36.39, and 60.65 µGy.

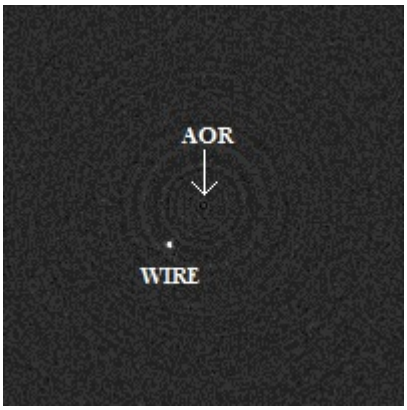

Figure 4.2: Transaxial slice with a reconstructed voxel size of 60 μm of the tungsten wire phantom used for the measurement of the presampling MTF. The distance between the AOR and the wire is 1.5 mm. The display window (min; max) is (−1500 HU; 1500 HU).

to get the H-LSF, and in the rows direction for the V-LSF. Consequently, each partial LSF consists of fourteen data bins with sampling step, $\Delta x = 58.8\ \mu$m. The center of mass along the x and y axis (CM_x and CM_y, respectively) for each ROI was computed by using *ImageJ* in order to shift each partial LSF according to its center of mass. Finally, a total of twenty profiles have been employed to generate a presampled LSF. Figures 4.3(a) and 4.3(b) show the presampled H-LSF and V-LSF measured in the axial plane, respectively. The resulting effective sampling distance was 3 μm and it is apparent from the figure that the LSF data were finely sampled. The oversampled H-LSF and V-LSF were then fitted with a gaussian function, resulting in a FWHM of (158 ± 4) μm for the H-LSF, and (185 ± 5) μm for the V-LSF. The difference between the two FWHMs can be attributed to expected differences between LSFs along radial and tangential directions. In case of proper geometrical calibration of the system, such differences must be negligible in proximity of the AOR when proper angular sampling is done (as in this case). Hence, the results obtained here seem suggesting that a geometrical re-calibration of the system should be necessary at the time of writing of this thesis. An average FWHM of (171 ± 6) μm was obtained.
As the MTF can be obtained by Fourier transforming the presampled LSF, in a gaussian approximation it will result in a gaussian function with aperture $\sigma_{\mathrm{MTF}} = 1/2\pi\sigma_{\mathrm{LSF}}$. Thus the frequency that corresponds to MTF value of 10 %, can be calculated as follows:

$$f_{10\,\%} = \frac{\sqrt{2\ln 10}}{2\pi\sigma_{\mathrm{LSF}}} \tag{4.15}$$

and then the relative low contrast detectability denoted by R_{10}, can be evaluated:

$$R_{10} = \frac{1}{2f_{10\,\%}} \approx 0.622 \cdot \mathrm{FWHM}. \tag{4.16}$$

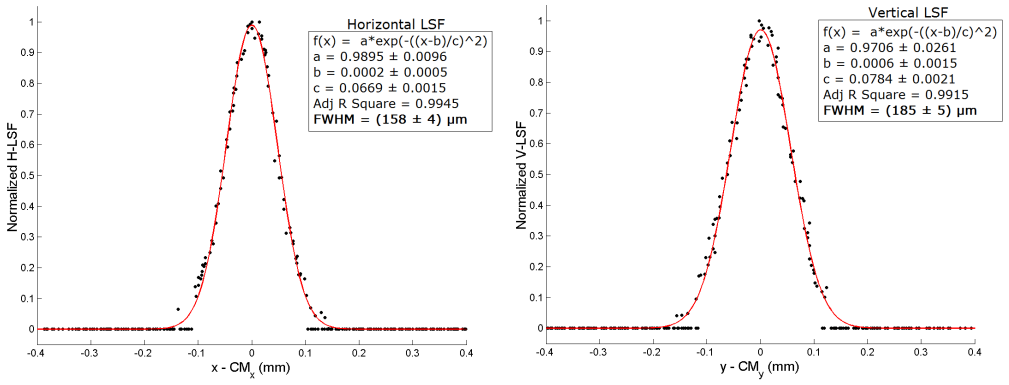

(a) (b)

Figure 4.3: The normalized finely sampled LSFs measured with the wire in the x (H-LSF in 4.3(a)) and y (V-LSF in 4.3(b)) direction, where the sampling distance was 60 µm. The Gaussian fit is also reported with a red line for both LSFs.

Thus the measured spatial resolution in the axial direction is 4.7 line pairs per mm (lp/mm) at 10 % MTF, resulting in a low contrast detectability R_{10} of (105 ± 3) µm.

For comparison, we have calculated the theoretical value of the spatial resolution σ_{PSF} of the IRIS CT scanner applying equation (4.5). In the gaussian approximation, the FWHM resolution and the σ in the spatial domain of each contribution are connected by the relationship: σ = (FWHM/2.355). It results that σ_{foc} = 21.23 µm. For the x-ray detector, we know from specifications provided by the manufacturer that the spatial resolution at 20 % of the MTF is 6.5 lp/mm, resulting in σ_{det} = 43.92 µm, as obtained by the following equation:

$$\sigma_{det} = \frac{\sqrt{2 \ln 5}}{2\pi f_{20\,\%}}. \tag{4.17}$$

The algorithm component σ_{alg} can be finally estimated approximating the triangle function to a gaussian one with a FWHM equal to the detector sampling pitch, resulting in σ_{alg} = 31.85 µm [50]. As it can be seen, the dominant contribution is from the x-ray detector. Finally, applying equation (4.5), it results σ_{PSF} = 45.56 µm, corresponding to $f_{10\,\%} \approx 7.5$ lp/mm in the frequency domain and a low contrast detectability R_{10} of 66.6 µm.
As it can be noticed, the measured R_{10} value diverges significantly from the theoretical one. This important difference confirms what we have supposed before, i.e. a total geometric calibration of the scanner should be necessary.

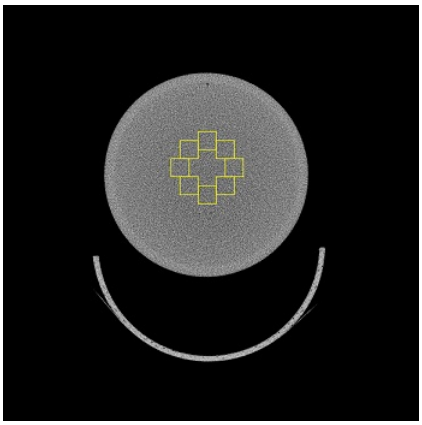

Figure 4.4: Transaxial slice of the water phantom used for NPS CT images measurements. With a reconstructed voxel size of 60 µm, ROIs size is set to 50×50 pixels. Their circular disposition is displayed.

Noise of micro-CT images

The bidimensional NPS of the micro-CT scanner was calculated from water phantom reconstructed images. The phantom was a water-filled plexiglas cylinder with a outer diameter of 30 mm and images were acquired with different scanning protocols in order to analyse NPS of CT images under several conditions. ROIs size and disposition was obviously adapted to CT images, also according to the reconstructed voxel size. Anyway, for all reconstructed images, eight ROIs were placed along a concentric circle centered at about the center of the water phantom as Figure 4.4 shows. It represents a reconstructed image of the water phantom with a voxel size of 60 µm. In this case ROIs size was set to 50×50 pixels, as for those ones reconstructed with a voxel size of 80 µm, whereas for images with a voxel size of 120 µm, ROIs size was set to 30×30 pixels. Before Fourier transforming, a zero padding with 200 samples was perfomed on the selected ROIs of 50×50 pixels, while it reduces to 120 samples when ROIs of 30×30 pixels were used for the measurement. Then the procedure to measure the 2D-NPS, was the same as described above for the analysis of the NPS of the detector. In order to extract the NNPS, the 2D-NPS was divided by the square of the mean value of the pixels used for analysis (in units of digital value) [41]. The 1D-NNPS profiles were then obtained as described above. The 1D-NNPS profiles extracted from reconstructed images with a voxel size of 60 µm, are reported in Figure 4.5(a) for all tube voltages. More specifically, 2000 projection views were acquired at 35, 50, 65 and 80 kV with an exposure per frame of 0.28, 0.14, 0.070 and 0.045 mA/s.Images were reconstructed with the Ram-Lak filter. The mean dose that would delivered to an animal with a diameter equal to that of the phantom used here (30 mm) was calculated as explained in section 4.1.3 and values are reported in the legend of the

figure, in correspondance of the relatives tube voltages. Figure 4.5(b) illustrates the effect of the voxel size on the NPS. Profiles calculated from images that were reconstructed with a voxel size of 60 µm (the nominal voxel size) and 80 µm are reported up to the relatives Nyquist frequencies which are 8.50 and 6.37 mm^{-1}, respectively. In order to obtain images with a voxel size of 80 µm, the same projections views were reconstructed by only modifying the software binning, in the preprocessing protocol of the workflow. Finally NPS of CT images reconstructed with the three reconstruction filters (Standard, Smooth and Edge filter) were analyzed and Figure 4.5(c) shows the results. In this case, 576 projection views were acquired at 80 kV with an exposure per frame of 0.034 mAs. Images were reconstructed with a voxel size of 120 µm, resulting in a Nyquist frequency of 4.25 mm^{-1}.
Focusing on Figure 4.5(a) where spatial frequencies are reported up to the Nyquist one, it can be noticed that images acquired at 35 kV suffer from higher noise than images acquired at the other tube voltages. Figure 4.5(b) shows really clearly how noise decreases with increasing voxel size. Finally in Figure 4.5(c) the 1D-NNPS profiles extracted from images reconstructed with three reconstruction filters, give informations about how the choice of the reconstruction filter reflects on the image noise too. It can be observed that noise in an image reconstructed with the Edge filter is higher than the noise that charcacterizes images reconstructed with the other two filters.

For an analysis of image noise in the spatial domain, the coefficient of variation C_v measured on water phantom images are reported in Figure 4.6 as a function of the first four voxel sizes that are available for the IRIS scanner on the left, and as a function of the exposure in mAs units on the right. Images were acquired at the same exposure level to define the noise dependance from the voxel size, while tube current was changed in order to increase the exposure keeping fixed other parameters. The fitted data exhibit an inverse relationship between the coefficient of variation and approximately the fourth power of the isotropic voxel size and the square root of the exposure.

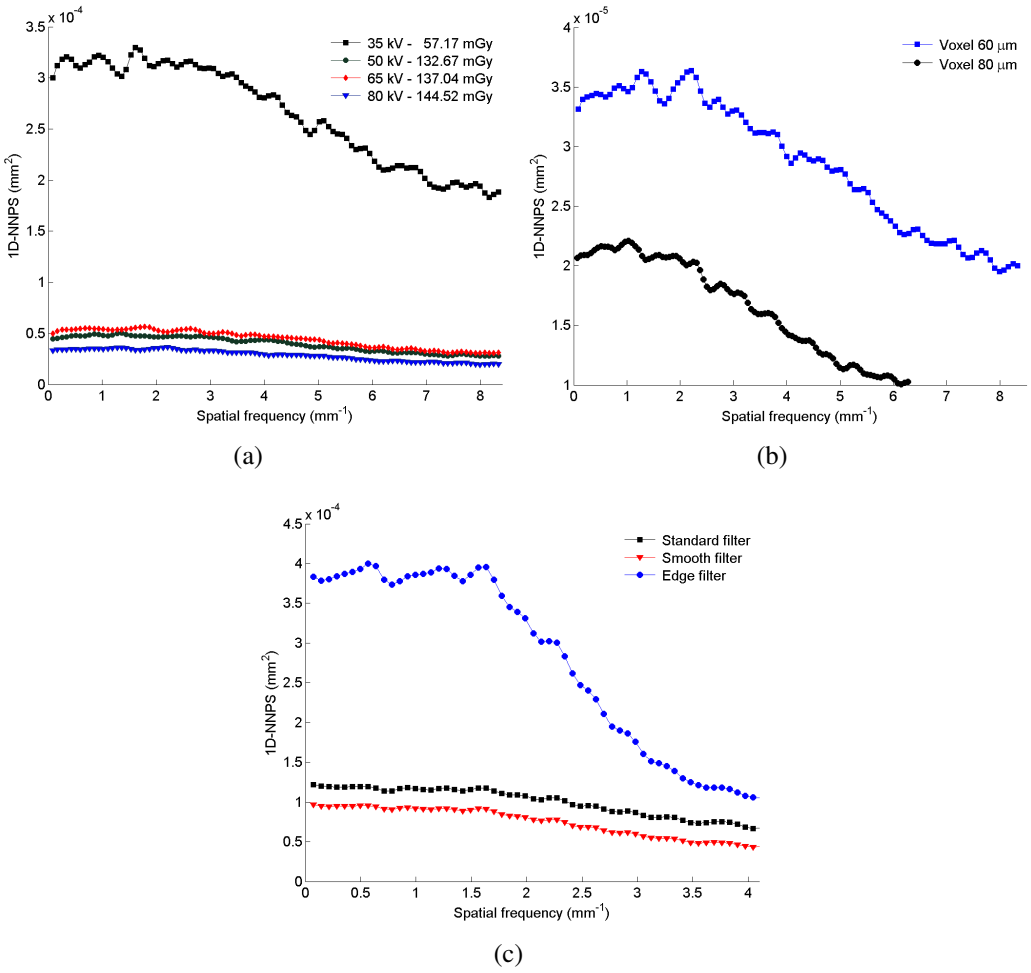

Figure 4.5: 4.5(a): 1D-NNPS profiles extracted from reconstructed images with a voxel size of 60 µm for 35, 50, 65, and 80 kV. The corresponding mean dose values that would deliver to a small animal with similar diameter of that of the water phantom (30 mm), are also reported. Mean dose values are calculated by means of $CTDI_{100,air}$ values reported in section 4.1.3, and Monte Carlo conversion factors adapted from [47]. 4.5(b) 1D-NNPS profiles extracted from reconstructed images with a voxel size of 60 µm and 80 µm. 4.5(c): 1D-NNPS profiles calculated from images reconstructed with a voxel size of 120 µm, with the Standard, Smooth and Edge filters.

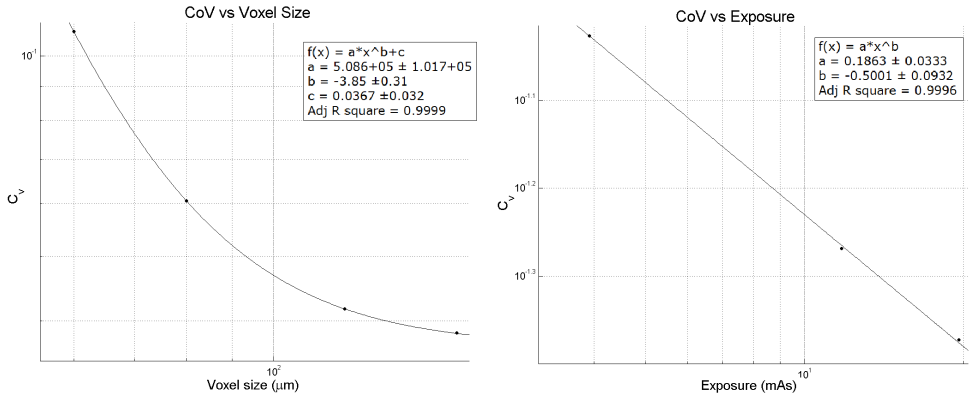

Figure 4.6: Coefficient of variations C_v values measured on the reconstructed images as a function of the voxel size on the left side, and the exposure in mAs on the right side. Measurements are referred to the water attenuation coefficient.

4.2.3 Image quality of fast dynamic imaging protocol

A useful feature of the IRIS micro-CT is its ability to acquire a sequence of tomographic images (dynamic mode) for application to perfusion studies. The evaluation of dynamic images often relies on the analysis of density, rather than on vessel segmentation because of different reasons that will appear clearer at the end of this section.
The dynamic mode is performed with the fastest protocol available which consists in acquiring ten consecutive frames at a tube voltage of 80 kV, a cathode current of 1 mA, and an exposure time per frame of 32 ms. This is a short scan protocol with an angular step of 0.9°, leading to 228 projection views that are collected by alternating the rotation direction of the gantry (anticlockwise for even frames, clockwise for the odd ones). Projection views are generally reconstructed with the smooth filter and a voxel size of 240 μm. The total scan time of the dynamic mode is 7.3 s per frame, with an interscan delay of 11.7 s was observed [23]. The main limiting factors of the dynamic mode are the mechanical design since the PET detector that is mounted on the same rotating gantry of the CT scanner does not permit a slip ring implementation, and, as for the interscan delay, the data transfer speed between consecutive scans. Geometric and CT number reproducibility of this protocol has been already evaluated in a previuos work giving successfully results as to adfirm that it seems promising for perfusion imaging, in both standalone CT or in conjunction with PET [23].

In this section the imaging performances of the IRIS dynamic mode will be further investigated. For this purpose a hollow plexiglas phantom with inner diameter of 40 mm, that corresponds to the typical rat size, was modified by adding inside its water filled cavity, five Eppendorf micro test tubes containing mixtures

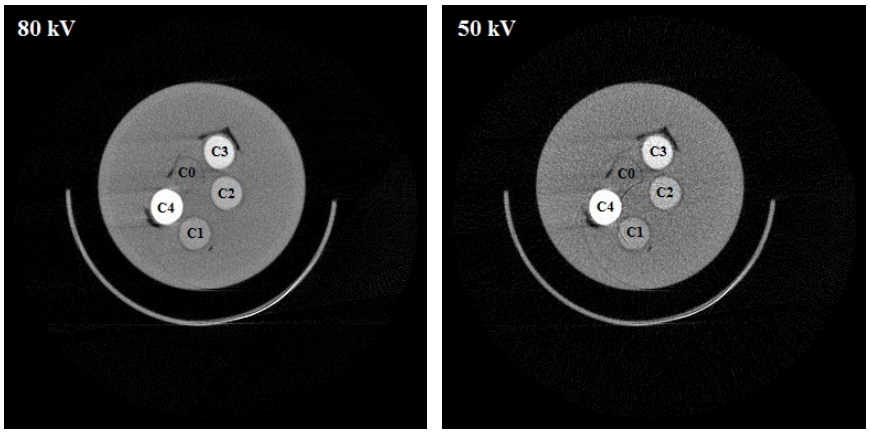

Figure 4.7: Comparison of two transaxial slices of the phantom acquired with the dynamic protocol at 80 kV (on the left) and at 50 kV (on the right). Streaking artifacts due to angular undersampling are noticeable in both images, while in that one acquired at 50 kV ther are also ring artifacts. For both images the display window (min; max) is (−1000 HU; 1000 HU). The iodine concentrations corresponding to C0, C1, C2, C3, C4 are reported in the text.

of water and iodinated CA (Iomeron 400, Bracco, Italy) with the following concentrations:

C0: Water
C1: Water+CA, 3.87 mg I/mL
C2: Water+CA, 7.74 mg I/mLL
C3: Water+CA, 15.5 mg I/mL
C4: Water+CA, 32.0 mg I/mL

Phantom images were therefore acquired with the scanning protocol above described, or even, four acquisitions at the different tube voltages were perfomed, keeping fixed all the other parameters (tube current, exposure time per frame, rotation mode, reconstruction filter, voxel size). In Figure 4.7 transaxial slices of the reconstructed phantom at the tube voltage of 80 and 50 kV are reported. As expected, due to the short scan times, different kind of artifacts are noticeable. In both images streaking artifacts due to the angular undersampling of the SS acquisition mode in cone-beam geometry, are really evident [51]. At 50 kV, ring artifacts are also present. This kind of image degradation is generated by noise in the projection data that is rotationally invariant, that is, has the same pattern and intensity for all projection angles. This kind of noise is interpreted by the reconstruction algorithm as a rotationally invariant feature of the object itself (rings) [4]. The reconstruction algorithm interpret such inconsistencies as circularly symmetric features in the object under examination. This effect is more often observed in cone beam CT systems based on flat-panel detector than in clinical scanners,

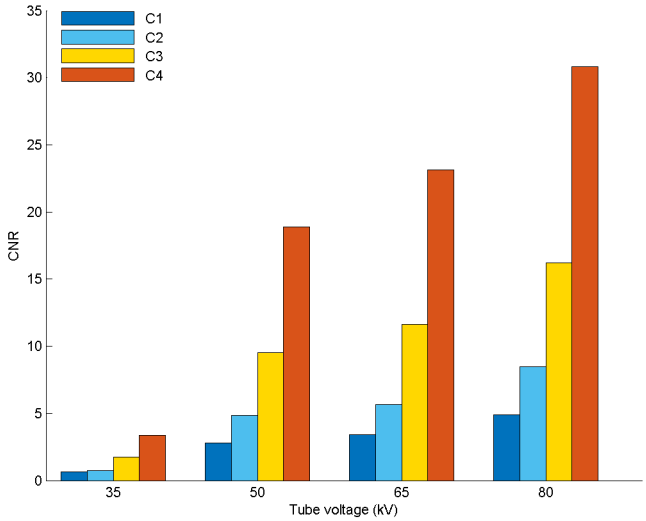

Figure 4.8: CNR for all iodine concentrations and for all tube voltages relative to the fast scanning protocol designed for time-resolved 3D imaging.

just because reaching a good gain equalization among all detection elements in flat-panel detector is much more challenging due to the high number of pixels and independent read out channels, as well as usually very small size of each pixel. Gain equalization is in most cases carried out by acquiring a flat field image with higher counting statistics as possible. Figure 4.7 is an example of the failure of the ring artifact correction probably because of the low counting statistics at 50 kV, resulting in a insignificant gain equalization.

This phantom was scanned to analyze the CNR for large object scale in terms of iodine concentration and results are graphically reported in Figure 4.8 for all tube voltages and for all iodine concentrations. It can be noticed that at 80 kV the lowest iodine concentration (3.87 mg I/mL) borders on the Rose threshold with a CNR of 4.9. CNR values decrease with decreasing tube voltage because of the sensitivity of the tomographic system to iodine that increase with tube voltage. At 35 kV CNR values are in fact all above the threshold. As already expected, the 35 kV setting is the less useful for CT perfusion studies since the sensitivity of the system to iodine concentration is very low, and together with the little fluence rate, which reflects on noisy images, make this setting inappropriate for imaging dynamic mode.

In order to analyse the detecability of the fast dynamic protocol, a CNR analysis in terms of object size was also perfomed. We in fact expected that images are affected by the Partial Volume Effect (PVE) [52]. It is due to the finite spatial resolution of the imaging system and it arises at the interface between two

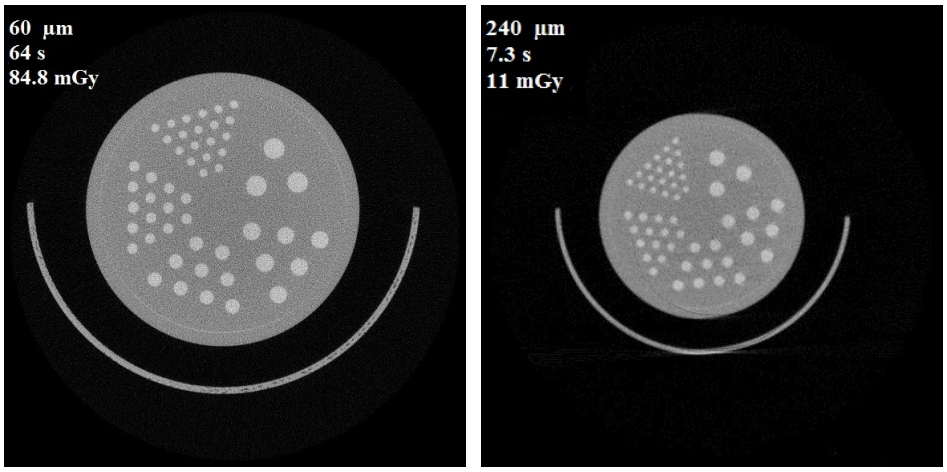

Figure 4.9: Transaxial slices of the Derenzo phantom filled with a iodine concentration of 9.62 mg I/mL. On the left, image acquired at 80 kV with the high resolution scanning protocol corresponding to 1280 projection views acquired in 64s and reconstructed with a voxel size of 60 µm. The resulting mean dose value to rats is 84.8 mGy. On the right, image acquired at 80 kV with the SS protocol designed for the dynamic mode corresponding to 228 projection views acquired in 7.3 s and reconstructed with a voxel size of 240 µm. The resulting mean dose value to rats is 11.0 mGy. For both images the display window (min; max) is (−1000 HU; 1000 HU).

different materials where a mix of the two corresponding attenuation values can be noticed. The result is that the image of a small source is a larger but dimmer source. Therefore we expected that for low resolution protocols this effect is more prominent, especially in correspondence of object whose size is of the order of magnitude of the spatial resolution.
For this analysis a Derenzo phantom, which is generally employed to evaluate the imaging perfomances of PET scanners, was used. In this case it was filled with a mixture of iodine-based CA and water resulting in a concentration of 9.62 mg I/mL. This solution was not randomly chosen, but it approximately corresponds to the iodine concentration that perfuses small animal vascular network. Derenzo phantom was therefore scanned with the fast dynamic imaging protocol, that is with the lower resolution protocol available in IRIS/CT scanner. An acquisition with a higher resolution was also perfomed. It consisted in 1280 projection views acquired in a total time of 64 s and reconstructed with a isotropic voxel size of 60 µm. Figure 4.9 shows transaxial slices of this phantom reconstructed with both protocols at the tube voltage of 80 kV. It contains several cylindrical cavities of different diameters that have been measured from images reconstructed with the higher resolution protocol with *ImageJ*. Measurements gave the following results: 0 99 +− 0 05, 1 43 +− 0 09, 1 92 +− 0 08, 2 41 +− 0 08, (2.90 ± 0.04) mm. CNR was evaluated for both protocols at 50, 65 and 80 kV and results are graphically

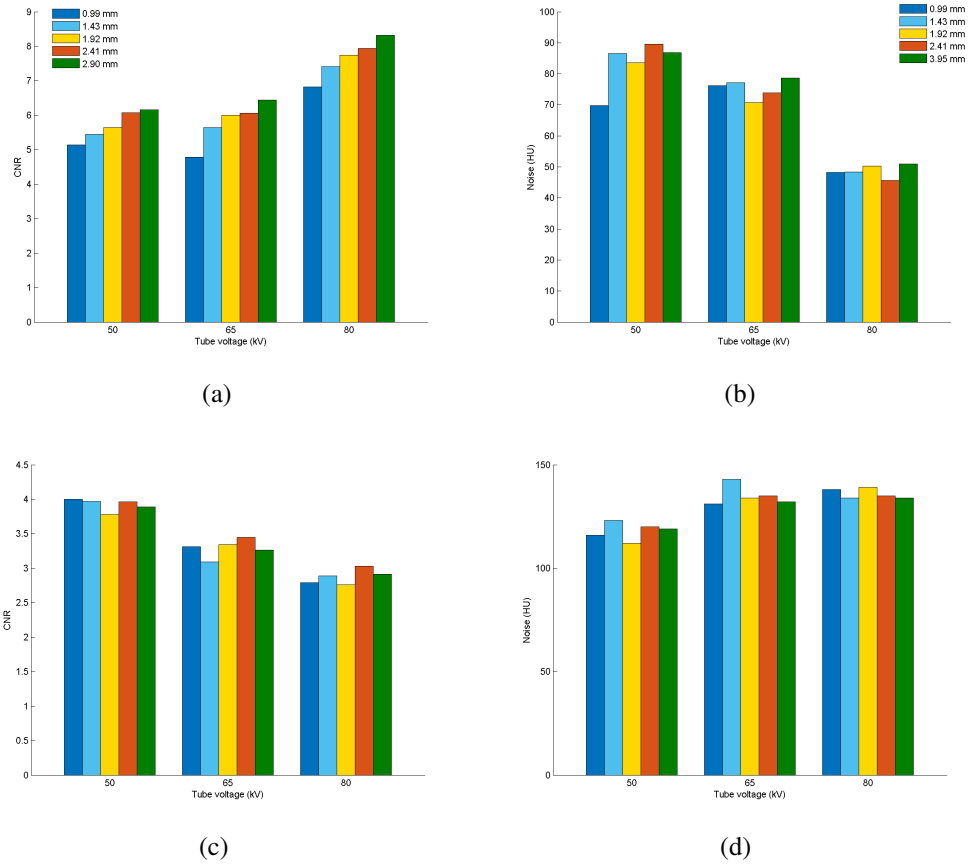

Figure 4.10: 4.10(a) and 4.10(b): Contrast to Noise Ratio (CNR) for a iodine concentration of 9.62 mg I/mL and noise in HU in the plexiglas background relatives to the fast dymanic protocol. 4.10(c) and 4.10(d): CNR for a iodine concentration of 9.62 mg I/mL and noise in HU in the plexiglas background relatives to the high resolution protocol. CNR and noise values are reported for the tube voltage of 50, 65 and 80 kV and for all diameters of Derenzo phantom, reported in the legend, and for both scanning protocols.

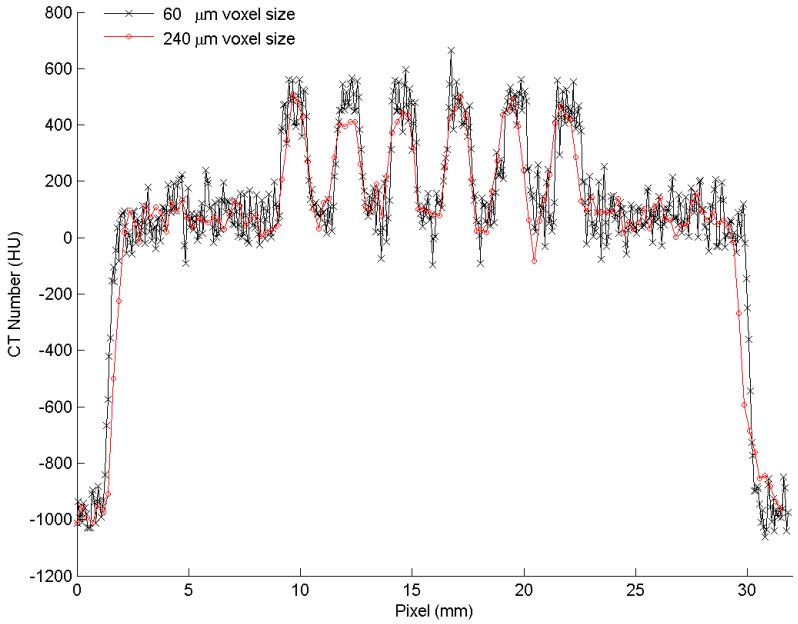

Figure 4.11: Profiles of the smaller inserts (diameter of 0.99 mm) of Derenzo phantom relatives to images acquired at 80 kV with the high resolution protocol (60 μm voxel size) and the fast dynamic protocol (240 μm voxel size). Profiles are reported in black and red, respectively.

reported in Figures 4.10(a) and 4.10(c). For the same phantom measurements, the corresponding noise levels in the plexiglas background, calculated as the standard deviation of the CT numbers, have been also reported in Figures 4.10(b) and 4.10(d). For CNR maesurements, a circular ROI was placed in each cavity in order to compute the mean and the standard deviation of CT numbers. More specifically, three cavities were considered for each diameter size and results were then averaged. ROIs size was adapted each time to the dimension of the cavity. As it can be observed from Figure 4.10(a), CNR values decrease on smaller inserts, confirming that PVE affects images acquired with the fast scanning protocol. CT signal in images acquired with the higher resolution protocol is not significantly altered, instead. It can be noticed from CNR values reported in Figure 4.10(c) since they do not show a particular trend as a function of the object size. Noise values are direct consequences of the tube settings and the voxel size: for the fast dynamic protocol we have lower values at the tube voltage of 80 kV, while for the high resolution one, noise values are lower at 50 kV to which correspond a higher exposure time. In support of this theory, we reported in Figure 4.11 the profiles of the smaller inserts of Derenzo phantom relatives to images acquired at 80 kV with the two scanning protocols. In Table 4.3 the total scan time and the mean dose

Tube voltage (kV)	Total scan time (s)		Dose to mice (mGy)		Dose to rats (mGy)	
	60 μm	240 μm	60 μm	240 μm	60 μm	240 μm
50	224	7.3	117.87	3.84	96.05	3.13
65	89.6	7.3	95.07	7.75	81.13	6.61
80	64	7.3	96.55	12.52	84.77	11.00

Table 4.3: Total scan time in s and mean dose in mGy delivered to mice and rats (diameters of 20 and 40 mm respectively) for the high resolution and fast dynamic protocols which are indicated with the corresponding voxel size (60 μm and 240 μm, respectively.) Mean dose values are calculated by means of $CTDI_{100,air}$ values reported in section 4.1.3, and Monte Carlo conversion factors adapted from [47].

values to mice and rats are reported for the high resolution and the fast dynamic protocol at the three tube voltages considered in the analysis above. We can conclude affirming that at the state of the art of the fast scanning protocol designed for dynamic studies, the tube setting of 80 kV should be employed, since it results the best in terms of image noise, CT enhancement and image artifacts.
At the time of writing of this thesis, phantoms with smaller inserts than those of the Derenzo phantom were not available, so it will be interesting to performe other studies on smaller structures (of the order of μm for example) to further investigate how the PVE affects images acquired with the fast scanning protocol.

4.2.4 Hounsfield Unit calibration

As explained in Chapter 1, image reconstructed data are expressed in CT numbers in Hounsfield Unit (HU). μ_{eff} and hence CT numbers, are affected by the x-ray tube voltage, beam filtration, and object thickness. Thus, possible reasons for medium-term and long-term drifts of the μ_{eff} values, are related to (microscopic) changes in the tube output, or detector dark signal and temperature drift.
Because all real images are always affected by noise, it is more correct to say that a calibrated CT image must be such that the average value of the reconstructed voxels within a ROI uniformly occupied by water, is $\langle \text{CT\#} \rangle_{\text{ROI}} = 0\,\text{HU}$.
A plexiglas water phantom with a inner diameter of 25 mm was used to calibrate CT numbers. It was scanned using the P160-AllkV-FS protocol and the reconstructed image data, in HU, were reported in μ_{eff} applying the inverse formula of equation (1.42) with the known $\mu_{\text{eff,water}}$ coefficients, which were the ones that were used to express image data in HU units. 200 slices of the reconstructed water phantom were averaged in order to result in a smaller standard deviation σ of $\mu_{\text{eff,water}}$. In order to evalute the new value of $\mu_{\text{eff,water}}$, the mean value of a circular ROI of size 90×90 pixels centered with respect to the cylinder was measured. The size of ROI was such as to taken into account the beam hardening effect. The

Tube voltage (kV)	$\mu_{\text{eff,water,old}}$ (mm^{-1})	$E_{\text{eff,old}}$ (keV)	$\mu_{\text{eff,water,new}}$ (mm^{-1})	$E_{\text{eff,new}}$ (keV)	Difference (%)
35	0.037	30.3	0.0406	28.5	9
50	0.027	39.7	0.0285	37.7	5
65	0.023	48.9	0.0245	44.7	6
80	0.0209	57.9	0.0225	50.8	7

Table 4.4: The old effective linear attenuation coefficient of water ($\mu_{\text{eff,water}}$) and new ones are reported for all tube voltages of the IRIS scanner. Their relatives effective energies E_{eff} values have also been reported as reference together with the variation percentage of $\mu_{\text{eff,water}}$.

results of the calibration are summerized for all tube voltages in Table 4.4. Besides the old $\mu_{\text{eff,water}}$ and the new ones, obtained from the calibration, the energy values corresponding to $\mu_{\text{eff,water}}$ are reported as E_{eff}. These values were provided by *XMuDat* [26]. Before calibration, we have noticed a mean percentage variation of $\mu_{\text{eff,water}}$ of 7 % (in Table 4.4 the percentage variation for each tube voltage is reported).

4.2.5 Beam hardening correction

In computed (micro)tomography, the term *artifact* is applied to any systematic discrepancy between the CT numbers in the reconstructed image and the true attenuation coefficients of the object [53]. Artifacts can be grouped into four categories, depending on their nature:

- physics-based artifacts, which result from the physical processes involved in the acquisition of CT data;
- patient-based artifacts, which are caused by such factors as patient movement or the presence of metallic materials in or on the patient;
- scanner-based artifacts, which result from imperfections in scanner function;
- helical and multisection artifacts, which are produced by the image reconstruction process.

Beam Hardening artifact falls into the first group and it is due to the polychromatic x-ray beam. Because of the energy dependence of the photoelectric absorption, a heterogeneous beam traversing an absorbing medium becomes relatively richer in high-energy photons, and hence more penetrating, or *harder*. Hence the attenuation produced by a given material, defined as the negative logarithm of the ratio of

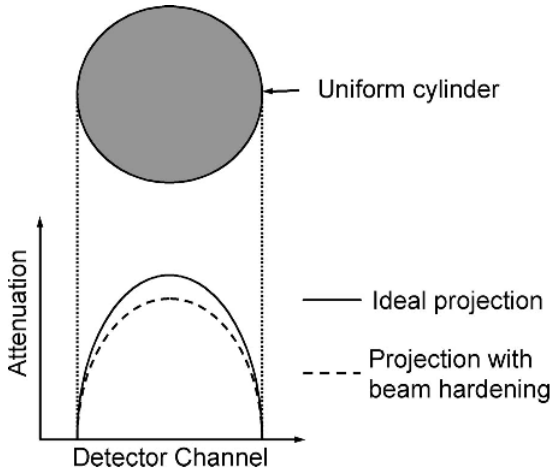

Figure 4.12: Attenuation profiles obtained with and without beam hardening for an x-ray beam passing through a uniform cylindrical phantom. Image is adapted from [53].

transmitted (I) to incident intensities (I_0), is not strictly proportional to its thickness. This is in fact strictly true only for monochromatic source, as the follow equation assumes:

$$\mu d = -\ln\left(\frac{I}{I_0}\right). \tag{4.18}$$

Two types of artifact can result from this effect: the so-called cupping artifacts and the appearance of dark bands or streaks between dense objects in the image. X rays passing through the middle portion of a uniform cylindrical phantom are in fact hardened more than those passing though the edges because they are passing though more material. As the beam becomes harder, the rate at which it is attenuated decreases, so the beam is more intense when it reaches the detectors than would be expected if it had not been hardened. Therefore, the resultant attenuation profile differs from the ideal profile that would be obtained without BH, as it is illustrated in Figure 4.12. Dark bands or streaks occur because the portion of the beam that passes through one of the objects at certain tube positions is hardened less than when it passes through both objects at other tube positions. This type of artifact can occur both in bony regions of the body and in scans where a contrast medium has been used.

The effect of BH can be corrected in several ways. It is common to reduce it by filtering of the spectrum in which soft photons are removed. However the decreasing amount of X-rays results in a decrease of the image SNR as such that prolonged exposure is needed. A second, commonly correction method is based on a linearization procedure. For polychromatic source a deviation from the expected linear trend is noticed and fitting the measured nonlinear relationship with

polynomials, BH can be corrected, as every value on the polynomial is corrected towards the linear trendline which is expected in the monochromatic case. However this method is material dependent since it works only on a two-component system, such as air and another material. For systems consisting of more than two components, this method is often used in combination with the projection data and a first reconstruction image to obtain more prior information about the object under investigation [54].

The IRIS scanner BH correction was performed by the water precorretion method, which consists in applying the linearization technique explained above to a water phantom. The goal was to determine the coefficients $c_{i,\mathrm{wc}}$ of the fourth-order polynomial $\mathrm{p_{wc}}$ by which BH correction can be implemented:

$$\mathrm{p_{wc}} = \sum_i c_{i,\mathrm{wc}} x^i \tag{4.19}$$

where x is the attenuation. When BH correction is not implemented, $c_{i,\mathrm{wc}}$ are: 0, 1, 0, 0, 0 for $i = 0, 1, .., 4$.
The phantom used for the measurements was a water-filled plexiglas with a inner diameter of 25 mm which was scanned with a multi-energy protocol in order to correct BH effect for the all available tube voltages. A central slice of image reconstructed data sets was considered in order to make well founded the approximation of the cone beam geometry to a fan beam one. With these considerations, it is possible to state that the beam traversing the water cylinder, covers the same path length at each angular projection. Furthermore reconstructed image data were processed with *ImageJ* since both plexiglas thickness was to be removed in order to deal with a two-component system, and data, in HU units, were to be reported in attenuation coefficient values. For this purpose, the inverse formula of equation (1.42) was employed. An attenuation profile was therefore extracted. In Figure 4.13 the attenuation profile obtained from the reconstructed image at 80 kV is reported as a function of the pixel position, in mm units. The water thicknesses L that the beam traverses were calculated in the following manner:

$$L = 2\sqrt{\mathrm{R}^2 - (\mathrm{C} - \mathrm{Pixel})^2} \tag{4.20}$$

where R and C are the radius and the center of mass of the segmented water phantom, respectively. More specifically R was calculated as the half of the difference between the two pixel positions corresponding to the first attenuation values different from zero, while C was measured with *ImageJ*. The calculated L values were then plotted as a function of attenuation data. First of all it was assured that there was a correspondance between the symmetric values of attenuation data and L values. For this purpose, the center of mass C was oppotunately modified until a reasonable matching was reached. Water thicknesses L were then fitted with a

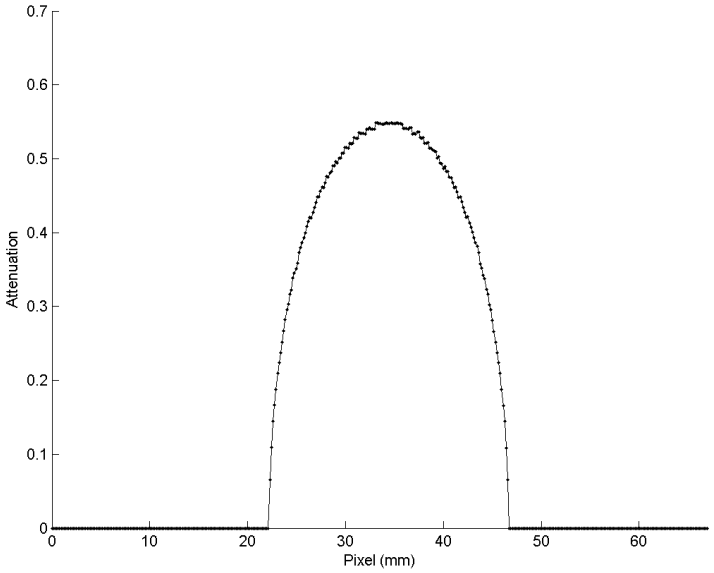

Figure 4.13: Attenuation profile obtained from reconstructed image of the water phantom used for BH correction at the tube voltage of 80 kV.

fourth-order polynomial in *MATLAB* enviroment. The results obtained from the analysis on the water phantom image at 80 kV, are graphically reported in Figure 4.14. As reference, the linear trend that data should have, has also been reported. The linear trend was obtained by fitting with a first-order polynomial only L values up to 6 mm since it can be assumed that for small thicknesses the effect of BH is negligible. The divergence from the linear trend is evident. In Table 4.5 the fourth-order polynomial coefficients obtained from fit have been reported. The agreement between L values and the fit with the fourth-order polynomial is confirmed by the coefficient of determination (R^2) and the Sum of Squares due to Error (SSE) which are equal to 1 and 2.032.

	Fourth-order polynomial coefficients
c_0	0 (fixed at bound)
c_1	43.97 ± 1.23
c_2	−5.33 ± 10.4
c_3	15.55 ± 28.06
c_4	−6.44 ± 24.17

Table 4.5: Polynomial coefficients obtained from fit in *MATLAB* with 95% confidence bounds.

Beam hardening effect can be therefore eliminated by implementing the coef-

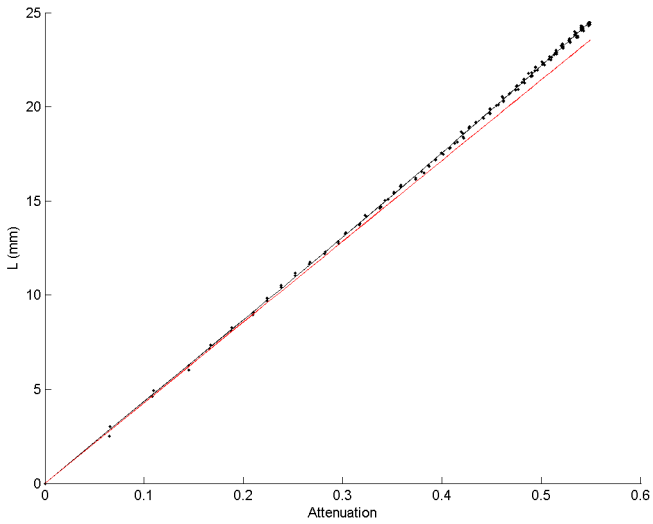

Figure 4.14: Water thickness L as a function of attenuation data at 80 kV. Fit with the four-order polynomial is represented with a black line while the linear trend is shown with a red line.

ficients $c_{i,\mathrm{wc}}$ calculated as the ratio between the fourth-order polynomial and the linear regression line of equation: $r(x) = c_1 x + c_0$, where c_1 and c_0 are the coefficients of the fourth-order polynomial.
By performing the same measurements on images acquired at the other tube voltages (35, 50, and 65 kV), it was noted that the BH correction was necessary for all tube voltages. In order to confirm or invalidate the obtained coefficients, the BH correction was implemented on water phantom greater (diameter of 40 mm) than that one used for the analysis. Transaxial slices of the reconstructed water phantom are reported in Figure 4.15 before and after BH correction. The relative CT number profiles are reported in Figure 4.16. As it can see, cupping artifact is reduced after the correction. In order to further investigate the effects of BH correction on reconstructed images, the uniformity of the reconstructed images before and after the BH correction, was also evaluated. More specifically the mean value and the standard deviation σ of CT numbers in circular ROIs was measured. ROIs were placed at the center and at the edges of the water phantom, as Figure 4.17 shown. Finally, we have calculated the difference between the CT number measured in the central ROI and the mean of CT numbers obtained at the edges. In Table 4.6 the measured values in HU units are reported. As it can be noticed, before BH correction, the difference between the center of the water image and its edges amounts to 19.5 HU, while it reduces up to 2.3 HU when images are corrected from BH.

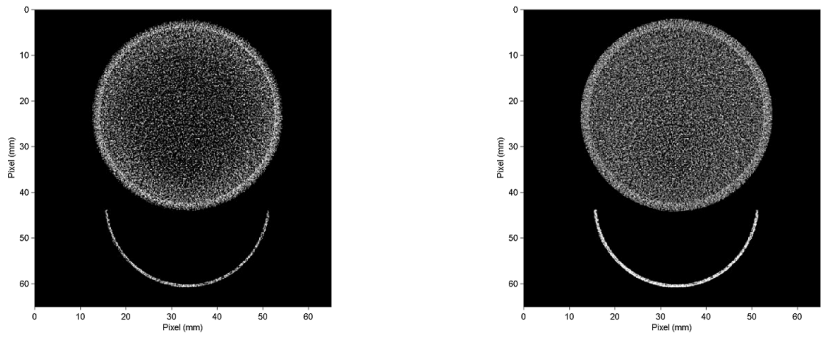

Figure 4.15: Transaxial slices of the reconstructed water phantom before (left) and after (right) BH.

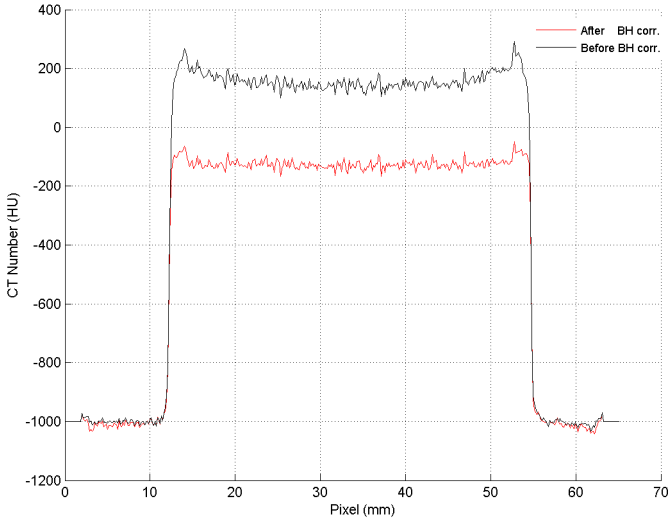

Figure 4.16: CT number profiles of the water phantom relatives to images reconstructed before BH correction, in black, and after, in red.

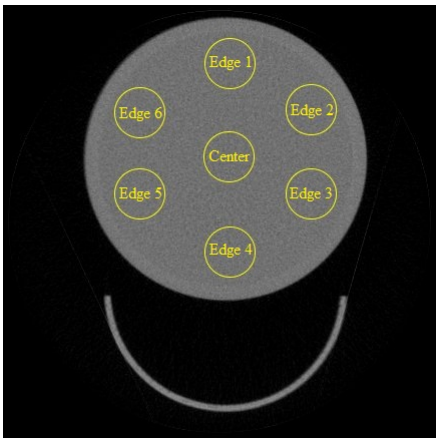

Figure 4.17: Transaxial slice of the water phantom were the ROIs considered for the image uniformity test have been graphically reported.

	Before BH correction		After BH correction	
	Mean (HU)	σ (HU)	Mean (HU)	σ (HU)
Center	159	63	-118	48
Edge 1	174	62	-119	46
Edge 2	180	57	-114	45
Edge 3	178	61	-115	44
Edge 4	179	60	-115	45
Edge 5	179	60	-116	46
Edge 6	181	59	-115	44
Homogeneity	19.5		2.3	

Table 4.6: Mean and standard deviation values in HU units measured in circular ROIs placed at the center and at the edges of the water phantom in order to verify the improvement of image uniformity after the implementation of BH correction. The homogeneity of reconstructed images, i.e. the difference in HU between the central value and the average of values at the edges are also reported.

Chapter 5

Phantom studies with metal Nanoparticles

Introduction

Progresses in nanotechnology are paving the way for the development of new CAs. The very interesting properties of nanoparticle based CAs attract by now the attention of molecular imaging research so that there are many studies in literature focused on confirming, and in the same time discovering, all the possibilities that they can offer in this field. One of the aims of this thesis was indeed to investigate the response of this recent CA in x-ray imaging. The obtained results must be meant as just preliminar results, since both the properties of the specific metal NPs and their response to x-rays are still being analyzed in more in-depth studies. In this chapter the first results that were obtained in phantom studies employing gold and platinum NPs are presented. This work was done in collaboration with the Center for Nanotechnology Innovation@Nest, Istituto Italiano di Tecnologia, who have provided the candidate nanoparticle-based CA under investigation.

5.1 Materials and methods

Numerical simulation aimed to give a replication of the physical processes involved in micro-CT imaging. Simulations allowed to theoretically investigate the response of the IRIS CT scanner to metal types and concentrations of NPs. Furthermore, simulations provided a first guidance to chemists for improving the formulation of NPs for the purpose of CT CAs. Monte Carlo simulation would require much more efforts and was not the main aim of this thesis. Despite the cone beam geometry of the IRIS micro-CT, a 2D object in a fan beam geometry was simulated for the sake of semplicity using analytical computation of polychro-

matic projection data with simple test objects. The real IRIS geometry reduces to the simulated fan beam geometry in the proximity of the medial transaxial plane, i.e., for z~0. Iodinated CA and metal NPs were used in simulated phantom studies in order to compare CAs response to x-rays. The assessment of the sensitivity, which is expressed in HU/mg/mL unit, of the system to metal NPs, was the first goal of such simulations. Phantom studies in which a iodinated CA was employed, were also used as benchmark in order to assess the simulation accuracy by direct comparison with already available experimental data.

5.1.1 Two-dimensional phantom simulations

Before describing the manner in which numerical simulation was implemented, we will focus on the fundamental role that the choice of the phantom plays in a micro-CT study and the consequences which this entails. Phantom studies should attempt to mimick the same conditions of an animal study. First of all cylindrical phantom, in 3D space, are simpler to simulate with respect to other phantom shape because x-rays would traverse the same thickness of material for each angular projection. For the same reasons, such a phantom, but also any other object or small animal, would be placed in the scanner FOV parallel to the AOR. Phantom material is another aspect that should not be underestimated. Plexiglas phantoms are usually employed, since the linear attenuation coefficient of this material is similar to that of water, which in turn behaves like soft tissue.

Phantom imaging simulations were realized evaluating all steps concerning with x-ray imaging, from x-rays production to image reconstruction, by means of both available software packages and MATLAB code newly written within this thesis. It is reported in Appendix A. More specifically, *SpekCalc Windows release 1.1* was used to simulate x-ray spectra at different kilovoltages [25], while material attenuation values as a function of the energy were provided by *XMuDat*[1] [26]. The simulated projection images were reconstructed by the software *CtRecon*, developed at the Functional Imaging and Instrumentation Group (FIIG) of the Dept. of Physics "E. Fermi", University of Pisa.
X-ray spectra provided by the software were first of all corrected for the attenuation that beam suffers when it exit the tube window. For this purpose, a MATLAB code was written using equation (1.3). Both spectra and attenuation coefficients were calculated by setting the energy bin to 0.5 keV as it was considered a reasonable pitch, that is a good comprimise between energy resolution and computational time. The total attenuation coefficient was employed in simulations, assuming that all the photons were completely removed from the beam independently of the type of interaction that have undergone in the phantom material.

[1]The attenuation coefficients provided by *XMuDat* come from the NIST database.

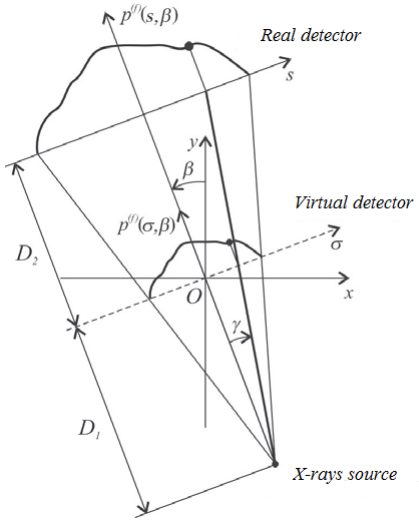

Figure 5.1: Schematic view of the fan beam geometry. The relationship between fan beam coordinates (s,β) and the parallel beam ones (t,θ) are also reported together with the positive direction of angles.

This simplification is necessary in analytical simulations, where photon scattering is hard to model and implement. Nevertheless, at low energy ($\leq 100\,\mathrm{keV}$) we assumed that this approximation was sufficiently reliable for the actual purposes of our simulations, i.e., simulating the tomographic image contrast by varying the NPs concentrations.
A circular composite phantom was therefore simulated in 2D space, according to the fan beam geometry. For a circle with radius $\mathrm{R_n}$ and centered in $(\mathrm{x_n}, \mathrm{y_n})$, the chord lenghts L that a ray of the beam traverses can be calculated as follows:

$$\mathrm{L}(t,\theta) = \sqrt{\mathrm{R_n^2} - [t - \mathrm{s_n}\cos(\gamma_\mathrm{n} - \theta)]^2} \tag{5.1}$$

where $\mathrm{s_n} = \sqrt{\mathrm{x_n^2} + \mathrm{y_n^2}}$, $\gamma_\mathrm{n} = \tan^{-1}(\mathrm{y_n}/\mathrm{x_n})$ and t and θ are the coordinate pair representing a line integral, as defined in section 1.2.1. However equation (5.1) is relevant only for a parallel beam geometry. For a fan beam geometry we must take into account the x-ray beam divergence. Line integrals are therefore calculated by the coordinate pair (s, β) and the projection corresponding to a specific angle β is represented by the function $p(s,\beta)$, as Figure 5.1 shows. Thus, the chord lenghts L in a fan beam geometry have been calculated as follows:

$$\mathrm{L}(s,\beta) = \sqrt{\mathrm{R_n^2} - \left[\frac{\mathrm{SAD}s}{\sqrt{(\mathrm{SAD}+\mathrm{ADD})^2 + s^2}} - \mathrm{s_n}\cos(\gamma_\mathrm{n} - \beta + \tan^{-1}\frac{s}{\mathrm{SAD}+\mathrm{ADD}})\right]^2}, \tag{5.2}$$

where, according to the IRIS geometry, Source to Axis Distance (SAD) is 206 mm and Axis to Detector Distance (ADD) is 56 mm; the simulated detector, centered with respect to the x-ray source, consists in a row of pixels with side size equal to 0.3 or 0.15 mm, corresponding to a pixel rebinning 4×4 and 2×2, respectively. With an angular step of 0.625°, 576 projection views have been simulated, since $0°<\beta_j<360°$.
In order to get the fan beam sinogram $P(s,\beta)$ of the simulated object, equation (1.3) was conveniently modified with equation (5.2) in order to firstly obtain the number of the unattenuated photons reaching the detector:

$$\mathrm{N}(s,\beta,E) = \mathrm{N}_0(s,\beta,E)e^{-2\sum_n \mu_n(E)\mathrm{L_n}(s,\beta)} \tag{5.3}$$

where N_0 are the photons that would reach the detector if no object were present (thus it represents a flat field image), and the sum is taken over the n materials that the beam traverses. The energy dependency takes into account that the beam is polychromatic, so the number of photons N have been calculated for each energy bin. Next, the Energy Absorption Efficiency (EAE) of the scintillator screen has been considered according to equation (1.12), as not all N will be converted to visible light and thus detected. The detected photons are finally summed up in order to delete the energy dependence, obtaining an "intermediate dataset" of the fan beam sinogram $P(s,\beta)$. As it can be deduced, it is calculated in the following manner:

$$P(s,\beta) = -\ln\left(\frac{\mathrm{N}(s,\beta)}{\mathrm{N}_0(s,\beta)}\right). \tag{5.4}$$

Sinogram is finally reconstructed by *CtRecon*, obtaining a 2D simulated phantom. More specifically, the reconstructed values correspond to the effective linear coefficients μ_{eff} which are then converted in HU units, according to equation (1.42). For this purpose a water phantom was also simulated in order to get $\mu_{\mathrm{eff,water}}$.
Phantom simulations were performed for all tube voltages that are available in IRIS scanning protocols. The fan beam sinogram of the simulated phantom at 80 kV is reported on the left side of Figure 5.2 and the relative reconstructed image on the bottom right, while a reconstructed water phantom image at 80 kV, is reported on the top. It represents a section of a plexiglas cylinder with a diameter of 50 mm. It contains five small wells, all of them placed at the same distance from its center, and with a diameter of 6 mm. They can be filled with a generic solution of known elemental composition in order to evaluate the resulting CT numbers. In the example reported in Figure 5.2, wells are filled with a mixture of iodine and water. As it can be noticed from reconstructed images, simulation represents a very ideal case since no noise was taken into account. The main purpose of the simulations described in this section was to investigate the behaviour of CT image contrast in the IRIS scanner as a function of the NPs concentration;

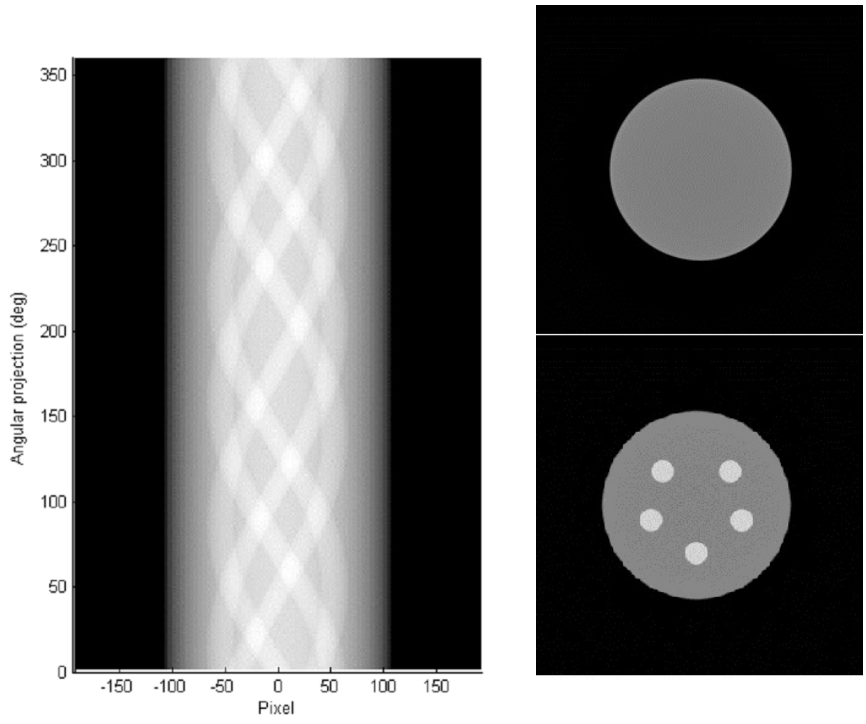

Figure 5.2: On the left the fan beam sinogram of the compostite simulated phantom at 80 kV. The relative reconstructed image is on the bottom right side, while a reconstructed water phantom image is reported on the top. The hardware binning was set to 4×4. For both reconstructed images the display window (min; max) is (−1000 HU; 1000 HU).

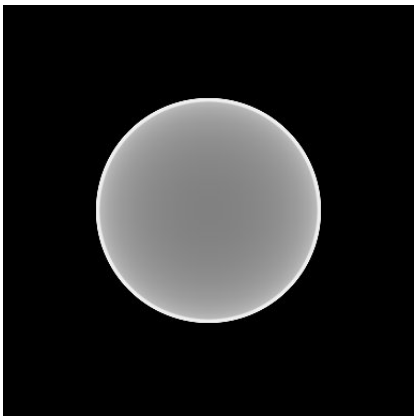

Figure 5.3: Simulated water phantom at 80 kV with a hardware binning 4×4. The display window (min; max) is (−100 HU;100 HU) as to enphasize how Beam Hardening (BH) is well reproduced by simulations.

hence, the noise was not included for simplicity. Actual measurements of CNR were performed with real experiments, as described later. Nevertheless the BH effect is reproduced very well in simulation, as it can be noticed from the cupping artifact that is evident in the reconstructed water phantom image at 80 kV, reported in Figure 5.3. It has been simply displayed with a different window from that one used in Figure 5.2.

The effective linear coefficients of water obtained from simulations ($\mu_{\text{eff,water,simul}}$), are reported in Table 5.1 togheter with the corresponding effective energies $E_{\text{eff,simul}}$. Effective energy values were provided by *XMuDat*. For comparison, $\mu_{\text{eff,water,real}}$ that were obtained after HU calibration (reported in Chapter 4), are also tabulated. It can be noticed that $\mu_{\text{eff,water,simul}}$ are greater than $\mu_{\text{eff,water,real}}$ values for all tube voltages with a mean percentage variation of 14 %. This difference is due to the approximation that we have done in simulation neglecting Rayleigh and Compton scattering. Thus all the scattered photons are removed from the primary beam. Anyway this approximation does not compromise the purpose for which simulation were done.

5.1.2 Contrast agents employed

Iodinated CA and metal NPs were employed in both simulated and real phantom studies since the first one represents the reference. More specifically, Iomeron 400, producted by Bracco (Milan, Italy) was used as iodinated CA. It is a water soluble compound containing iomeprol with a iodine concentration of 400 mg/mL. Metal NPs were instead synthesized at Center for Nanotechnology Innovation@Nest, Istituto Italiano di Tecnologia. We report the structure of Gold Nanoparticles

Tube voltage (kV)	$\mu_{\text{eff,water,real}}$ (mm^{-1})	$E_{\text{eff,real}}$ (keV)	$\mu_{\text{eff,water,simul}}$ (mm^{-1})	$E_{\text{eff,simul}}$ keV	Difference (%)
35	0.0406	28.5	0.0459	26.9	11
50	0.0285	37.7	0.0342	32.0	16
65	0.0245	44.7	0.0294	36.5	16
80	0.0225	50.8	0.0259	41.7	13

Table 5.1: Real effective linear attenuation coefficients of water ($\mu_{\text{eff,water,real}}$) that were obtained from HU calibration and the simulated ones ($\mu_{\text{eff,water,simul}}$) for all tube voltages of the IRIS scanner. Their relatives effective energies E_{eff} values have also been reported, as reference, together with the variation percentage between real and simulated $\mu_{\text{eff,water}}$.

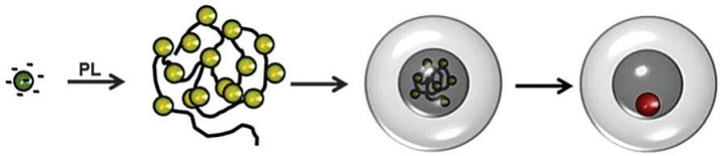

Figure 5.4: Scheme for the general formation of the nanosystem. Negative GNPs are assembled in spherical arrays employing poly(L-lysine) or dye-modified poly(L-lysine). These cores are then embedded in hollow silica shells. After calcination the organic compounds are burned and the silica shell remained intact, while gold nanoparticles are melted in a single bigger gold nanoparticle presenting a "naked" surface [29]. Image is adapted from [29].

(GNPs), as reference. It is composed of three elements:

- small GNPs with a diameter of 3 nm;
- commercial polymers surrounding the nanoparticles;
- a degradable silica shell embedding the polymer-nanoparticle assembly.

The general synthetic approach employed for the preparation of these hollow silica nanospheres containing the gold nanoparticle array is shown in Figure 5.4. In short, it consists in aggregating GNPs of (2.8 ± 0.4) nm coated by negative poly(sodium 4-styrene sulfonate), in spherical arrays by the positive poly(D- or L-lysine) by means of ionic interactions, and then growing the silica shell on this template by a modified Stöber method [29]. Interestingly, the degradation products of these nanomaterials are the polymers, small GNPs and silicic acid, compatible with the possibility of overcoming accumulation owing to the renal clearance of these building blocks. The degradation kinetics of these nanostructures in physiological media was also evaluated, and the good results obtained (compared with other similar studies) suggest that these nanosystems can represent a promising tool to overcome the issue of accumulation of inorganic NPs in organisms. For these reasons, different kind of experiments are ongoing. X-ray experiments have

Figure 5.5: Home made phantom used in characterizing the NPs x-ray attenuation properties.

been performed with the IRIS micro-CT and results are reported in the following sections.

5.1.3 Description of the phantom used for data acquisition

For metal NPs x-ray experiments, a specific phantom was realized. It consists in a plexiglas cylinder in which five small cylinders were dug all at the same distance from the phantom center. These small wells are 4 mm large and equally high, resulting in a volume of $(50 \pm 1)\,\mu L$. A specific plexiglas cover, which is screwed into the cylinder, was realized in order to avoiding CA leakage from the wells. For greater clarity, Figure 5.5 illustrates the home-made phantom here described. As it can be noticed, the cover presents overturned funnel shaped holes in correspondence of the wells through which they can be directly filled with the contrast medium with a syringe. This structure was designed to limit the formation of air bubbles, but since NPs solutions were handled with pipette and not with siringe, wells were filled directly without recurring to this device. In addition parafilm was applied in order to limit air bubbles formation.

5.2 Results

The same iodine concentrations that were realized to evaluate the imaging performances of the dynamic scanning protocol (Chapter 4), were simulated in order to compare the sensitivity of the system to iodine concentration with that obtained from simulation. Sensitivity was measured by means of the slopes of the linear fits in which CT numbers were reported as a function of iodine concentration. Results

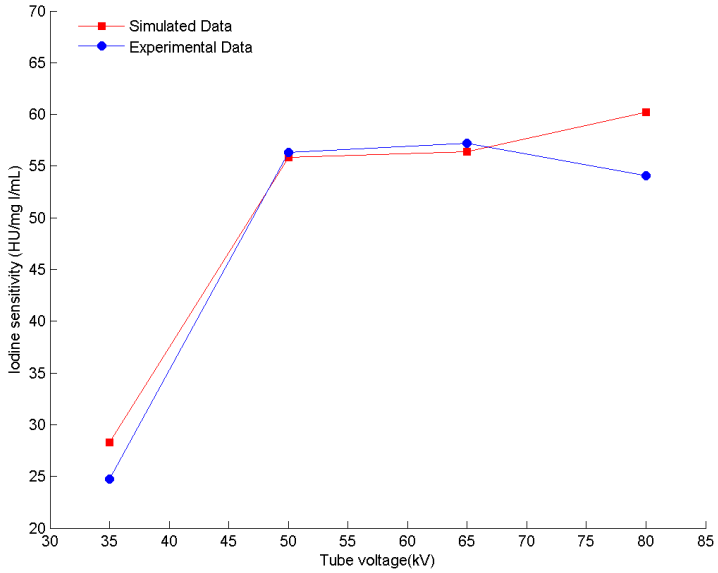

Figure 5.6: Iodine sensitivity in HU/mg I/mL for all tube voltages resulting from experimental data, in blue, and simulated data, in red.

are graphically reported in Figure 5.6 for all voltages. As it can be noticed, simulations at 50 and 65 kV give results, in terms of iodine sensitivity, comparable with experimental data, resulting in a percentage error of 0.8 % and 1 %, respectively. However, simulations at 35 and 80 kV differ more from the experimental ones with a percentage error of the iodine sensitivity of 15 % and 11 %, respectively. According to these results, different phantom simulations were perfomed before experiments with gold and platinum NPs. Simulations were also done with metal CAs, such as cerium, that were not physically available at the time of writing of this thesis. The sensitivity of the IRIS CT scanner to gold, platinum and cerium was therefore analyzed from simulation data and results are reported in Figure 5.7. Sensitivity of the system to gold and platinum decreases with increasing tube voltages, as the K-edge of the two metals is at 80.7 and 78.4 keV, respectively, i.e. above the photon energies available with the IRIS CT. The opposite trend can be noticed for cerium and iodine which present a K-edge at 40.4 and 33 keV, respectively.

Thanks to the versatility of the nanosystem, NPs incorporating different metals were synthesized at the Center for Nanotechnology Innovation@Nest. Besides GNPs, they provided to us platinum, gold-platinum and gold-cerium NPs. The metal percentage they estimated, amounted to 5.8 % for GNPs, 2.7 % for platinum NPs, and 1 % and 0.6 % for gold-platinum NPs, respectively. The metal

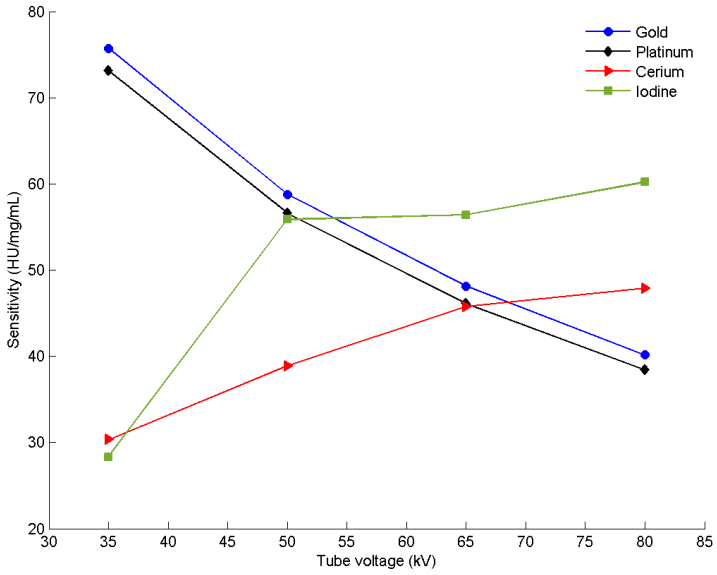

Figure 5.7: Gold, Platinum, Cerium and Iodine sensitivity in HU/mg/mL for all tube voltages resulting from simulation data are reported in blue, black, red, and green respectively.

percentage in gold-cerium NPs was not known. The main challenge was the poor available volume of NPs (of the order of μL) to be diluted as little as possible to obtain CNR values at least above the Rose threshold (CNR >5).

In order to simulate metal NPs we thought that Silicon Dioxide (SiO_2) could represent a good material to model the silica shell of these NPs. Several simulations with GNPs were perfomed for different gold concentrations. Finally it was emerged a discrete CT enhancement with CT number values that do not exceed 160 HU for the maximum GNPs concentration that was physically available, at the tube voltage of 35 kV.

With this background, GNPs x-ray experiment was done, starting from a volume of 100 μL in which GNPs were diluted in Milli-Q with a concentration of 20 mg GNPs/mL. The five wells of the home made phantom, were filled with the following concentrations: 0.51, 1.28, 3.2, 8 and 20 mg GNPs/mL. The P160-AllkV-FS protocol, described in section 4.1.4, was used to acquire tomographic images since it allows multi-energy acquisition while observing the stability time of solutions which amount to ten minutes. A cross section of the home-made phantom passing from its cavities at various concentration of GNPs is shown in Figure 5.8. The linearity between GNPs concentration and reconstructed CT numbers at the various tube voltages was to be verified; thus a circular ROI was placed in each well in order to compute the mean and the standard deviation of CT num-

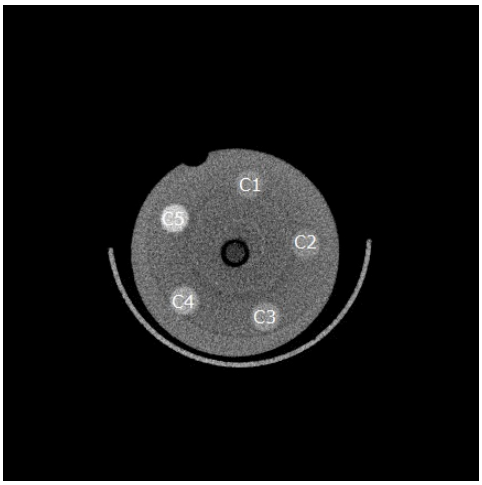

C1:MilliQ+GNPs, 0.51 mg GNPs/mL
C2:MilliQ+GNPs, 1.28 mg GNPs/mL
C3:MilliQ+GNPs, 3.20 mg GNPs/mL
C4:MilliQ+GNPs, 8.00 mg GNPs/mL
C5:MilliQ+GNPs, 20.0 mg GNPs/mL

Figure 5.8: Transaxial slice at 35 kV of the home made phantom realized to verify linearity between GNPs concentration and reconstructed CT numbers. The display window (min; max) is (−300 HU; 300 HU).

bers for each GNPs mixture. A linear fit of the obtained ROI values was performed to determine the slope and the linear correlation coefficient (R^2) for all the tube voltages. Results are illustrated in Figure 5.9 as a function of both GNPs and metal concentration taking into account that the estimated weight fraction of gold amounted to 5.8 %. In order to know CT numbers for all tube voltages corresponding to the pure Milli-Q, which represents the zero GNPs concentration, a multi-energy acquisition of the home made phantom filled with Milli-Q was perfomed with the same scanning protocol used before. The five ROIs values were then averaged in order to obtain a mean CT number to subtract to CT number of each GNPs concentration. It can be noticed from Figure 5.9 that reconstructed CT numbers showed a strong linear correlation with respect to the GNPs concentration for all voltages and it is also confirmed by the Pearson's correlation coefficient that was $R^2 \geq 0.9992$ for all voltages. The slopes of the linear fits of Figure 5.9 were then used to measure the sensitivity of the system to NPs concentration. It is reported in Figure 5.10, for all tube voltages, together with that obtained from simulations, for comparison. Simulation results differ from the experimental ones with a percentage error of 12 % at the tube voltage of 35 kV, and around 20 % at the other tube settings. The GNPs sensitivity decrease with increasing tube voltage, emerges also from the two transaxial slices of the phantom acquired at 35 and 80 kV presented in Figure 5.11, and from CNR values that were calculated respect to the plexiglas background. They are graphically reported in Figure 5.12.

As it can be noticed, the Rose threshold is reached for all GNPs concentrations only at the tube voltage of 35 kV. At 50 kV only the two higher concentrations are above the threshold, while at 65 kV only the master solution exceed the CNR

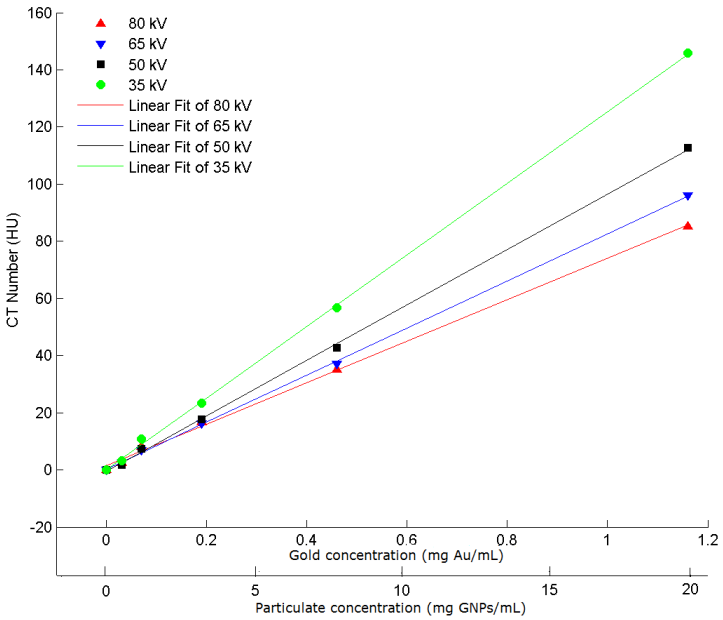

Figure 5.9: Plot of CT numbers in HU measured for all available GNPs concentrations and for all tube voltages. The fits of data have also been reported.

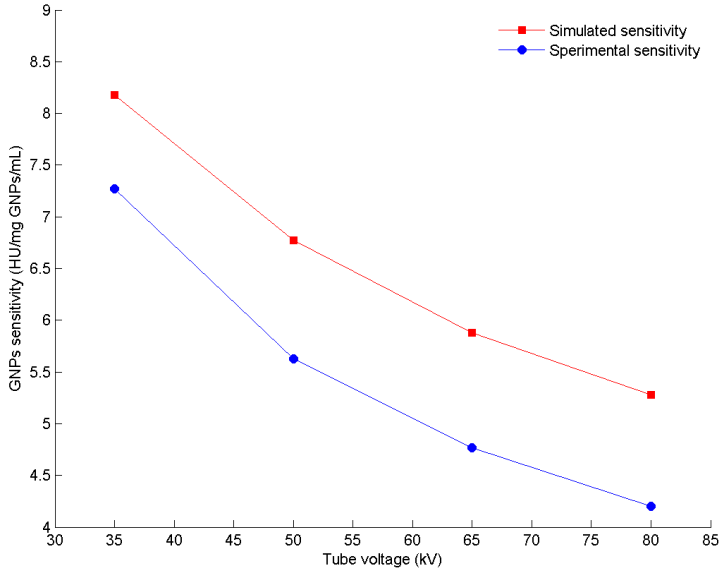

Figure 5.10: GNPs sensitivity in HU/mg GNPs/mL for all tube voltages resulting from experimental data, reported in blue, and simulated data, in red.

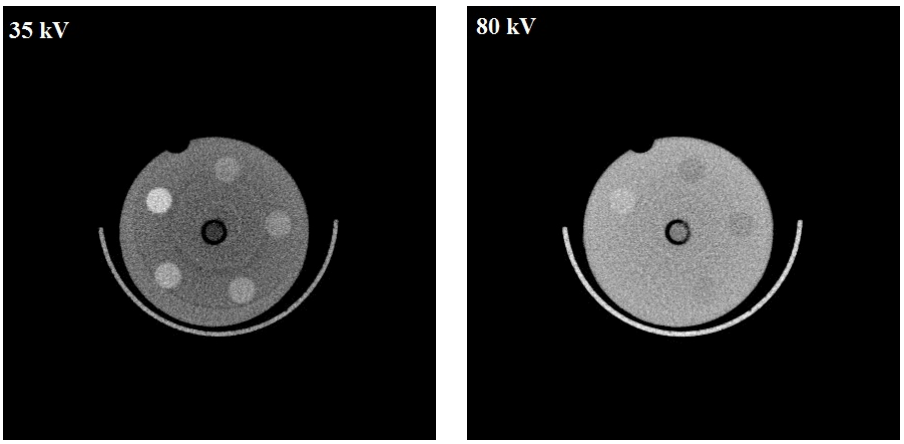

Figure 5.11: Comparison of two transaxial slices of the home made phantom which wells were filled with the various GNPs concentrations (see Figure 5.8). They were acquired at 35 kV (left) and 80 kV (right). For both images the display window (min; max) is (−300 HU; 300 HU).

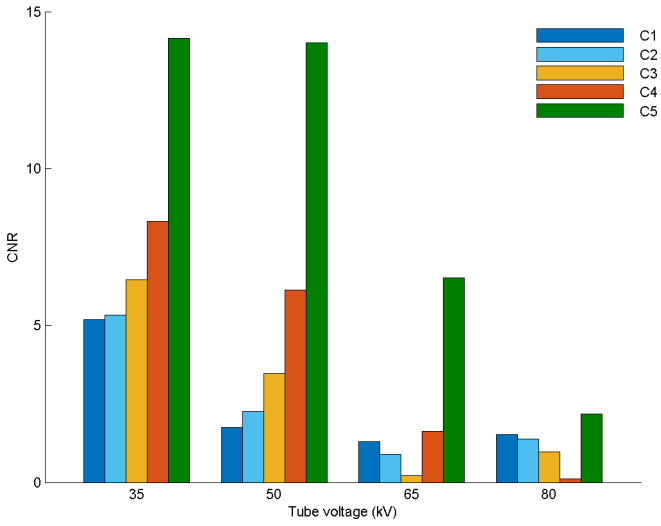

Figure 5.12: Contrast to noise ratio for all Gold Nanoparticles (GNPs) concentrations at each tube voltage.

value of five. All the CNR values at 80 kV are considerably below the threshold. Nevertheless it should be also noted that these concentrations are much lower than that generally achieved in recent in vivo studies [31, 55, 56]. A typical volume for intravenous injection into a mouse (for example into the tail vein), is in fact 0.2 mL. Since the LD50 is >5 g Au/kg, a 20 g mouse may be injected with 100 mg of gold or more [30], resulting in a gold concentration of the order of hundreds mg/mL.
Despite the low gold concentrations available, the higher attenuation of gold than iodine is confirmed by the difference of CT enhancement. In fact it is enough to observe that if for a concentration of 4.2 mg I/mL a CT signal of 112 HU at 35 kV has been observed, for a concentration of 20 mg GNPs/mL that corresponds to 1.16 mg Au/mL, the signal that has been obtained is equal to 146 HU, which is higher than the signal corresponding to a concentration of iodine three times greater than that of gold. This is also confirmed at the tube voltage of 80 kV, as it can be also seen from Figure 5.13 where two slices of the home made phantom at 35 and 80 kV are reported. More specifically, three of its cavities are filled with the previous C5, C4 and C3 mixtures of GNPs, while the other two with iodine CA at the concentration of 20 and 40 mg/mL that respectively correspond to I1 and I2 in the figure. The opposite sensitivity trend of the system to these different CAs, is evident since at 80 kV, cavities filled with GNPs are not distinguishable from background, while cavities with iodine show signal levels so high respect to the plexiglas background so that a streak artifact due to BH can be also noticed. The situation is reversed at 35 kV, though the high iodine concentrations do not may allow to see very well this difference. Thus gold and iodine can be easily differentiate by dual energy micro-CT which is an emerging micro-CT application that allows the separation of two different materials.

Platinum NPs x-ray experiment was finally perfomed filling two cavities of the home made phantom with mixtures of platinum NPs and milli-Q at the concentration of 11 and 7 mg NPs/mL. The weight fraction of platinum was so low respect to the silica shell, that we preferred to not further dilute the solution. The other three cavities were filled with mixtures of gold-cerium NPs and milli-Q at the concentration of 0.2, 0.1, and 0.05 mg NPs/mL.
As it can be noticed from the slice at 50 kV in Figure 5.14, where P1 and P2 indicate platinum NPs mixtures while G1, G2, and G3 correspond to the gold-cerium NPs ones, platinum NPs were deposited, so it was not possible to verify the linearity of CT numbers. Equally negative results concerning with gold-cerium NPs were observed, probably due to the very low particulate concentration despite CT image noise.

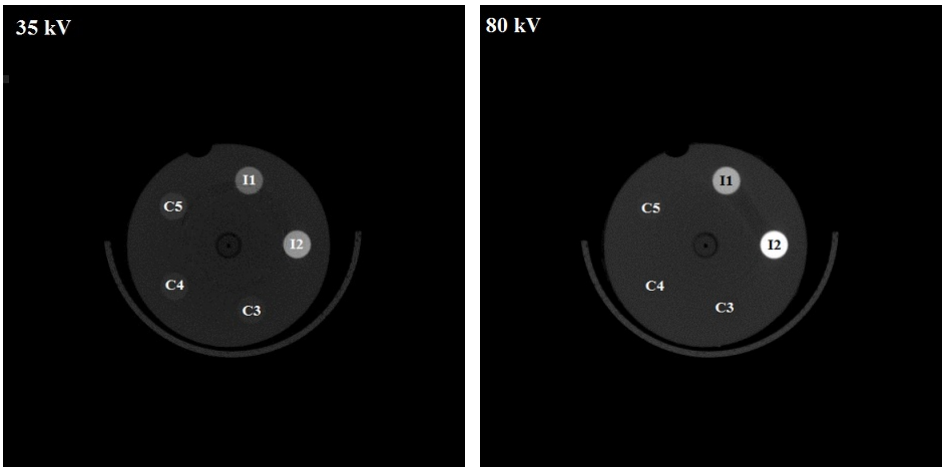

Figure 5.13: Comparison of two transaxial slices at 35 (left) and 80 (right) kV of the home made phantom which wells were filled with different mixtures of GNPs that corresponding to the previous C5, C4 and C3 and iodine CA indicated with I1 and I2, as explained in the text. For both images the display window (min; max) is (−500 HU; 2500 HU).

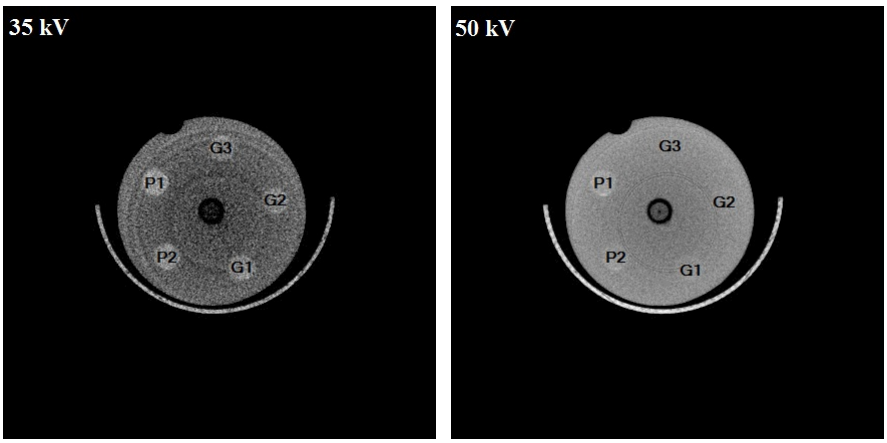

Figure 5.14: Comparison of two transaxial slices at 35 (left) and 50 (right) kV of the home made phantom which wells were filled with two mixtures of platinum NPs which are indicated with P1 and P2, and three mixtures of gold-cerium NPs which are indicated with G1, G2, and G3. For both images the display window (min; max) is (−200 HU; 200 HU).

Conclusions

In this thesis the imaging performances of the CT section of the IRIS PET/CT micro-tomograph have been evaluated. Part of this work can be meant as an extension of the physical characterization of the scanner already reported in a previous article in which the performances of the IRIS/CT were evaluated for the first time, focusing on the standard scanning protocols for all the available tube voltages and voxel sizes [23]. Spatial resolution of the tomographic system was evaluated in terms of MTF, resulting in a low contrast detectability R_{10} of 105 μm, against the theoretical value of 66.6 μm. This result suggests that at the time of writing of this thesis, a geometric calibration of the scanner might be necessary. Image noise has been further investigated in terms of coefficients of variations of the reconstructed values, and NPS, focusing on the dependence on the dose, reconstructed voxel size and reconstruction filter. Results showed that the noise has a structured appearance at all the voxel sizes under investigation. NPS of the higher resolution protocol (voxel size of 60 μm) was evaluated for all the tube voltages, observing that the scanning protocol at 35 kV produces the noisier images due to the really low fluence rate, while level noise decreases to about a sixth for other tube voltages since the mean dose increases of about the triple, as expected. Comparison between images reconstructed with different voxel size (60 and 80 μm), confirmed the inverse relationship between noise and voxel size. Finally image noise due to the reconstruction filter was taken into account. The Edge filter results the worst in terms of image noise, especially at the lower spacial frequencies, while NPS corresponding to images reconstructed with the Standard and the Smooth ones, show similar trend. Then the imaging performances of the imaging protocol designed for dynamic studies, has been analyzed in terms of CNR as a function of the density of a iodinated CA, and also as a function of object size since this protocol was proposed for perfusion studies. Known artifacts related to short-scan reconstruction in cone-beam geometry were evidenced, partly biasing the quatitative results. This limitation cannot be avoided with this kind of protocol. Moreover, due to the very limited photon flux at such a short scan duration, we have noticed that the scanning protocol at 35 kV cannot be employed for dynamic measurements. Nevertheless, for single energy scanning protocol it is anyway not recommended

to use such a low kV setting due to the very low sensitivity of the system to iodine concentration. The Rose threshold (CNR >5) at the lower iodine concentration (3.87 mg/mL) was reached only at 80 kV. Derenzo phantom was then used to study the impact of PVEs on the quantification of contrast enhancement on small structures. It was filled with a iodine solution at the concentration of 9.62 mg I/mL that approximately corresponds to that of vascular iodine concentration in typical animal studies. It emerged that, for the low resolution dynamic scan protocol (240 µm voxel size), the CNR decreased on smaller inserts, as expected due to the PVE. For the structure size available in the used phantom, PVE did not affect significantly the CNR measurements when the high-dose, high-resolution protocol (60 µm voxel size) was used. It can be said that the protocol at 80 kV seems attractive for dynamic studies since provides a good trade-off between image noise and dose (11 mGy per dynamic frame to rat). The results obtained from this study could represent the basis of further analysis aimed to optimize the CA injection protocol in real dynamic acquisitions.
The HU calibration was perfomed as required in a Quality Assurance (QA) program established at IFC for micro-CT instrumentation. The new effective linear attenuation coefficients of water, compared with the old ones that were used to calculate CT numbers, confirmed that the calibration at the time of writing of this thesis, was necessary since a mean percentage variation of 7 % was observed.
Beam Hardening of the IRIS CT scanner was analyzed and a first correction of it was provided for all tube voltages with the water precorrection method. It seems that correction is meaningful up to object size of 40 mm of diameter, as tests on the uniformity of the reconstructed image, according to the QA program at IFC for micro-CT instrumentation, also confirm.
Attention was then paid on the huge development of new CAs, in the form of metal NPs, leading to a very close cooperation between chemists and physicists. More specifically the IRIS/CT response to metal NPs was investigated. Measurements were also supported by numerical simulations that were in good agreement with experimental results. Simulations allowed to theoretically investigate the response of the IRIS CT scanner to metal types and concentrations of NPs that were not physically available at the time of writing of this thesis. Furthermore, simulations provided a first guidance to chemists for improving the formulation of NPs for the purpose of CT CAs. It emerged that gold and platinum sensitivity decreases with increasing tube voltage, as the K-edge of gold and platinum is at 80.7 and 78.4 keV, respectively i.e., above the photon energies available with the IRIS CT. An opposite trend was observed for cerium sensitivity, instead (the K-edge of this metal is in fact at 40.4 keV). CT numbers showed a strong linear correlation with respect to the GNPs concentration for all voltages. Nevertheless, it emerged from the measurements of this thesis that the NPs concentrations available for the experiments (ca. 6 % in weight) is still too low for practical in-vivo applications.

In fact in CNR measurements, the Rose threshold is reached for all GNPs concentrations only at the tube voltage of 35 kV. Even though we know from simulation that the sensitivity of the CT scanner decrease with increasing tube voltage, this result further confirms that the gold concentration is low respect with the entire nanoparticle structure. Anyway these results are sufficient to state the higher attenuation of gold than iodine at the same concentration. Phantom studies with metal NPs are still needed since, on the one hand, the efforts of chemists to increase metal concentration and prolong the stability in solution, are continuous, and the other, interesting micro-CT applications can be investigated such as dual energy which is very attractive today.

Appendix A

Script of the tool for projection data simulation

The MATLAB code for projection data simulation is divided into steps according to the physical phenomenon involved. The simulated phantom consists in a bidimensional circle with an outer radius Rext of 25 mm. Inside it there are five circular cavities of a radius R of 3 mm, each of which at approximately the same distance (sn) from the center. The corresponding center coordinates (xn, yn) are expressed in mm, as well as all the other lenghts. The chord lenghts that a ray of the beam traverses have been therefore calulated for each of the circular objects which constitute the phantom.

```
s = -57.5:0.3:57.5;         % Pixel row of the real detector
                            % for hardware binning of 4X4
D1 = 206;                   % AOR in mm
D2 = 56;                    % ADD in mm
sigma = (s*D1)./(D1+D2);    % Pixel row of the virtual detector
% Properties of the outer circumference:
Rext = 25;
xnext = 0;
ynext = 0;
sn1ext = sqrt(xnext*xnext+ynext*ynext);
Ynext = atan2(ynext,xnext);
R = 3;                              % Radius of the inner circumferences
% Properties of the first inner circumference:
xn1 = -9;
yn1 = 9;
sn1 = sqrt(xn1*xn1+yn1*yn1);
Yn1 = -atan2(yn1,xn1);
% Properties of the second inner circumference:
xn2 = -12.083;
yn2 = -4;
sn2 = sqrt(xn2*xn2+yn2*yn2);
Yn2 = -atan2(yn2,xn2);
% Properties of the third inner circumference:
xn3 = 0;
yn3 = -12.728;
sn3 = sqrt(xn3*xn3+yn3*yn3);
Yn3 = -atan2(yn3,xn3);
% Properties of the fourth inner circumference:
```

```
xn4 = 12.083;
yn4 = -4;
sn4 = sqrt(xn4*xn4+yn4*yn4);
Yn4 = -atan2(yn4,xn4);
% Properties of the fifth inner circumference:
xn5 = 9;
yn5 = 9;
sn5 = sqrt(xn5*xn5+yn5*yn5);
Yn5 = -atan2(yn5,xn5);
% Angular sampling to get 576 projection views:
beta = 0.0109:0.0109:2*pi;
% Rope lenghts calculation:
for i = 1:length(beta)
    for j = 1:length(sigma)
    t(j) = (D1.*s(j))./sqrt(D1*D1 + sigma(j).*sigma(j));
    theta (i,j) = beta(i)+atan(sigma(j)./D1);

     Lext(i,j) =  sqrt(Rext*Rext-t(j).^2);
     L1(i,j) =  sqrt(R*R-(t(j)-sn1*cos(Yn1-theta(i,j))).^2);
     L2(i,j) =  sqrt(R*R-(t(j)-sn2*cos(Yn2-theta(i,j))).^2);
     L3(i,j) =  sqrt(R*R-(t(j)-sn3*cos(Yn3-theta(i,j))).^2);
     L4(i,j) =  sqrt(R*R-(t(j)-sn4*cos(Yn4-theta(i,j))).^2);
     L5(i,j) =  sqrt(R*R-(t(j)-sn5*cos(Yn5-theta(i,j))).^2);
    end
end
```

Simulated spectra, that is photon counts as a function of the energy bin (0.5 keV), were corrected for the attenuation that beam suffers. 1.4 mm of glass and 2.5 mm of plexiglas were considered.

```
for n = 1:length(spectrum)
    N0(n) = spectrum(n).*exp(-(1.4.*glass(n))-(2.5.* pmma(n)));
end
```

The Energy Absorption Efficiency of the detector is considered in order to calculate the number of photons that will be contribute to the formation of the flat field image.

```
% Correction of the photon counts N0 according to the pixel position respect to
    the source p
p = s(:,192);
for n = 1:length(N0)            % n is the index relative to the energy bin
    for m = 1:length(sigma)     % m is the index relative to the pixel position
        Np(n,m) = (((D1+D2)^2)/((sigma(m)-p).^2+(D1+D2)^2)).* N0(n);
    end
end
% E is the energy vector that depends on the kV of the x-ray spectrum
E = 3.5:0.5:35;
for n = 1:length(N0)
  for m = 1:length(sigma)
   N0p(n,m) = (1/(D1+D2)^2).*0.5.*E(n).*(muCsI_en(n)./muCsI_t(n)).*(1-exp
       (-0.150.*muCsI_t(n))).*Np(n,m);
  end
end
Nun = sum(N0p,1); % Unattenuated photons
```

Photons that traverse the phantom and reach the detector have been simulated considering all possible crossings of the circular objects of the phantom.

```
N1p =  Np.*0.5*(1/(D1+D2)^2);
 for l = 1:576                  % l is the index relative to the angular sampling
    for m = 1:length(sigma)
```

```
        for n = 1 : length(N0)

            if real (Lext(l,m)) ~= 0
            N1p(l,m,n) = Np(n,m).*0.5.*(1/(D1+D2)^2).*exp(-2.*(pmma(n).*real(Lext
                (l,m))));
            else N1(l,m,n) = Np(n,m).*0.5*(1/(D1+D2)^2);
            end

% Crossing of L1
            if real(Lext(l,m))~=0 && real(L1(l,m))~=0
            N1p(l,m,n) = Np(n,m).*0.5*(1/(D1+D2)^2).*exp(-2.*((pmma(n).*(real(
                Lext(l,m))-real(L1(l,m))))
            +(mu1(n).*real(L1(l,m)))));
            end

% Crossing of L1 and L2
            if real(Lext(l,m))~=0 && real(L1(l,m))~=0  &&  real(L2(l,m))~=0
            N1p(l,m,n) = Np(n,m).*0.5*(1/(D1+D2)^2).* exp(-2.*(((pmma(n).*(Lext(l
                ,m)-L1(l,m)-L2(l,m)))+(mu1(n).*L1(l,m))
            +(mu2(n).*L2(l,m)))));
            end
            if real(Lext(l,m))~=0 && real(L2(l,m))~=0 && real(L1(l,m))==0
            N1p(l,m,n) = Np(n,m).*0.5*(1/(D1+D2)^2).* exp(-2.*((pmma(n).*(Lext(l,
                m)-L2(l,m)))
            +(mu2(n).*L2(l,m))));
            end

% Crossing of L1, L2, and L3
            if real(Lext(l,m))~=0  &&  real(L3(l,m))~=0
            N1p(l,m,n) = Np(n,m).*0.5*(1/(D1+D2)^2).*exp(-2.*((pmma(n).*(Lext(l,m
                )-L3(l,m)))
            +(mu3(n).*L3(l,m))));
            end
            if real(Lext(l,m))~=0 && real(L3(l,m))~=0 && real(L1(l,m))~=0 && real
                (L2(l,m))==0
            N1p(l,m,n) = Np(n,m).*0.5*(1/(D1+D2)^2).*exp(-2.*((pmma(n).*(Lext(l,m
                )-L3(l,m)-L1(l,m)))+(mu3(n).*L3(l,m))
            +(mu1(n).*L1(l,m))));
            end
            if real(Lext(l,m))~=0 && real(L2(l,m))~= && real(L3(l,m))~=0 && real(
                L1(l,m))==0
            N1p(l,m,n) = Np(n,m).*0.5*(1/(D1+D2)^2).*exp(-2.*((pmma(n).*(Lext(l,m
                )-L2(l,m)-L3(l,m)))+(mu2(n).*L2(l,m))
            +(mu3(n).*L3(l,m))));
            end

% Crossing of L1, L2, L3, and L4
            if real(Lext(l,m))~=0 && real(L4(l,m))~=0
            N1p(l,m,n) = Np(n,m).*0.5*(1/(D1+D2)^2).*exp(-2.*((pmma(n).*(Lext(l,m
                )-L4(l,m)))
            +(mu4(n).*L4(l,m))));
            end
            if real(Lext(l,m))~=0 && real(L3(l,m))~=0 && real(L4(l,m))~=0
            N1p(l,m,n) = Np(n,m).*0.5*(1/(D1+D2)^2).*exp(-2.*((pmma(n).*(Lext(l,m
                )-L3(l,m)-L4(l,m)))+(mu3(n).*L3(l,m))
            +(mu4(n).*L4(l,m))));
            end
            if real(Lext(l,m))~=0 && real(L2(l,m))~=0 && real(L4(l,m))~=0
            N1p(l,m,n) = Np(n,m).*0.5*(1/(D1+D2)^2).*exp(-2.*((pmma(n).*(Lext(l,m
                )-L2(l,m)-L4(l,m)))+(mu2(n).*L2(l,m))
            +(mu4(n).*L4(l,m))));
            end
```

```
            if real(Lext(l,m))~=0 && real(L4(l,m))~=0 && real(L1(l,m))~=0  &&
                real(L3(l,m))==0
            N1p(l,m,n) = Np(n,m).*0.5*(1/(D1+D2)^2).*exp(-2.*((pmma(n).*(Lext(l,m
                )-L4(l,m)-L1(l,m)))+(mu4(n).*L4(l,m))
            +(mu1(n).*L1(l,m))));
            end

% Crossing of L1, L2, L3, L4, and L5
            if real(Lext(l,m))~=0 && real(L5(l,m))~=0
            N1p(l,m,n) = Np(n,m).*0.5*(1/(D1+D2)^2).*exp(-2.*((pmma(n).*(Lext(l,m
                )-L5(l,m)))
            +(mu5(n).*L5(l,m))));
            end
            if real(Lext(l,m))~=0 && real(L5(l,m))~=0 && real(L4(l,m))~=0
            N1p(l,m,n) = Np(n,m).*0.5*(1/(D1+D2)^2).*exp(-2.*((pmma(n).*(Lext(l,m
                )-L5(l,m)-L4(l,m)))+(mu5(n).*L5(l,m))
            +(mu4(n).*L4(l,m))));
            end
            if real(Lext(l,m))~=0 && real(L3(l,m))~=0 && real(L5(l,m))~=0
            N1p(l,m,n) = Np(n,m).*0.5*(1/(D1+D2)^2).*exp(-2.*((pmma(n).*(Lext(l,m
                )-L3(l,m)-L5(l,m)))+(mu3(n).*L3(l,m))
            +(mu5(n).*L5(l,m))));
            end
            if real(Lext(l,m))~=0 && real(L2(l,m))~=0 && real(L5(l,m))~=0
            N1p(l,m,n) = Np(n,m).*0.5*(1/(D1+D2)^2).*exp(-2.*((pmma(n).*(Lext(l,m
                )-L2(l,m)-L5(l,m)))+(mu2(n).*L2(l,m))
            +(mu5(n).*L5(l,m))));
            end
            if real(Lext (l,m))~=0 && real(L5(l,m))~=0 && real(L1(l,m))~=0
            N1p(l,m,n) = Np(n,m).*0.5*(1/(D1+D2)^2).*exp(-2.*((pmma(n).*(Lext(l,m
                )-L5(l,m)-L1(l,m)))
            +(mu5(n).*L5(l,m))+(mu1(n).*L1(l,m))));
            end
        end
    end

 end
```

N1p(l,m,n), that is unattenuated photons that reach the detector depending on the bin energy (l), the pixel location (m) and the bin energy (n), will be corrected for the Energy Absorption Efficiency of the detector as already seen before.

Bibliography

[1] ASTM E1441-97, "Standard guide for computed tomography (CT) imaging", *American Society for Testing and Materials*, 1997.

[2] A. DelGuerra, D. Panetta, 1-Radiation Measurements, in : F. Rösch, "Nuclear and Radiochemistry, Volume 2: Modern Applications", *De Gruyter*, 2016, pp. 1-12.

[3] R.F. Laitano, "Fondamenti di dosimetria delle radiazioni ionizzanti", *ENEA*, 2013, pp 45-54.

[4] A. Brahme, "Comprehensive Biomedical Physics, Volume 2: X-Ray and Ultrasound Imaging", *Elsevier*, 2014, pp. 49-88, 99-102.

[5] Beutel, Kundel, Van Metter, "Handbook of Medical Imaging, Volume 1: Physics and Psychophysics", *SPIE, Bellingham, WA*, 2000, pp. 67-68.

[6] A.C. Kak and M. Slaney, "Principles of computerized tomographic imaging", *IEEE press, New York*, 1988.

[7] J.H. Radon, "Über die Bestimmung von Funktionem durch ihre Integralwerte längs gewisser Mannigfaltigkeiten", *Berichte Sächsische Akademie der Wissenschaften*, 1917, 69: 262-267.

[8] L.A. Feldkamp, L.C. Davis, J.W. Kress, "Practical Cone-Beam Algorithm", *Journal of the Optical Society of America A*, 1984, Vol. 1, No.6.

[9] H. Tuy, "An Inversion Formula for Cone-Beam Reconstruction", *SIAM Journal of Applied Mathematics*, 1983, 43: 546-552.

[10] M.L. Bouxsein, S.K. Boyd, B.A. Christiansen, et al., "Guidelines for assessment of bone microstructure in rodents using micro-computed tomography", *American Society for Bone and Mineral Research*, 2010, 25(7): 1468-86.

[11] D.P. Clark, C.T. Badea, "Micro-CT of rodents: State of the art and future perspectives", *Physica Medica*, 2014, 1-16.

[12] J. Ehling, B. Theek, F. Gremse, et al., "Micro-CT Imaging of Tumor Angiogenesis: Quantitative Measures Describing Micromorphology and Vascularization", *The American Journal of Pathology*, 2014, 184(2): 431-44.

[13] T.L. Kline, M. Zamir, E.L. Ritman, "Accuracy of Microvascular Measurements Obtained From Micro-CT Images", *Annals of Biomedical Engineering*, 2010, 38(9): 2851-2864.

[14] C.T. Badea, K.K. Athreya, G. Espinosa, et al., "Computed tomography imaging of primary lung cancer in mice using a liposomal-iodinated contrast agent", *PLoS One*, 2012, 7(4): e34496.

[15] E.L. Ritman, "Current Status of Developments and Applications of Micro-CT", *Annual Review of Biomedical Engineering*, 2011, 13: 531-552.

[16] N.L. Ford, M.M. Thornton, D.W. Holdsworth, "Fundamental Image Quality Limits for Microcomputed Tomography in Small Animals", *Medical Physics*, 2003, 30(11): 2869-2877.

[17] C.T. Badea, L.W. Hedlund, G.A. Johnson "Micro-CT with respiratory and cardiac gating", *Medical Physics*, 2004, 31(12): 3324-3329.

[18] X. Guo, S.M. Johnston, G.A. Johnson, et al., "A comparison of sampling strategies for dual energy micro-CT", *Proceedings of SPIE*, 2012, 8313.

[19] S.A. Detombe, N.L. Ford, F. Xiang, et al., "Longitudinal follow-up of cardiac structure and functional changes in an infarct mouse model using retrospectively gated micro-computed tomography", *Investigative Radiology*, 2008, 43(7): 520-9.

[20] Z. Kan, S. Phongkitkarun, S. Kobayashi, et al., "Functional CT for quantifying tumor perfusion in antiangiogenic therapy in a rat model", *Radiology*, 2005, 237(1): 151-8.

[21] S. Phongkitkarun, S. Kobayashi, Z. Kan, et al., "Quantification of angiogenesis by functional computed tomography in a Matrigel model in rats", *Academic Radiology*, 2004, 11(5): 573-82.

[22] F. Eisa, R. Brauweiler, M. Hupfer, et al., "Dynamic contrast-enhancedmicro-CTonmice with mammary carcinoma for the assessment of antiangiogenic therapy response", *European Society of Radiology*, 2011, 22: 900-9007.

[23] D. Panetta, N. Belcari, M. Tripodi, et al., "Performance evaluation of the CT component of the IRIS PET/CT preclinical tomograph", *Nuclear Instruments & Methods in Physics Research A*, 2015, 22(4): 135-144.

[24] https://en.wikipedia.org/wiki/Polyetherimide.

[25] G. Poludniowski, G. Landry, F. DeBlois, et al., "SpekCalc: a program to calculate photon spectra from tungsten anode x-ray tubes", *Physics in Medicine and Biology*, 2009, 54(19): N433-8.

[26] V.G. Pronyaev, "XMuDat: Photon attenuation data on PC Version 1.0.1 of August 1998. Summary documentation", *International Atomic Energy Agency, Nuclear Data Section, Vienna*, 1998.

[27] J.J. Pasternak and E.E. Williamson , "Clinical Pharmacology, Uses, and Adverse Reactions of Iodinated Contrast Agents: A Primer for the Non-radiologist", *Mayo Clin Proc.*, 2012, 87(4): 390-402.

[28] J. Xie, S. Lee, X. Chen "Nanoparticle-based theranostic agents", *Advanced Drug Delivery Reviews*, 2010, 62(11): 1064-1079.

[29] D. Cassano, D.R. Martir, G. Signore, et al., "Biodegradable hollow silica nanospheres containing gold nanoparticle arrays", *The Rojal societu of Chemistry.*,2015, 51, 9939-9941.

[30] Nanoprobes, "$AuroVist^{TM}$: The first Gold Nanoparticle X-ray Contrast Agent for in vivo use", 2009, Product Information and Instructions.

[31] J. Domey, U. Teichgräber, I. Hilger, "Gold nanoparticles allow detection of early-stage edema in mice via computed tomography imaging", *Int J Nanomedicine*, 2015, 10: 3803-14.

[32] H. Boll, S. Nittka, F. Doyon, et al., "Micro-CT Based Experimental Liver Imaging Using a Nanoparticulate Contrast Agent: A Longitudinal Study in Mice", *PLoS ONE*, 2011, 6(9): e25692.

[33] K. Ai, Y. Liu, J. Liu, et al., "Large-Scale Synthesis of Bi 2 S 3 Nanodots as a Contrast Agent for In Vivo X-ray Computed Tomography Imaging", *Advanced Materials*, 2011, 23(42): 4886-4891.

[34] N. Lee, S.H. Choi, T. Hyeon, "Nano-Sized CT Contrast Agents", *Advanced Materials*, 2013, 25(19): 2641-2660.

[35] J.R. Ashton, N. Befera, D. Clark, "Anatomical and functional imaging of myocardial infarction in mice using micro-CT and eXIA 160 contrast agent", *Contrast Media Mol. Imaging* 2014, 9(2): 161-168.

[36] R. Popovtzer, A. Agrawal, N. A. Kotov, et al., "Targeted Gold Nanoparticles Enable Molecular CT Imaging of Cancer", *Nano Letters*, 2008, 8 (12): 4593-4596

[37] V.P. Torchilin, "PEG-based micelles as carriers of contrast agents for different imaging modalities", *Advanced Drug Delivery Reviews*, 2002, 54(2): 235-252.

[38] S.Y.Jang, H.K. Kim, H. Youn, et al., "Fourier Analysis of Noise Characteristics in Cone-Beam Microtomography Laboratory Scanners", *IEEE Trans Biomed Eng.*, 2016, [Epub ahead of print].

[39] D.S. Evans, A. Workman, M. Payne, "A comparison of the imaging properties of CCD-based devices used for small field digital mammography", *Physics in Medicine and Biology*, 2002, 47(1): 117-135.

[40] H. Illers, D. Vandenbroucke, E. Buhr, "Measurement of correlated noise in images of computed radiography systems and its influence on the detective quantum efficiency", *Proceedings of the SPIE*, 2004, 5368: 639-647.

[41] J.T. Dobbins III, E. Samei, N.T. Ranger, et al., "Intercomparison of methods for image quality characterization. II. Noise power spectrum", *Medical Physics*, 2006, 33(5): 1466-1475.

[42] U. Neitzel, S. Günther-Kohfahl, G. Borasi, et al., "Determination of the detective quantum efficiency of a digital X-ray detector: Comparison of three evaluations using a common image data set", *Medical Physics*, 2004, 31(8): 2205-11.

[43] Organisation Intergouvernementale de la Convention du Mètre, "The International System of Units (SI)", *Bureau International des Poids et Mesures (BIPM)*, 2006.

[44] A. Rose, "The sensitivity performance of the human eye on an absolute scale", *Journal of the Optical Society of America A*, 1948, 38(2): 196-208.

[45] N.W. Marshall, "An examination of automatic exposure control regimes for two digital radiography systems", *Physics in Medicine and Biology*, 2009, 54(15): 4645-4670.

[46] C.H. McCollough, S. Leng, L. Yu, et al., "CT Dose Index and Patient Dose: They Are Not the Same Thing", *Radiology*, 2011, 259(2): 311-316.

[47] J.M. Boone, O. Velazquez, S.R. Cherry, "Small-Animal X-ray Dose from Micro-CT", *Molecular Imaging*, 2004, 3(3): 149-158.

[48] A.C. Konstantinidis, "Evaluation of digital X-ray detector for medical imaging applications", Phd Thesis, 2011.

[49] A.L. Kwan, J.M. Boone, K. Yang, et al., "Spatial resolution characteristics of a breast CT scanner", *Medical Physics*, 2007, 34(1): 275-281.

[50] N. Belcari, M.G. Bisogni, C. Carpentieri, et al., "Preliminary characterization of a single photon counting detection system for CT application", *Nuclear Instruments and Methods in Physics Research A*, 2007, 576(1): 204-208.

[51] J.H. Cho, D. Pal, J.B. Thibault, et al., "Reducing short-scan artifacts in 3D axial cone-beam CT with extra views", *The 13th International Meeting on Fully Three-Dimensional Image Reconstruction in Radiology and Nuclear Medicine*.

[52] M. Soret, S.L. Bacharach, I. Buvat, "Partial-Volume Effect in PET Tumor Imaging", *The Journal Of Nuclear Medicine*, 2007, 48(6): 932-945.

[53] J.F. Barrett, N. Keat, “Artifacts in CT: Recognition and Avoidance”, *RadioGraphics*, 2004, 24(6): 1679-1691.

[54] E. Van de Casteele, “Model-based approach for Beam Hardening Correction and Resolution Measurements in Microtomography”, PhD Thesis, 2004.

[55] L. Nebuloni, “Monitoring angiogenesis in tissue engineering through time-lapsed vascular imaging”, PhD thesis, 2013.

[56] J.F. Hainfeld, M.J. O’Connor, F.A. Dilmanian, et al., “Micro-CT enables microlocalisation and quantification of Her2-targeted gold nanoparticles within tumour regions”, *The British Journal of Radiology*, 2011, 84(1002): 526-533.